PASSIVE DISPOSAL OF LAUNCH VEHICLE STAGES IN GEOSTATIONARY TRANSFER ORBITS LEVERAGING SMALL SATELLITE TECHNOLOGIES

A Thesis

presented to

the Faculty of California Polytechnic State University,

San Luis Obispo

In Partial Fulfillment

of the Requirements for the Degree

Master of Science in Aerospace Engineering

by

Marc Alexander Galles

June 2021

COMMITTEE MEMBERSHIP

TITLE: Passive Disposal of Launch Vehicle Stages in Geostationary Transfer Orbits Leveraging Small Satellite Technologies

AUTHOR: Marc Alexander Galles

DATE SUBMITTED: June 2021

COMMITTEE CHAIR: Kira Abercromby, Ph.D.
Professor of Aerospace Engineering

COMMITTEE MEMBER: John Bellardo, Ph.D.
Professor of Computer Science

COMMITTEE MEMBER: Pauline Faure, Ph.D.
Assistant Professor of Aerospace Engineering

COMMITTEE MEMBER: Liam Cheney,
Mission Manager, NASA

ABSTRACT

Passive Disposal of Launch Vehicle Stages in Geostationary Transfer Orbits Leveraging Small Satellite Technologies

Marc Alexander Galles

Once a satellite has completed its operational period, it must be removed responsibly in order to reduce the risk of impacting other missions. Geostationary Transfer Orbits (GTOs) offer unique challenges when considering disposal of spacecraft, as high eccentricity and orbital energy give rise to unique challenges for spacecraft designers. By leveraging small satellite research and integration techniques, a deployable drag sail module was analyzed that can shorten the expected orbit time of launch vehicle stages in GTO. A tool was developed to efficiently model spacecraft trajectories over long periods of time, which allowed for analysis of an object's expected lifetime after its operational period had concluded. Material limitations on drag sail sizing and performance were also analyzed in order to conclude whether or not a system with the required orbital performance is feasible. It was determined that the sail materials and configuration is capable of surviving the expected GTO environment, and that a 49 m^2 drag sail is capable of sufficiently shortening the amount of time that the space vehicles will remain in space.

ACKNOWLEDGMENTS

There have been many people that have supported me through my academic journey, and I would like to take this opportunity to thank them. First, to my parents Todd and Jeanine Galles, thank you for the unconditional support and love you have given me throughout my career. Your support was what enabled me to pursue my passions and grow into the individual I am today. Second, to Dr. Abercromby my advisor, thank you for your counseling not only for my thesis but throughout my time at Cal Poly. I still recall when I met with you on the first week of school to talk about changing my major to aerospace engineering, and am so happy I did. To the rest of my committee, thank you for guiding my thoughts with excellent questions. Your feedback on my research led me to find new avenues to pursue and consider. Finally, I'd like to thank the entire Cal Poly aerospace department and the Cal Poly CubeSat Laboratory. College is meant to be a place of learning not only about your degree, but about yourself. If there is one thing I've learned from Cal Poly besides *Learn by Doing*, it's to continue to question everything. Questions sprout discussions which build foundational understandings.

TABLE OF CONTENTS

LIST OF TABLES

LIST OF FIGURES

LIST OF ACRONYMS

ADAMUS	Advanced Autonomous Multiple Spacecraft Laboratory
AFRL	Air Force Research Laboratory
AO	Atomic Oxygen
ARES	Astromaterial Research and Exploration Science
Cal Poly SLO	California Polytechnic State University, San Luis Obispo
CPCL	Cal Poly CubeSat Laboratory
ΔV	Change in Velocity
EELV	Evolved Expendable Launch Vehicle
ESPA	Evolved Secondary Payload Adapter
GEO	Geostationary Earth Orbit
GNC	Guidance, Navigation and Control
GTO	Geostationary Transfer Orbit
HydroLox	Binary Fuel Mixture of Liquid Hydrogen and Liquid Oxygen
IADC	Inter-Agency Space Debris Coordination Committee
JPL	Jet Propulsion Laboratory
km	kilometers
LEO	Low Earth Orbit
m	meters
MEO	Middle Earth Orbit
μ	Gravitational Parameter of Earth, (398600 km^2 /sec^2)
NASA	National Aeronautics and Space Administration

ORDEM	Orbital Debris Engineering Model
P	Drag Force Parameter
P_n	Probability of n impacts
Pa	Pascals
PCSA	Projected Cross-sectional Area
PPOD	Poly Picosatellite Orbital Deployer
psi	Pounds per Square Inch
PSLV	Polar Satellite Launch Vehicle
ρ	Density
rad	radians
R	Radius from Earth's Center (km)
sec	Seconds
SMA	Semi-major Axis
SpaceX	Space Exploration Technologies Corporation
SRP	Solar Radiation Pressure
SSO	Sun Synchronous Orbit
STK	System Tool Kit
TA	True Anomaly
TLE	Two Line Element Set
UV	Universal Variable
VUV	Vacuum Ultraviolet radiation
WCC	Worst Case Cold
WCH	Worst Case Hot

Chapter 1

INTRODUCTION

1.1 Statement of Problem

Since the launch of Sputnik in 1957, the number of artificial satellites in orbit has grown exponentially[1, 2]. The rise in artificial satellites has been coupled with an increase in the amount of space debris, which has been reported on by NASA [2]. NASA's LEGEND evolutionary debris model created by the Orbital Debris Program Office is the united States' primary model for studying long term debris projections. It covers near-Earth space between 200 km in altitude up to 50,000 km [2]. The model populations include active and spent spacecraft, rocket bodies, fragmentation from breakups, and mission-related debris, with possible minimum diameter thresholds as small as 1 mm [2]. Shown in Figure 1.1, as of February 2021 the Orbital Debris Program Office has cataloged approximately 22,000 unique objects in orbit that are larger than 10 cm.

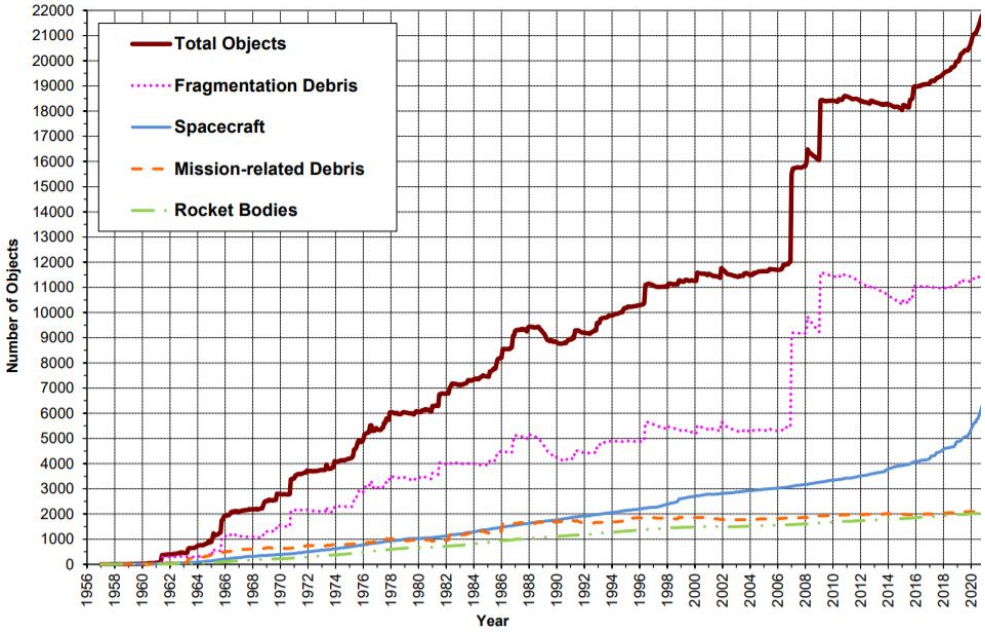

Figure 1.1: Monthly Number of Objects in Earth Orbit by Object Type [2]

As more objects are put into orbit, the probability of impact between objects increases. Defunct satellite collisions pose a threat to mankind's ability to utilize orbits around our planet. Satellites travel around the Earth with velocities that are measured in kilometers per second, meaning that impacts can often send thousands of fragments into orbit with kinetic energy to destroy other satellites. A 1 kilogram object traveling at 8 $\frac{kilometers}{second}$ has a kinetic energy of 50 Megajoules, or equivalent to about 12 kg of TNT. In 2009, a collision occurred between an inactive Russian communications satellite and an active United States communications satellite[3]. The collision produced upwards of 2000 pieces of space debris larger than 10 cm in diameter and many more pieces smaller than that. The debris created from this accident will remain in orbit for decades, potentially colliding with other spacecraft and creating more debris [3]. Space collisions of this magnitude are not common, but when they do occur it endangers many more missions than just those involved. In April of 2021, two more inactive satellites came very close to colliding; There was a 20% chance that two would collide over the Arctic [4]. Being inactive, neither party could

react or respond. Luckily, the satellites were observed after the potential collision to be intact and continuing on their paths [4].

In 1978, a NASA scientist named Donald Kessler described a potentially apocalyptic scenario in which LEO becomes unusable due to space debris[5]. Kessler Syndrome, as it has been called, is the idea that orbital collisions will create a cascade of impacts, snowballing until eventually the entire orbital plane is covered and unusable for future missions. To help reduce the growing space debris problem, the Inter-Agency Space Debris Coordination Committee (IADC) has passed guidance for all space missions passing through LEO to be maneuvered such that their expected residual orbital lifetime is 25 years or less after their operational period with at least a 90% probability of success[6]. In 2003, the IADC submitted their proposal to the United Nations Office for Outer Space Affairs, and in 2007 the General Assembly adopted the mitigation guidelines [7]. At this time the guidelines remain just that, guidelines. It will be shown later in this thesis that in fact a majority of launch vehicle providers offering GTO capabilities still do not meet these guidelines as there is no enforcement or penalty for not meeting them.

Kessler theorized this snowballing path of destruction in 1978, when spaceflight was still a fledgling industry [5]. It is unlikely that the scientist would have predicted how the industry would take off exponentially, growing from around 1000 active spacecraft in 1980 to over 6000 in 2020 [2]. With his prediction being based on available information at the time, and knowing now that the number of spacecraft in orbit has grown so fast, the likeliness of Kessler's fears being realized is even higher. As access to space has become less expensive and technology has grown so rapidly, more and more companies and institutions are expanding into space-based research which is causing the rapid growth in space presence.

Space debris is critical problem that must be addressed. How it is addressed is another challenge entirely. Many satellite operators reserve fuel for either a deorbit

maneuver or to place the satellite into a graveyard orbit[8]. The requirement to reserve fuel for an additional maneuver increases the risk to the spacecraft, as well as potentially leads to reductions in payload capacity. Some fuels such as HydroLox and other cryogenic propellants boil off or can leak out through pores in welds over time, meaning that after an extended operational period a satellite may not have enough fuel to perform any additional maneuvers[9]. For a deorbit maneuver to take place several hours after initial launch, the vehicle would need to contain enough propellant and electrical power to remain active for at least that long. One alternative to reserving propellant for active deorbiting of space vehicles is the use of sails. Gaining popularity with small satellites, drag sails and solar sails take advantage of perturbations in order to control and change the attitude and orbit of a spacecraft. This means that there is no longer a requirement to carry additional propellant, and the spacecraft can safe itself after deploying the passively controlled sail. There are additional risks with having a deployable system on the launch vehicle, and this will be discussed later in this thesis. Once deployed, aerodynamic forces can be taken advantage of to control and potentially aerostabilize the spacecraft. For this reason, this thesis will focus on drag sails as a means for deorbiting launch vehicle upper stages in Geostationary Transfer Orbits.

New spacraft platforms have arisen over the past few decades which bring with them new challenges and technological breakthroughs. These new platforms have also resulted in new branches of technology which will lay the groundwork for this thesis, such as the development of drag sail and solar sail technologies in small satellites [10, 11]. One such platform is the CubeSat, which was initially created through a partnership between Cal Poly in San Luis Obispo and Stanford University[12]. Investigation of small satellite developed technology may prove beneficial because there has been a rapid growth and adoption of small satellite platforms by various launch providers. Nanosats Database, the world's largest database of nanosatellites,

or satellites that have a mass less than 10 kg, has tracked and documented the number of CubeSats that have been launched in the last few decades [13]. The number of Nanosats and CubeSats that have been launched are shown in Figure 1.2, which shows the rapid adoption and growth that the small satellite industry has gone through as more companies and institutions begin to experiment and demonstrate new technologies on the platform [13].

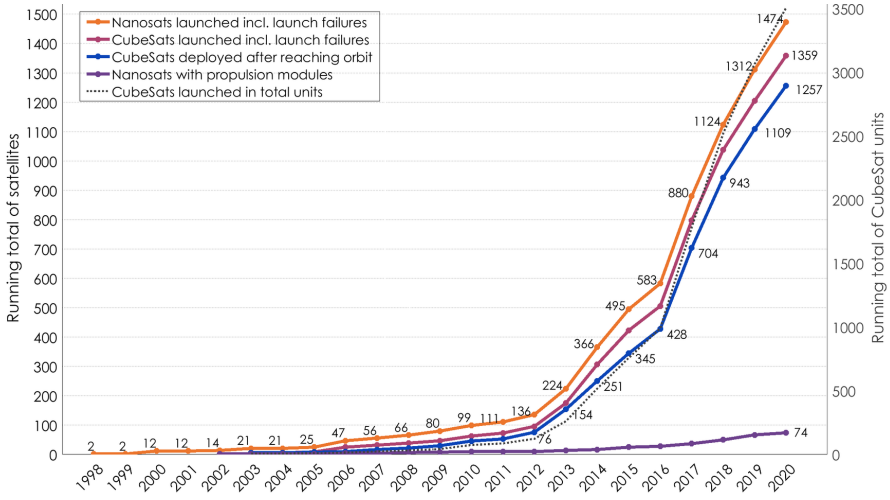

Figure 1.2: Total Nanosatellites and CubeSats Launched [13]

With the growth and adoption of small satellite launch interfaces, the platform offers a starting point for the development of a deployable drag sail for upper stage launch vehicles. A passive deorbit system is ideal because it not only reduces the risk over the missions operational period by not requiring additional chemical propellants, but it allows the vehicles to deploy the sail and then safe itself.

1.2 Objective

The objective of this thesis was to assess the current progression of small satellite drag sail technologies as well as determine what limitations might be associated with

implementation of a drag sail device on launch vehicle stages in GTOs. GTOs are a specific type of elliptical orbit which passes between LEO and GEO, typically having a perigee of around 200-500 km and an apogee of 35,800 km. Satellites which are destined for a geostationary orbit must first be put onto a GTO in order to reach their final destination. Launch vehicles that offer rideshare opportunities to small satellites usually carry several satellite dispensers to deploy them. The concept in presented in this thesis investigates whether or not it is feasible to replace one of these dispensers with a drag sail module which would aid with the orbital decay of launch vehicles in GTOs. The module would need to conform to the same form factor and interface as the small satellite dispensers, but would be used for end of mission requirements for the launch vehicle rather than deploy additional satellites.

Drag sail technologies were broken down into several categories that will be assessed in this thesis. The first category was sail performance, which researches novel designs for ensuring the drag sail is structurally capable and able to survive the space environment. The second category was orbital performance, which delved into sail performance metrics such as orbital decay and attitude dynamics. The final category was integration, which focuses on how drag sail devices are stowed and deployed, as well as how they may integrate with other systems.

A baseline layout was chosen for the drag sail system, and simulations were performed in order to verify that the chosen materials and layout would survive the structural loading expected to be experienced during its lifetime. Identification of modes of failure were also identified, with performance parameters given certain failures included in the analyses. Once the limitations of current drag sail technologies were assessed and realized, a model was developed to efficiently simulate an object's trajectory over long time frames. This model was tested on several candidate missions which have already flown and been disposed of to validate its accuracy and ability to estimate a decay date. Once the model was validated, it was used to simulate

missions utilizing launch vehicles in order to estimate how long they would remain in space before deorbiting, validating the performance impact that the inclusion of a deployable drag sail device would have on meeting the IADC's guidance.

Chapter 2

BACKGROUND

This chapter contains background information to the design and analysis of a deployable drag sail device aimed to integrate with upper stage launch vehicles in GTO. Relevant research pertaining to drag sail performance and research is covered, followed by orbital dynamics and their effects on performance. Finally, the areas of research that require further investigation are highlighted and the path forward for the development of the thesis is described.

2.1 Deployable Drag Devices

Deployable drag modulation systems utilize orbital perturbations in order to affect the spacecraft's attitude and/or orbit. Orbital perturbations often impart very small accelerations to spacecraft, which are normally handled by the Guidance, Navigation and Control (GNC) and Attitude Determination and Control (ADCS) subsystems[14]. Figure 2.1 shows the normalized acceleration that a spacecraft may experience from different perturbation as a function of altitude. At low altitudes, Drag is the dominating perturbing force, but as the altitude rises the force due to drag is exponentially diminished [14]. Other accelerations such as Solar Radiation Pressure (SRP) remain relatively constant for a wide range of orbits. With such small magnitudes, SRP and drag cannot be relied on for control methods on larger satellites, especially at higher altitudes. Acceleration due to drag is seen to decrease rapidly with altitude, and is negligible at altitudes above 800 km for orbital decay considerations.

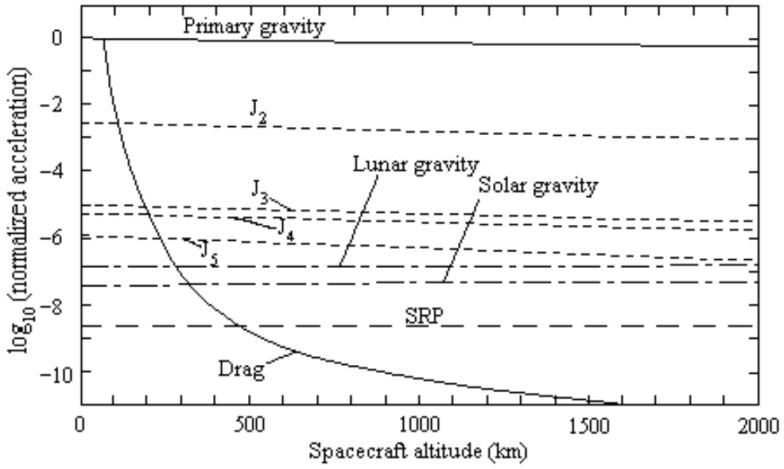

Figure 2.1: Orbital Perturbations as a Function of Altitude [14]

Manipulation of these orbital perturbations has however, been the focus of study in the development of new and innovative control laws and research on nanosatellite and small satellite platforms. On small satellites with lower inertia, where there may be constraints on using more traditional control hardware such as reaction wheels, these perturbations offer new and unique avenues for spacecraft control in LEO. In this section, important information regarding the development of such systems will be reviewed, as well as their performance from both a mechanical and orbital point of view.

2.1.1 The CubeSat Platform

With the creation of the CubeSat standard in 1999 ushering in a new, lower cost method of testing new payloads, researchers have been able to design and fly new technologies at a much higher rate. CubeSats costs are on the order of hundreds of thousands of dollars per launch, while larger satellites such as micro-satellites and general small-satellites under 500 kg cost several millions of dollars each according to NASA's Jet Propulsion Laboratory (JPL)[15]. This adds to the incentive to test new payloads on a platform like the CubeSat before implementation on larger, more expensive platforms. Larger satellites which cost millions of dollars are going to

be more risk-adverse, meaning they are less likely to incorporate low Technology-Readiness-Level (TRL) technologies. CubeSats on the other hand, offer a lower cost alternative for testing more high-risk payloads and instruments. The creation of the CubeSat platform has led to the development of new technologies, including advances in attitude control, power delivery, propulsion, and communications systems[16].

2.1.2 Notable Demonstration Missions

Several notable CubeSat missions were researched to lay the groundwork for this thesis. This section will discuss relevant information extracted from these missions as well as identify some of the challenges that were identified by the engineers that worked on them.

LightSail-1, the first of two missions created by the Planetary Society, was a solar sail demonstration mission built into a 3U CubeSat[10]. The mission used a quasi-rigid quadrant sail architecture, stowing a total sail area of 32 m^2 with a set of 4 m rigid booms provided by the Air Force Research Laboratory (AFRL). The entire sail assembly, including the deployment mechanism was configured to minimize its required storage volume, and the engineers were able to achieve an 80:1 deployed to pre-deployed ratio [10]. The LightSail missions demonstrated that larger sail areas can be stored and deployed from small volumes. The entire sail and sail deployment system fit within a 2U package. The CubeSats were able to fit a 32 m^2 solar sail, 4 booms, flight avionics, batteries, and structural components within a 3U CubeSat's form factor. The objective of this thesis is to design a drag sail to assist with deorbiting launch vehicle stages while leveraging preexisting interfaces. The sail module would be built with a CubeSat-dispenser-like mechanism that could be mounted to or replace another dispenser on a launch vehicle. Unlike the LightSail missions,the drag sail would not require flight avionics or batteries, so more volume can be allocated to packing a larger sail if necessary, and the dispenser can be more closely

designed to integrate the system. Currently, CubeSat dispensers have rails or tabs that the CubeSat interfaces with during storage and before launch, but a deployable drag sail would not need these same generalized clearances and could maximize its stowed volume.

The Canadian Advanced Nanospace eXperiment-7 (CanX-7) CubeSat is another notable mission, developed by the Space Flight Laboratory at the University of Toronto Institute for Aerospace Studies [17, 18]. The 3U satellite was launched into a 680 km Sun Synchronous Orbit (SSO) as a secondary payload on PSLV-C35. The 3.6 kg satellite used a 4 quadrant, 4 m^2 drag sail which took up a stowed volume of less than .4U (10cm x 10cm x 3 cm for each module), which was mechanically deployed by the booms [17]. Once the commands were sent, a small door to each sail was opened and the booms and sails were allowed to unwind. Similar to how the sails were deployed on the CanX-7 mission, the deployable drag sail described in this thesis could be deployed via signal received from the launch vehicle. The CanX-7 mission showed that deployment of drag sails can be achieved with stored energy from the booms, which relaxes power requirements that would be necessary for a motor-driven drag sail design. Deployment verification is also an important consideration for drag sail design, as failure to deploy part of the sail may result in unwanted angular accelerations. CanX-7 used several methods for deployment verification, including a door switch for each sail as well as sensors on the boom reels to show their extension [17].

Figure 2.2 shows the expected mission duration for the CanX-7 mission with no drag sail, with a drag sail that is not aerostabilizing, and an aerostabilized drag sail. Being a small satellite in a 680 km LEO orbit, the estimated deorbit time without drag sail deployment would have been upwards of 170 years [17]. With its sail deployed but a tumble assumed, the satellite was estimated to take approximately 4.5 years to deorbit [17]. With aerostability assumed, the same satellite was estimated to deorbit in under 3 years [17]. The analysis showed that aerostability has a posi-

tive impact on deorbit performance, and that a smaller aerostabilizing drag sail may perform as well as a larger, more massive sail that is not aerostabilizing.

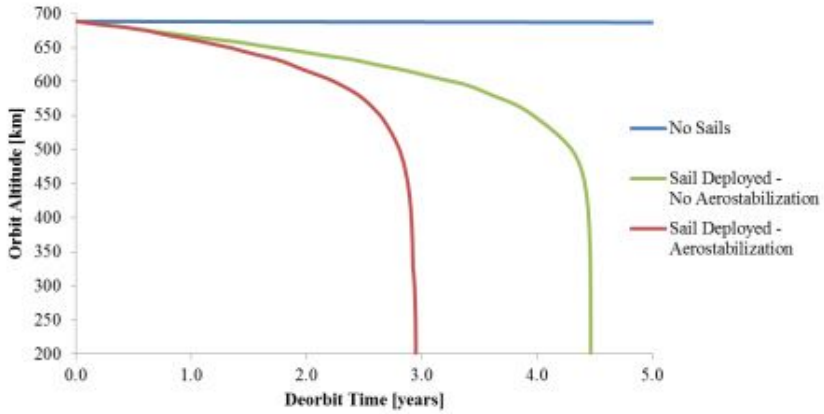

Figure 2.2: Expected Orbital Lifetime of the CanX-7 Mission [17]

The Spinnaker3 mission was developed by Purdue University and the Cal Poly CubeSat Laboratory (CPCL)[19]. Spinnaker3 is integrated with the Firefly Alpha, aiming to deorbit the rocket's second stage from a 200-mile (320 km) orbit. It accomplishes this using 3 m long booms and an 18 m^2 sail. Spinnaker3's mission is related to the concept developed in this thesis, although Spinnaker3's mission is destined for LEO operations at altitudes of around 320 km while this thesis is targeted orbits which range from 200 km to 35800 km. Spinnaker3 is designed to be integrated to the top of the FireFly Alpha's second stage, shown in Figure 2.3. The mounting location for a drag sail that is to be used on a launch vehicle is an important consideration because the location may impact the primary payload or cause additional constraints.

Figure 2.3: Spinnaker3 Deorbit Mission [19]

Interface locations present a problem for future missions as no identified secondary interface locations share the positioning of the Spinnaker3 drag sail system. The closest adaptation would be the ESPA ring, which is covered in the section Launch Vehicle Interfacing with Small Satellites. Positioning and interfaces will need to be discussed further when looking at a deployable drag device on rocket stages that won't interfere with the primary payload.

2.1.3 Orbital Performance Research

There are two major classes of solar sails, dependent on whether or not the sail is quasi-rigid with deployable booms. The first class consists of a square sail with deployable booms, while the second is the disk sail and heliogyro[20]. Disk sails and heliogyros require spin stabilization: benefiting from centrifugal forces to keep the membrane taut. With recent advances in material science leading to increased rigidity and less mass, as well as the capability of three-axis stabilization and lack of spin requirements, square sails with quasi-rigid booms have become the more popular design [20].

Along with the development of new manufacturing processes, sail boom materials and performances have also improved, able to achieve 15-25 grams/meter for booms and between 3-20 g/m^2 for sail membrane materials[20]. Understanding limitations on drag sail sizing based on mass is important for this thesis, as the aim is to leverage existing small satellite interfaces which have preexisting mass requirements.

Drag sails take advantage of atmospheric drag in order to reduce an orbit's duration. The Drag Equation, as stated by NASA, shows why drag sails are successful[22]. C_d represents the Coefficient of drag, a property of the object being analyzed which is typically determined experimentally. ρ represents the density of the medium being transversed ($\frac{kilogram}{meter^3}$), V is the velocity of the object relative to the medium it is traveling through ($\frac{meter}{second}$), and A is the area of the object with respect to the medium (meter^2) [22].

$$Drag\ Force = \frac{C_\mathrm{d} * \rho * V^2 * A}{2} \tag{2.1}$$

By manipulating the area, or creating a differential area, small satellites are able to control their orbital decay and attitude using the Drag Force[23, 24]. The University of Florida Advanced Autonomous Multiple Spacecraft Lab (ADAMUS) showed that deployable booms can be manipulated to derive controlled reentry on their 2U CubeSat [23]. The CubeSat has four deployable quasi-rigid booms which can retract or extend to provide orbital maneuvering, collision avoidance, and controlled re-entry [23]. Despite the drag perturbation's small magnitude, the satellite was still able to take advantage of it and use it for controlling its attitude.

Students at the Georgia Institute of Technology also investigated the effects of angling a drag sail on stability[24]. The students investigated the effects of changing the apex half angle of the drag sail, which is the angle between the boom and the center line of the sail. An apex angle of 90^o would mean the sail is perpendicular to the center axis, while an angle of 0^o would mean it was parallel [24]. Figure 2.4 shows a representation of the apex angle, depicted as Φ.

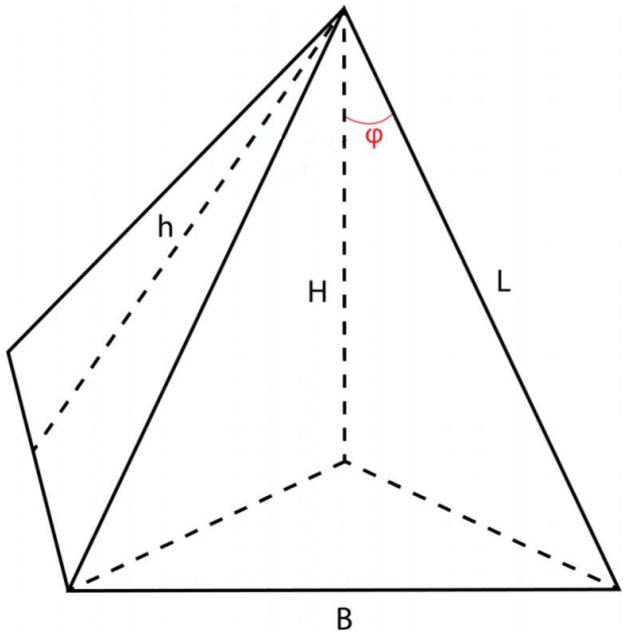

Figure 2.4: Sail Apex Angle [24]

Aerodynamic stability was evaluated over 5 orbits which ranged from 400 km to 600 km, and it was determined that the sail material and its reflectivity greatly affected stability results. The ability to change the angle of the sail and thus the spacecraft's stability will be an important consideration for long term deorbit missions. If the spacecraft is able to maintain stability, the performance benefits of aerostabilization that were shown in Figure 2.2 can be achieved, and the requirements on the drag sail size to meet the 25-year guideline can be reduced.

2.2 Design Orbit Selection and Considerations

2.2.1 Types of Orbits

The Space Foundation describes the primary orbital regions that are used around the Earth as Low Earth Orbit, Middle Earth Orbit, and Geostationary Orbit (LEO, MEO, GEO), each region of which having its own unique benefits as well as challenges[25]. Each of these orbital regimes also has unique implications on satellite disposal at the completion of its operational period. The Johnson Space Center's Orbital Debris Program Office states that at altitudes above 600 km, debris decay is measured in decades, and that debris located above 1000 km can take more than a century to deorbit [26].

For satellites to reach GEO usually requires an additional transfer orbit known as a Geostationary Transfer Orbit, shown compared to a LEO orbit in Figure 2.5. These orbits are uniquely posed because they typically have a perigee in LEO and an apogee at GEO. There are unique considerations that come from operating in GTO, including additional radiation considerations, higher velocity at perigee compared to a LEO, and a longer orbital lifetime.

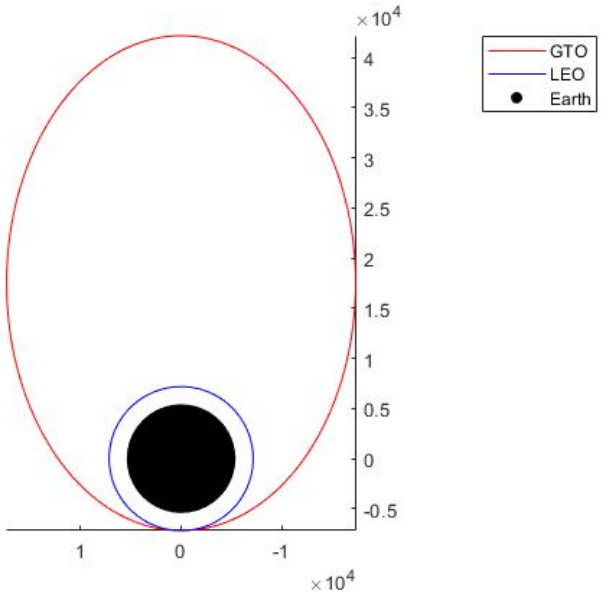

Figure 2.5: Example LEO vs GTO Orbits (units are km)

With higher energy, GTOs exhibit additional loading to structures and mechanisms of space vehicles. The typical orbit for LEO is approximately 7.8 km/second, which can be found through the application of the Vis-Viva equation for Keplerian Orbits [27]. In Eq. 2.2, μ is the gravitational parameter, R is the distance between the two bodies, and SMA is the semi-major axis of the ellipse.

$$V = \sqrt{\mu * (\frac{2}{R} - \frac{1}{SMA})} \tag{2.2}$$

The velocity at perigee for a GTO with the same perigee can also be calculated. The primary difference between the two is the SMA. With an SMA of 24,428 km, the resultant velocity at perigee for the GTO is 10.15 km/sec. This change in velocity can then be plugged into the equation for drag to understand how the loading differs between a LEO orbit and a GTO, which will be discussed further in section 3.1. This translates to higher tension in the sail's membrane and forces acting on the booms and support structure that need to be accounted for in the design process.

2.2.2 Launch Vehicle Challenges and Considerations

Launch providers face additional challenges when trying to decay or remove their rocket stages from GTO. Each launch to orbit increases the number of objects in space, including spent stages, payloads, fairings, and possibly more. Historically, spacecraft have needed all of the performance that launch providers can give and design their satellites to maximize their kilogram to price ratio [28]. With respect to GTOs in particular, it was noted that GTOs are the most difficult, requiring large ΔV's to reduce the perigee enough for reentry to occur. In addition, the added GNC and propellant requirements are difficult to meet. The rocket stage would need to have enough electrical power to continue to operate its guidance and control systems throughout its orbit, and propellant may boil off before reaching the point where a maneuver can be made. For example, in a GTO with an orbital period of 11 hours, assuming that the vehicle would inject directly into the GTO as opposed to a parking orbit, the rocket would need to have at least an additional 5 hours of electrical power and propulsion in order to make it to apogee and perform the deorbit maneuver. If using supplemental solid rockets or chemical mono-propellant thrusters for deorbiting, additional mass is lost that could be used by the payload. Launch vehicles also tend to have high ballistic coefficients, which means that they experience lower drag proportional to their mass. This is beneficial for launching payloads to orbit, but also means that the spent stages can stay in orbit for extended periods of time if reliant on passive disposal.

2.2.3 Space Environment

GTOs offer challenges with regards to the space environment. Traveling towards GEO means that the orbit will leave the safety of low earth orbit. Satellites operating in LEO are better shielded from solar activity because they are partially shielded by the Earth's Magnetosphere [29]. The Earth's magnetosphere tends to deflect this ra-

diation which ends up concentrating in what is known as the Van Allen Belts, shown in Figure 2.6. The Van Allen Belts are fields that point towards the poles, bouncing high energy particles between them. The radiation in the Van Allen Belts is, but GEO satellites must pass through these regions on their trajectory in order to reach their final orbits. The spent rocket stages that propel the GEO spacecraft to GEO are often left in an orbit that passes them through the Van Allen Belts, leading to additional radiation concerns.

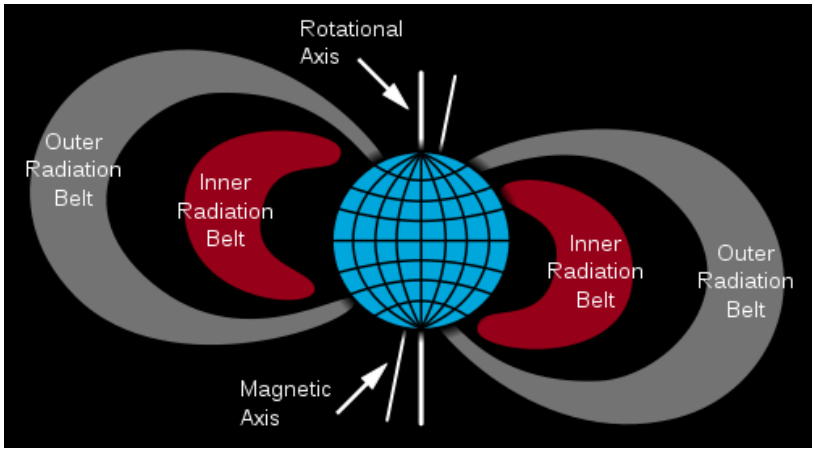

Figure 2.6: Van Allen Radiation Belts[30]

A group from NASA Marshall Space Flight Center researched the effects of electron radiation on solar sail materials at varying degrees of tension to see if there was a total dose to failure [31]. The materials, shown in Table 2.1, included Mylar of thicknesses 1.3µm, 1.6 µm, and Teonex which was 2.1 µm thick, with internal stresses ranging from 10 psi to 5000 psi. The results showed that the materials were able to survive large doses of radiation, in some cases Gigarads, without failing. For reference, a dose of 450 rads is fatal to humans. The researchers did note, however, that the samples of Mylar were exceptionally brittle after the test, which is important to understand for long-term space missions [31].

Table 2.1: Results of Sail Irradiation Test[31]

Material	Polymer thickness (μm)	Maximum tested total dose (Mrad)	Initial stress (psi)	Failure observed
Mylar	1.6	500	5000	Yes
Mylar	1.6	16740	1000	No
Mylar	1.6	16740	100	No
Mylar	1.6	16740	10	No
Al/ Mylar	1.3	4900	5000	No
Al/ Mylar	1.3	22840	5000	No
Al/Teonex	2.1	22840	5000	No
Al/Teonex	2.1	22840	5000	No

The research showed that the tension in the sail material and radiation dose to failure are directly related. Therefore, it will be important to understand the expected tension that can arise in a drag sail operating in a GTO. Another question arises from this analysis, and that is whether or not the failure of a subset of the sail area or sail membrane fails, will the mission still be successful?

Atomic oxygen (AO) is another consideration for space vehicles and can have a significant impact on mission success if not properly accounted for [32]. Testing was conducted at Cal Poly SLO to understand the material limitations of the solar sail that would be used on the LightSail-2 Mission. Simulated at an altitude of 400 km, or the orbit of the International Space Station, there was significant undercutting found after the expected fluence of 40 days in orbit was experienced [32]. This brought doubts to whether or not the sail material would be able to maintain its performance during extended duration in space. Although a GTO is typically only within the AO regime for less than 25% of its orbit, this adds up over a 25+ year mission. With a period of 11 hours per day, this means that the satellite will be within the AO region for about 5.5 hours per day. Over 25 years, this adds up to 50,187 hours or 2091 days in the AO region. This is also assuming that the orbit does not decay or change at all, which will increase the amount of time that the system is within this region. As

the orbit decays, the apogee will be reduced while the perigee will remain relatively constant. This means that over the time the spacecraft will be within the AO region for a higher proportion of its orbit. GTOs also have a higher velocity in this region, meaning that the AO impacts will be more energetic which will lead to higher erosion rates compared with the results from the testing done at Cal Poly.

The stitching in the sail, which was used to mitigate tear propagation, eroded before the sail material itself [32]. It was concluded that the stitching may last for only a few weeks in the AO environment, and that the sail itself may lost structural integrity within 15 months [32]. As shown in Figure 2.7, AO is present from altitudes around 400 km to above 1000 km, meaning that although some LEO drag sail missions may not have to consider its impact on sail materials, a GTO which passes through this region every orbit will definitely need to consider it.

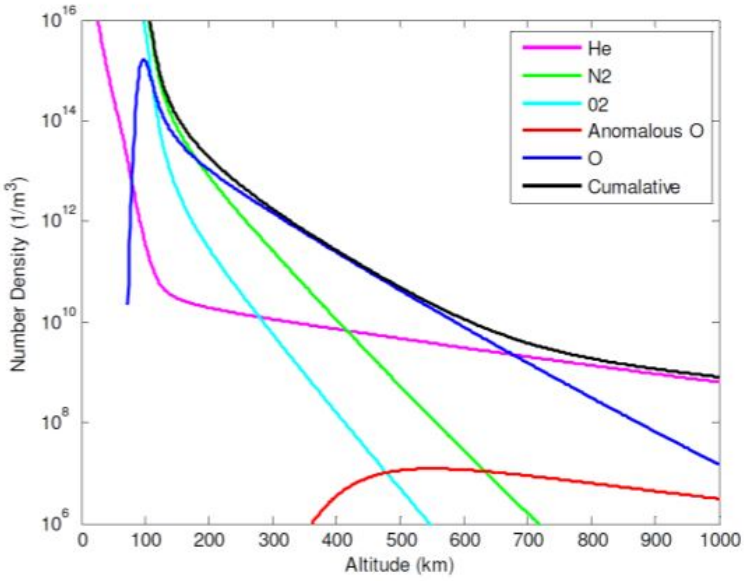

Figure 2.7: Density of Ambient Gases in Earth's Upper Atmosphere, Reported by NRLMSISE-00 Model[32]

Research was also conducted by a group of student engineers at the Space Flight Laboratory to analyze different materials for solar and drag sail applications, summarized in Table 2.2 [33]. The team looked at several materials, both aluminized and

not, to compare the depth of erosion due to AO. Aluminizing is done to stop the AO breaking polymer bonds in the films which leads to decomposition. The aluminized materials experienced reductions in erosion compared to their non-aluminized counterparts. In materials which aluminized both sides, the erosion was 0 µm [33].

Table 2.2: Atomic Oxygen Erosion Estimates[33]

Sail/Coating Combo	**Erosion Depth(µm)**
Mylar	79
Al-Mylar-Al	0
Kapton	74
Al-Kapton	29
SiO-Al-Kapton	29
Al-Kapton-Al	0
Upilex	24
Al-Upilex	9
Al-Upilex-Al	0
CP-1	50
CORIN XLS	1

The team also looked at thermal effects of the space environment, as the extreme temperatures in space can result in materials becoming brittle or experience excessive thermal expansion/contraction. The students determined the Worst Case Hot (WCH) and Worst Case Cold (WCC) for their mission and performed thermal balancing to determined how the materials would perform.

One notable assumption that was used in the analysis was to treat the sail as a thin film, thus not carrying much thermal mass. Based on their thermal analyses, which included looking at the melting temperature and glass transition of the candidate materials. Based on the assumption that half of the 25-year operational period of the sail would occur at the WCH condition, it was recommended to move forward with 12.5 µm Aluminized Upilex as the sail membrane material for their mission. Analysis on impact probability will need to be reanalyzed for a GTO mission, as the probability of impact in LEO over a few years is not equivalent to an expected 25-year mission in a GTO.

2.3 Evolution of Space Debris

The Inter-Agency Space Debris Coordination Committee was formed in October 1993 as an international forum for worldwide coordination of activities related to man-made debris and natural debris in space[36]. On November 26, 1986, an Ariane 1 second stage spontaneously exploded in LEO, creating at least 492 large pieces of debris [36]. This led to eventual creation of an inter-agency committee that was tasked with coming up with guidelines for future missions to mitigate space debris.

Historically, missions in GTO have remained in orbit for extended periods of time after completing their operational periods. TLEs pulled from Celestrak and placed in Figure 2.8 show a wide variety of missions that were initially used for GTOs, some of which were launched over 30 years ago are still in highly eccentric orbits as of June 2021[37]. This is why debris mitigation and removal in GTO is so important. Without measures in place, more debris will enter this region than will be removed.

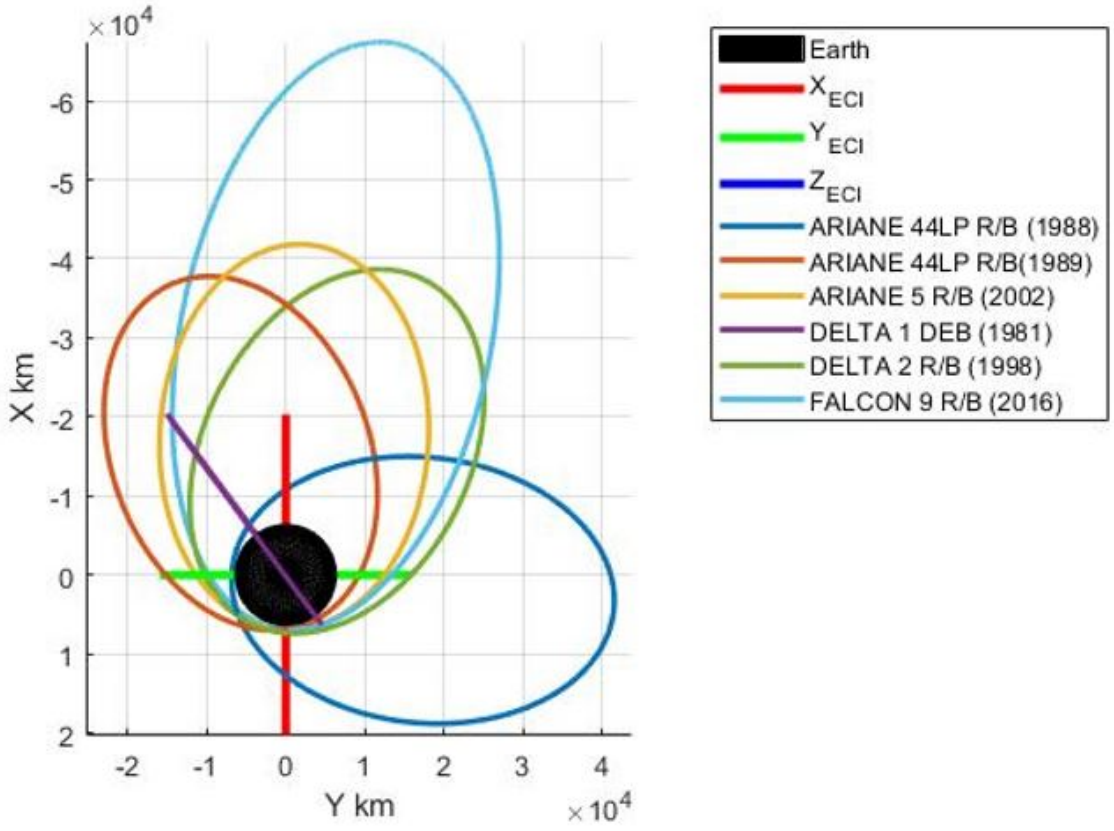

Figure 2.8: GTO Objects in Orbit [37]

Some of these missions are more than 30 years old, but others have been launched after the IADC guideline was recognized by the UN. As the number of space objects increases, it is clear that something must be done to reduce the amount of time that an object will remain in orbit. If every mission remains in orbit for decades after its operational period has finished, the probability of a collision or impact will grow, and Kessler's theoretical collisional cascade may become a reality. GTO objects are not respecting the guidelines set forth by the IADC and UN Committee on Peaceful Uses of Outer Space, not only creating more debris but potentially creating future unusable regions and orbits. The failure of these spacecraft to meet these guidelines is the basis for this thesis, to develop a drag sail system to aid with the removal of these space vehicles before they become more debris.

If nothing is changed, the projected path for passively deorbited spacecraft will continue to grow exponentially, leading to increased risk of conjunctions for astronauts and other vital space infrastructure. Studies have been done analyzing the path that humankind is tracking, and how our choices today may influence our reality tomorrow [38, 39]. This thesis offers an idea that can help mitigate these risks to our future in space. Figure 2.9 shows a projection of the number of collisions in space that will occur if no changes are made. If Post Mission Disposal (PMD) is continued, where satellites are safed after completing their operational period or placed into graveyard orbits, the number of collisions over the next century will grow exponentially. By actively removing 2 satellites after their mission has completed, the trend line of the number of collision can be curved, and by actively removing 5 satellites per year after their operational period has concluded the trend can even slow in progression.

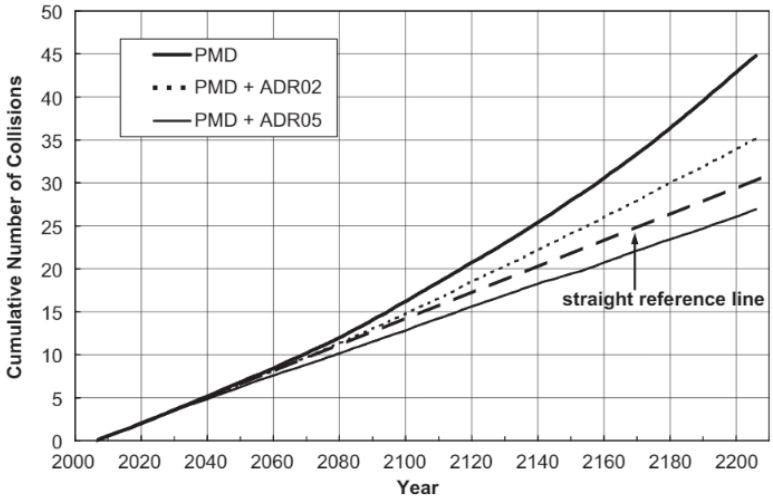

Figure 2.9: LEO Collisions Projection [38]

Figure 2.10 shows that if no measures are taken, the expected number of objects in LEO is going to grow exponentially. This analysis can be extrapolated to GTO, where current measures mean rocket stages and debris are left in high energy orbits to decay over hundreds of years. By removing 5 objects per year from LEO, the number of objects in space can be curbed, reducing the number of potential conjunctions and

unwanted accidents in space. The next few decades are pivotal, and may mean the difference between Kessler Syndrome becoming a reality and staying a theory. The prediction model was started in the 1950s, and can be compared with NASA's Orbital Debris Program Office's tracked space debris to assess its validity. In the year 2020, The simulated LEO debris population showed in Figure 2.10 shows approximately 10,000 objects greater than 10 cm, while Figure 1.1 shows that NASA was tracking over 21,000 objects [2, 38]. This shows that the models are conservative, and that in reality the total number of objects in LEO is growing faster than predicted.

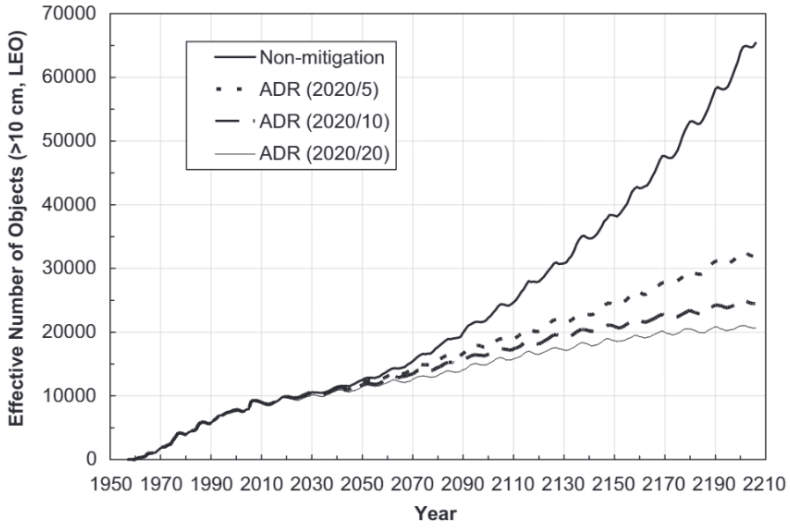

Figure 2.10: Simulated LEO Debris Population [39]

2.4 Launch Vehicle Interfacing with Small Satellites

In 1999, The CubeSat was created by Cal Poly SLO and Stanford University[40]. A CubeSat is a type of small satellite which is named for its cube-like form factor. The sizes of CubeSats are scaled in U's, which denote 10 cm x 10 cm x 10 cm volumes, and are typically $\leq$ 1kg per U.

The standard has been widely adopted, as the lower cost as well as programs that allow more access to space have created new industries and opportunities for both educational and commercial avenues. As of April 2021, more than 1680 Nano-satellites have been launched, which range from 1 kg to 10 kg, including over 1550 CubeSats [41].

As small satellites become more common, more launch vehicle providers are including interfacing locations and opportunities for launches. These deployment locations are usually located such that the secondary payloads have minimal impact on primary mission success. For the concept of a deployable drag sail device, these locations will need to be considered, as the deployment mechanism might interfere with other subsystems or not be able to fully deploy depending on the deployment orientation.

Launch vehicle spin rates also affect deployment characteristics and must be considered when designing any deployable mechanism. Not every mission requires spin stabilization, but the ULA Delta IV heavy as well as the SpaceX Falcon 9 and Ariane 5 are all capable of a spin stabilized satellite deployment of 30 degrees/sec in the roll axis[42, 43, 44, 45].

There are several locations for small satellite dispensers, making selection of an interface important. On the ULA Centaur Second Stage, CubeSats may be dispensed from the Aft Bulkhead Carrier (ABC), shown in Figure 2.11 [46].

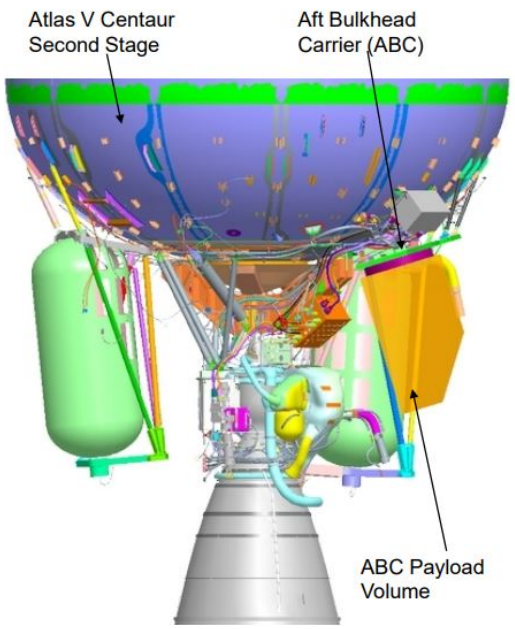

Figure 2.11: Aft Bulkhead Carrier [46]

Another secondary payload location that is more universal is the Expendable Secondary Payload Adapter (ESPA) ring, shown in Figure 2.12. The ESPA ring can carry up to 6 secondary payloads to orbit and is mated between the primary spacecraft at the second stage[47]. The ESPA ring is one of the more versatile interfaces, as several secondary payloads may be mated to it and it has the potential to be used by several launch vehicles. With the goal of being able to be integrated and used by several different launch vehicle providers, the interface location selected for this thesis must be adaptable or usable for multiple launch vehicles.

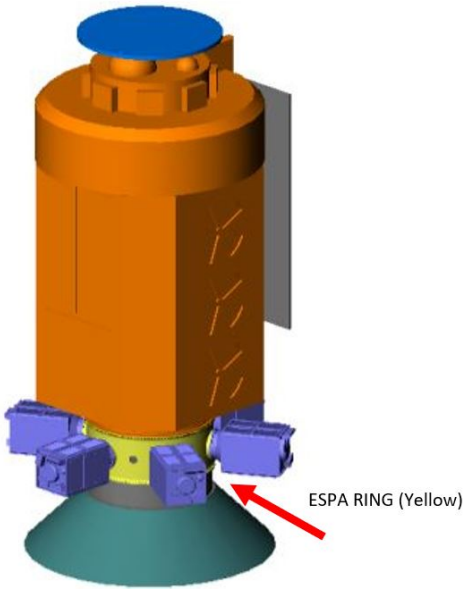

Figure 2.12: Fully Integrated ESPA Mission [47]

2.5 Summary Of Background Information

In order to begin analysis on the development of a drag sail module that can be used on GTO rocket stages, first research had to be conducted to understand the current state of the art and how the lessons learned from testing and analysis could be applied to this thesis. First, deployable drag devices were considered, and notable flight missions were researched to understand some of the design decisions that were made impacts the final results. Second, research on the orbital performance of deployable drag devices was considered in order to understand the scalability of drag sail technologies as well as identify any limitations that may be present for a potential GTO application. Rationale for the thesis was discussed, as the evolution of space debris is growing and new solutions are needed to help stunt the growth of debris in orbit. Lastly, current interface options for small satellites were considered, as the location and orientation of the drag sail module will be important for calculating orbital parameters and performance values.

Chapter 3

PERFORMANCE ANALYSIS AND DEVELOPMENT

To begin creating a baseline design for a deployable drag sail, limitations as well as performance metrics must be understood. As referenced in Types of Orbits, there are unique considerations that must be accounted for in a design focused on GTO. In this chapter, analyses will be developed and evaluated to determine an upper bound on sail design due to material limitations. Sail sizing and scalability will then be presented in the development of a new model for estimating orbital lifetime of satellites and launch vehicles. A combination of these two analyses will determine a realistic estimation of the reduction in orbital lifetime of rocket stages in GTOs.

3.1 Assessment of Sail Materials Limitations on Sail Sizing and Performance

GTOs have been identified previously to have unique considerations when designing systems to operate there. First, the higher velocity associated with GTOs means that structural components must be designed to withstand higher peak loading. Second, there are additional environmental concerns for space vehicles in GTOs compared to LEO orbits. These metrics drive the following analysis to determine if there is an upper bound for drag sail sizing for a 25-year GTO mission. If a sail is designed such that the launch vehicle using it would meet the IADC's guideline but the sail fails due to structural loading or material failure, there is no benefit to including it. The maximum loading for a drag sail placed in a Low Earth Orbit and a Geostationary Transfer Orbit with the same perigee are shown in Figure 3.1. The x axis represents the width of the square sail, meaning the total sail area can be calculated

by squaring the value. The drag experienced by the same sail is about 1.75 times higher for the GTO. The steep rise in loading is due to the increased velocity, which is squared in the equation for calculating the drag experienced by a spacecraft in eq. 2.1.

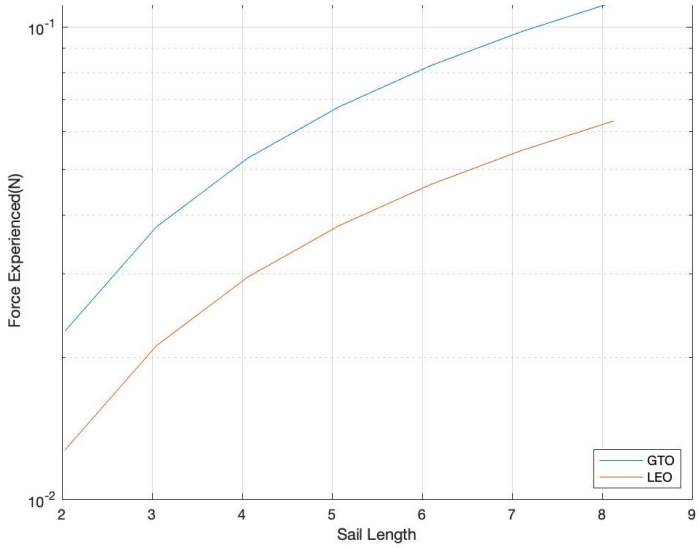

Figure 3.1: Example Loading in a Sail in GTO vs LEO

There are several concepts for drag sails that were considered for this thesis. The most popular sail design based on literature researched is the quadrant sail with deployable semi-rigid booms, which has seen applications for both solar sails and drag sails in various CubeSat missions[10, 17, 19, 20]. It has also been shown that square solar sails can be designed to induce some level of aerostability in LEO, which is talked more about in the Efficiently Modeling Long Term Orbital Progression of Launch Vehicle Stages and Satellites section 3.2. One issue that is presented with quadrant sail designs is the need for considerations regarding sail tearing, since tear propagation is a function of the number and size of impacts on the sail as well as the tensile loading on the membrane. The typical strategy to reduce tear propagation is to include stitching that would disrupt tear propagation and reinforce the sail; However, stitching has been found to be susceptible to atomic oxygen[32]. Many researchers have investigated other ways to both reduce potential loading on the sail

membrane as well as mitigate the effects of undercutting and tearing in the harsh space environment. The Surrey Space Centre published a paper describing the idea of a stripped solar sail as it compares to quadrant sails[46]. The general layout of both types of sails are shown in Figure 3.2. Rather than just dividing the sail area into four unique quadrants, the design breaks each quadrant into individual strips of sail material which are attached to the booms. The strips widths can be chosen based on manufacture supplied strip widths or cut to be thinner, easing in house assembly and integration.

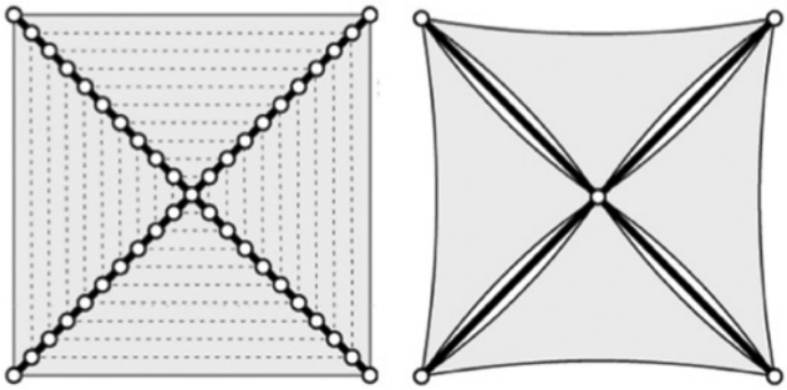

Figure 3.2: Quadrant and Stripped Sail Designs[46]

The stripped sail design has several benefits, which led it to being selected as the sail layout for further analysis. Current sail attachment methods impact sail scalability, since attaching the sail to the tip of the boom creates the largest moment arm. LightSail-2, which had a 32 m^2 solar sail, is shown in Figure 3.3 just prior to completing deployment of its sail. Unlike the stripped sail design, the sails are attached to the tips of the booms rather than along the length of the boom, which is visible in the figure. This means that there is a larger moment created at the boom tip which can lead to additional deformation of the sail as well as increased risk of material fatigue resulting in potential structural failures.

After just one year in space, one of the booms on the LightSail-2 buckled[47]. Information on why the boom buckled was not found online, but the team had reported that the failure did not greatly impact the mission [47].

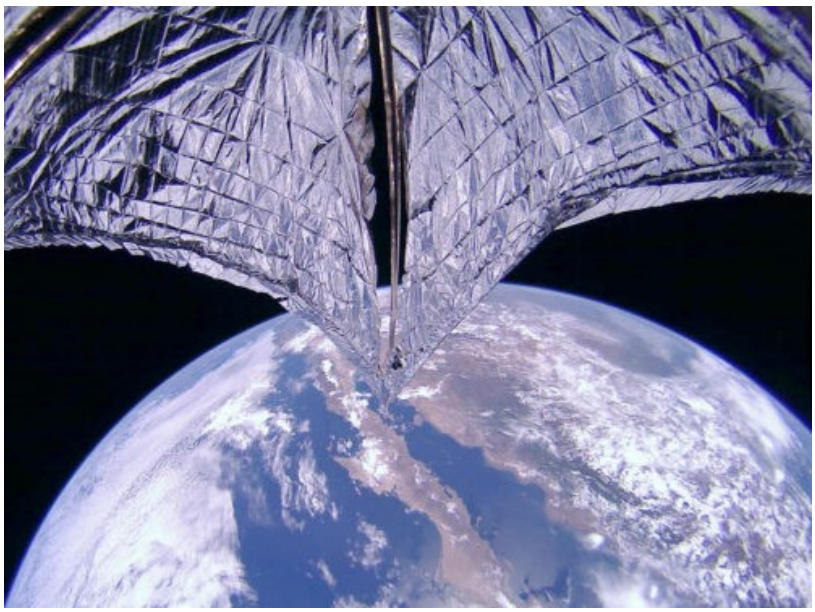

Figure 3.3: LightSail-2 Sail Attachment Scheme[47]

Using individual strips reduces the effective length for global buckling, meaning that the overall design can be lighter and less boom rigidity is required for the same size sail. Research has been conducted on a stripped sail design with the goal of developing a 10,000 m^2 solar sail[48]. Although such a large sail required a much more complex deployment and boom structural design to account for the extremely large sail area, it shows the merit of the stripped sail design and its ability to be scaled more easily than traditional quadrant sails or heliogyros. In 2004, as part of their Phase II contract, the engineers from L'Garde, Ball Aerospace, and NASA Langley Research Center successfully deployed a 10 m long stripped sail quadrant, shown in Figure 3.4 [48]. This quadrant would equate to a total sail area of 100 m^2 sail area.

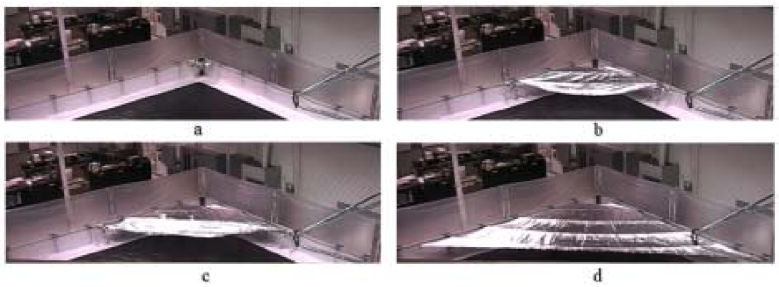

Figure 3.4: Test Deployment of 10 m Stripped Sail Quadrant[48]

The second benefit of the stripped sail is that the sail membrane can be treated as if it is placed in uniaxial tension[46]. The loading experienced by each strip is distributed along the membrane and into the booms, as opposed to the biaxial tension state that is present in quadrant sails. This is useful for determining material limitations for sail loading and impacts tear propagation.

The stripped sail design also performs better with regards to failure and redundancy. Since the sail consists of several parallel strips per quadrant, if there is a tear in one of the strips it will not affect the entire quadrant. The spacing between strips is physical, although small, and is not affected by the space environment the way stitching would be. Failure analysis on performance will be covered in a the Efficiently Modeling Long Term Orbital Progression of Launch Vehicle Stages and Satellites section 3.2.

It is inevitable that large area solar or drag sails that remain in space for extended period of time will be impacted by natural and artificial debris such as micrometeorites or debris from previous spacecraft. Analysis formulation on material failures was adapted for GTO and modified to account for the stripped sail design as opposed to a quadrant sail design[33]. Software from the NASA Astromaterial Research & Exploration Science (ARES) Office's Orbital Debris Model (ORDEM) 3.0 software was also used to generate particle fluence density throughout the trajectory[49]. The software can estimate particle flux over time that can be used to determine the probability of impacts occurring over a mission's lifetime. Figure 3.5 shows the estimated

flux density for a GTO with a perigee of 180 km and an apogee of 35000 km. The mission simulation was started in 2022, and can be used to estimate the total flux of particles that a certain drag sail area would encounter for a given mission duration. The orbit was chosen based on available information on target GTO orbits from user guides of launch vehicle providers[40, 41, 42, 43]. One important note is that ORDEM does not account for particles smaller than 10 cm at altitudes greater than 2000 km, which is a majority of a GTO's trajectory. This model is still a good estimate, however, because there a higher spatial density of objects below 2000 km relative to the rest of the orbital regime that will be simulated [90].

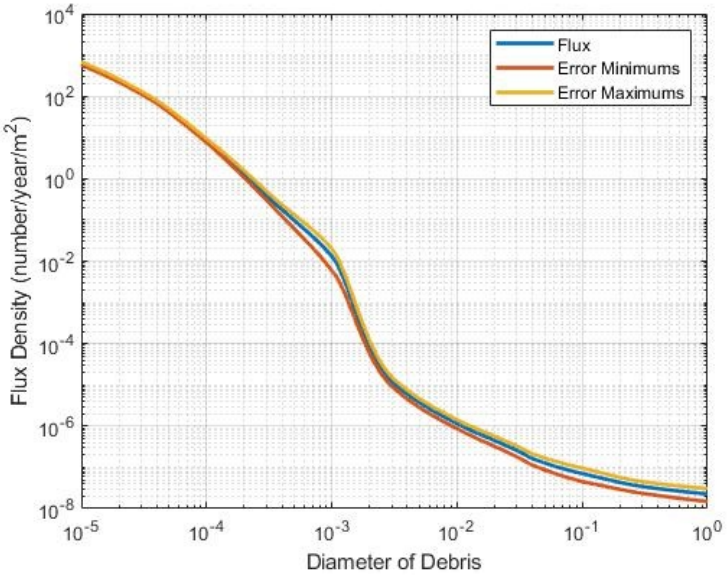

Figure 3.5: Cross Sectional Area Flux Density vs Diameter[49]

This particle flux was used to determine the probability of impact of various diameters of space debris. To determine the probability of any impact over the mission lifetime, the probability of 0 impacts was calculated using a Poisson's distribution, and then subtracted from 100%. A confidence margin is also applied, so it was assumed that any particle with greater than 1% chance of impacting the sail would impact the sail to be conservative. It was also assumed that the sail would deploy

without damage, which can be achieved through ground testing and proper integration practices and validation. If the sail is deployed with a hole in the membrane, that becomes a structural weakness and could potentially cause the sail to fail. By assuming the sail will be deployed nominally and without puncture, analysis can focus on the weakest structural components.

$$P^n = \frac{N^n}{n!} * e^{-N} \tag{3.1}$$

In equation 3.1, P_n is the probability of n impacts, N is the cumulative particle fluence, and n is an integer number of impacts[33]. With the estimated flux density, the expected impact count for various sized drag sails can be calculated as well as the probability of impact for the various debris diameters over a 25-year mission. The maximum debris size in millimeters is plotted in Table 3.1. The largest debris that is expected to impact is 4.1 mm, and would be expected to impact only the 64 m^2 sail.

Table 3.1: Largest Expected Impact for Varying Sail Areas

Sail Size (m^2)	Debris Impact Size (mm)
16	2.57
25	2.88
36	3.24
49	3.72
64	4.07

The two materials analyzed for tear propagation were 12.5 µm Upilex and 12.5 µm Aluminized Kapton based on analysis and testing[33]. Note the thickness of the membranes used in the analysis, which is as much as three times thicker than those used in other missions. Solar sailing missions often optimize for lower mass in order to maximize their characteristic acceleration (a_c), which is a ratio between total mass and sail membrane area:

$$a_c \propto \frac{SailArea}{Mass} \tag{3.2}$$

The choice of using Upilex and Kapton as the two candidate materials for sail membrane materials stems from research conducted by several institutions. Testing was conducted by the students at the University of Toronto which concluded that Upilex was a better option based on thermal properties, which was supported by independent research conducted by the European Space Agency and NASA Glenn Research Center [33, 34, 35]. The ESA study showed that Upilex film remained stable at 50K higher than Kapton of the same thickness, and showed less isothermal mass lost after testing at 350^o C [34]. NASA Glenn and Cleveland State University exposed different films to high levels of Vacuum Ultraviolet (VUV) radiation to test how the material properties changed, which is shown in 3.6. The testing showed that not only does Upilex have the largest tensile strength, but that it retained that strength through extended exposure to VUV [35].

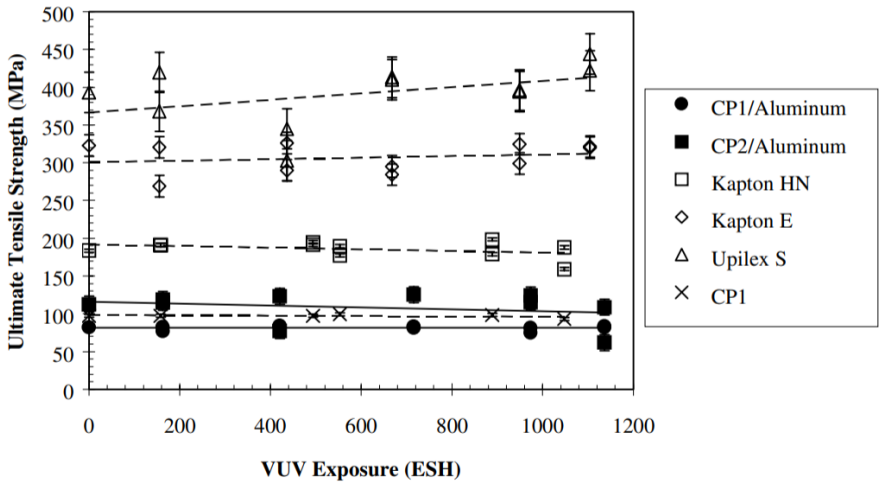

Figure 3.6: Ultimate Tensile Strength Against VUV Exposure[35]

Due to the higher expected loading and relaxed constraints on mass of the sail material itself, thicker materials were favored as they experience less stress compared to thinner sails. Student researchers at the Space Flight Laboratory at the University of Toronto Institute for Aerospace Studies identified that the stress intensity factor for Upilex was unavailable, so published values for Kapton were initially used to calculate critical loading in the sails for their analysis[33]. In house testing showed that this was a conservative assumption because Upilex was more resilient to tearing than Kapton of the same thickness[33].For this thesis, an analytical value of the stress intensity factor for Upilex was calculated and used. K_c, the critical stress intensity factor, can be estimated using the Fracture energy G_c and E representing Young's Modulus for a given material[50].

$$K_c = \sqrt{G_c * E} \tag{3.3}$$

This can be used to validate that that using the critical stress intensity of Kapton is a conservative estimate for Upilex, which is dependent on geometry as well as yield strength of the material. For varying sized pieces of Upilex and Kapton, analytical

values for K_c can be calculated and shown in Figure 3.7. Tensile modulus' for Kapton and Upilex were taken from online resources; Upilex-125S's tensile modulus is stated as 7.6 GPa, while Kapton's modulus is 2.5 GPa [51, 52]. This indicates that Upilex will require additional tension for a given sample width in order to reach its critical stress.

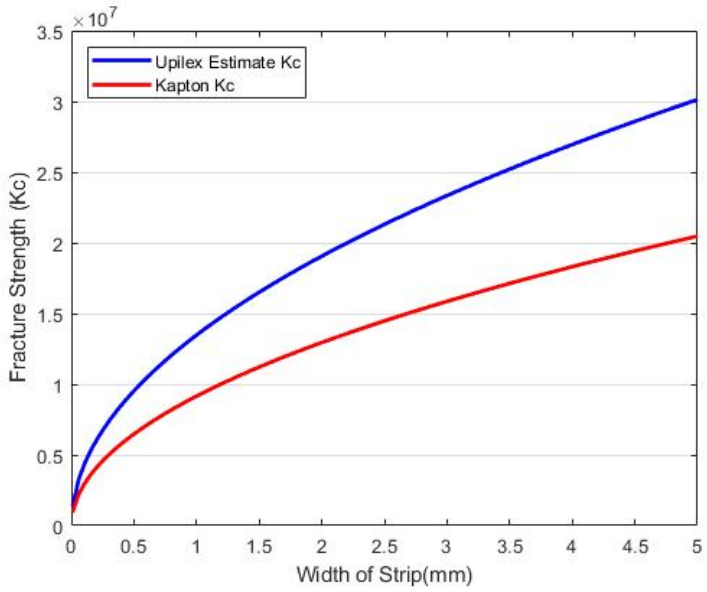

Figure 3.7: Estimate of Critical Stress Intensity for Varying Geometries

Testing has shown that the ratio of particle size to film thickness is relate to impact size for hypervelocity impacts [33]. This means that in non-brittle films, the resultant hole diameter is assumed to be the same size as the impacting particle [33]. Some sail materials become brittle due to thermal aging or as the WCH conditions bring them close to their maximum operational temperatures [33].

The weakest part of a drag sail is the connection points between it and the booms. These connections often consist of a hole in the membrane with reinforcement such as a metal grommet or additional material attaching the sail to the booms. The grommet attachment scheme was chosen because it allows the sails to expand as the booms deploy, and offers additional support for load transfer between the booms and

sail strips. This method also allows each strip to be individually folded and attached to the booms during packing, reducing integration complexity [46]. For the analysis conducted on the CubeSat sail, the worst-case loads were identified for a sail loading a single 5 mm grommet for base attachment point[33]. The loading used is pictured in Figure 3.8. The sail's geometric factor was calculated using the center-tearing case, as the edge tearing case was not physically realizable for the grommet [33].

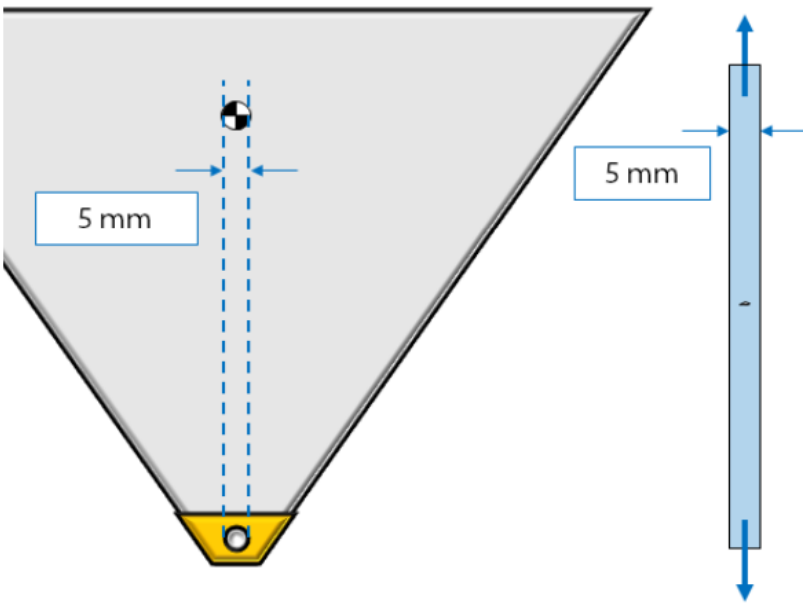

Figure 3.8: Idealized Quadrant Sail Loading[33]

For this thesis the analysis will initially be adapted and performed for the stripped sail case, although it has been identified that the stripped sail has more than one attachment point and will be attached to more than one boom[48]. A geometric factor is calculated in order to determine a critical crack length in the center tear case, as edge tearing is not realizable physically[33]. The critical crack length indicates when a crack or tear transitions from stable to unstable. For this application, the critical crack length is the diameter of the debris impact which would initiate a tear within the membrane. Below this value, the crack will not propagate. The geometric factor F is used to calculate σ_c, which is the critical stress required to initiate a tear. K_I is

the tensile fracture strength, also known as the stress critical stress intensity factor for Mode I tearing, and a is a varying crack length. Mode I fracture mechanics is defined as purely tensile loading [50].

$$\sigma_c = K_I(\sqrt{\pi * a * F})^{-}1 \tag{3.4}$$

The geometric factor can be found using eq. 3.5 and is a function of the width of the sample (W) as well as the tear length (a) for a center crack under tension[50].

$$F(\frac{a}{W}) = \sqrt{sec(\frac{\pi a}{2W})} * (1 - .025 * (\frac{a}{W})^2) + .06 * (\frac{a}{W})^4 \tag{3.5}$$

Results using available values for 12.5µm Kapton and estimated values for 12.5µm Upilex are shown in Figure 3.9. This chart shows the hole diameter required for a given tensile state to initiate a tear in the membranes. The membranes were assumed to be non-brittle, so the impact size was assumed to be the size of the debris impact. This chart will be used in conjunction with Table 3.1 to determine the max tension that the sail membranes can experience before an impact would initiate and propagate a tear. If the tension in the sail is lower than the value on the chart, the impact is not expected to propagate tearing after impact.

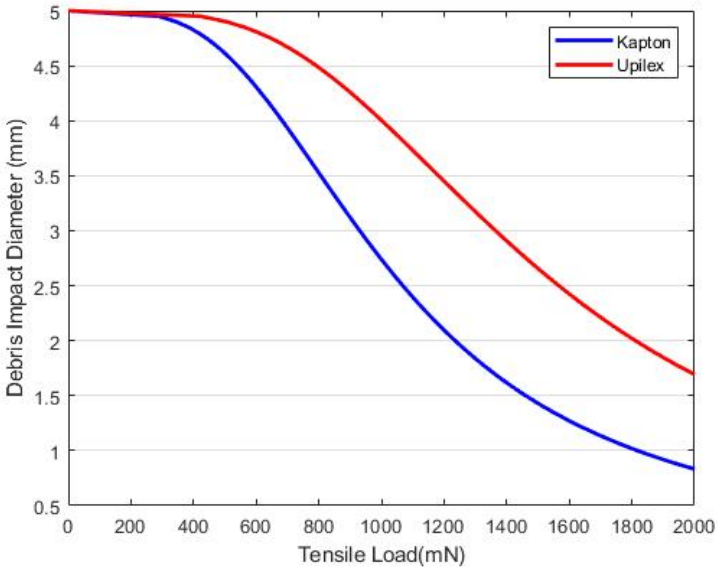

Figure 3.9: Critical Crack Length for Single Attachment Kapton and Upilex Strips

The analysis can be used to compare the expected impact size for a micrometeorite with the sail and determine the upper bound for tension that the sail can be under before tearing will occur. This information is used for a conservative estimate for tear initiation on a quadrant sail, but for the stripped sail it is more sensible to use multiple connection points. For the stripped sail, the analysis is conducted again but with a total of 2 connection points per strip. This is a more realistic attachment scheme, depicted in Figure 3.10.

Figure 3.10: Visualization of Stripped Sail Loading Assumption

The results of the analysis show that for multiple attachment grommets, the critical crack length for the sail requires a large tensile load in the strips. Figure 3.11 shows the results of the analysis given multiple attachment points for the stripped

sail compared to a single attachment point. For example, a 4 mm impact would initiate a tear in a single grommet sail if under more than 0.7 N of tension, while a double grommet sail would require 2.5 N. The loading for a given sized impact is significantly larger, further showing the benefits of the stripped sail design compared to the quadrant sail design.

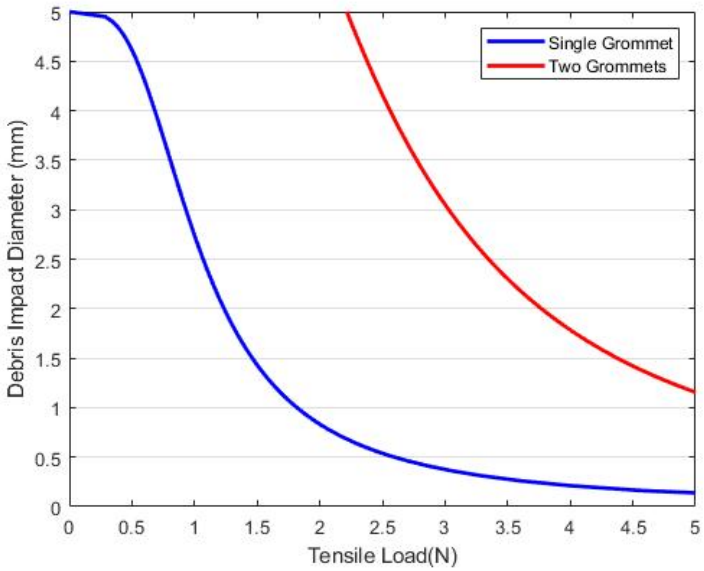

Figure 3.11: Comparison of Performance with Multiple Attachment Points

For the largest sail that was considered, a 64 m^2 drag sail, the largest estimated impact had a diameter of 4.1 mm. For this size, the drag sail strip with the two grommets must be experiencing no more than 2.5 N of tension. In order to determine if this value is reached, and that the sail may be subject to tearing, the loading on each strip must be calculated for a GTO.

To estimate the loading on the sail strips in GTO, a simulation was created. The simulation uses four launch vehicles, The Ariane 5, Falcon 9, Delta IV Heavy, and Vulcan Centaur. These vehicles were chosen because of information availability as well as the fact that they all have targeted GTO missions in the near future [40, 41, 42, 43]. There is variability with every launch and every orbit, so it was

decided to use the target orbits from the user guides for performance information. Geostationary payloads will have to circularize the orbit that they are deployed into, so launch providers often increase the perigee of the transfer orbit to reduce the ΔV requirements on the payload.

3.1.1 Sail Loading for GTO Target Orbits

For each vehicle, the orbit was calculated and propagated using MATLAB's ode45 variable step function. For each vehicle, loading is calculated for each strip throughout the orbit; Since the velocity at perigee is the largest, that is where the largest loading will occur. For all calculations, an atmospheric scale height model was used with values from mean solar activity and a C_D of 2.2. There is large uncertainty when it comes to the C_D of a satellite, but 2.2 is commonly used and accepted for space missions[53]. The values used for the atmospheric model is averaged between the MSISE-90 and the NRLMSISE-00 models[55, 56]. The solar irradiance used was 1365 W/m^2 [56]. For each simulation, sail areas ranging from 25 m^2 to 64 m^2 were used. For the sail strips, a width was used of 0.508 m, which is the width of the strips sold by UBE industries[52]. With the orbital assumptions explained, the formulation of how sail loading will be determined can be discussed.

The expected loading was calculated for one sail quadrant, which is comprised of a varying number of strips based on the total desired sail area. For each strip on the sail, the width is defined and known based on manufacturer specifications. For this analysis, the width is taken to be .508 m, as stated above. For each position in the orbit, the drag force parameter P was calculated. P represents drag without an area component, with units of $\frac{kilogram}{meter-second^2}$ rather than $\frac{kilogram-meter}{second^2}$(Newtons). This parameter will then be applied individually to each strip in order to calculate the drag acting on the strip.

$$P = \frac{C_{\mathrm{d}} * \rho * Velocity^2}{2} \tag{3.6}$$

$$D_{strip} = P * Area_{strip} \tag{3.7}$$

$$TotalDragForce = \sum_{n=1}^{N} D_{strip_n} \tag{3.8}$$

Each strip is treated as a trapezoid and numbered 1-N in Figure 3.12. The area of the trapezoid is found using the bases A and B, where for the first iteration A = α, an assumed width of 0.01 m. For each strip, B becomes A and the new area is calculated. Note that all graphics are not drawn to scale but drawn to highlight considerations in the design of the analyses used.

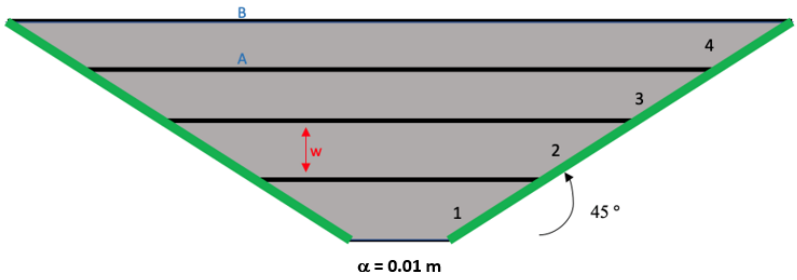

Figure 3.12: Stripped Sail Quadrant Layout

The area of a trapezoid is then calculated[57]. For this application, A and B the two bases , and w refers to the width of the drag sail strips.

$$Area_n = \frac{w * (A_n + B_n)}{2} \tag{3.9}$$

Once the area of an individual strip is known, it can be multiplied by the parameter P to calculate the force due to drag D_{strip}. Each strip is experiencing uniaxial tension, so the total drag force on the strip is set to an equivalent distributed load, shown in Figure 3.13.

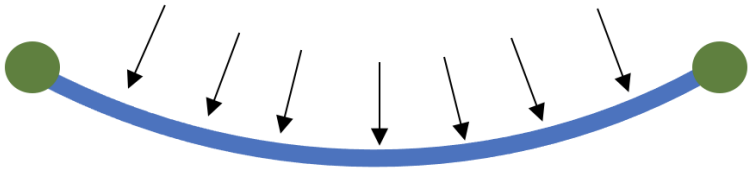

Figure 3.13: Strip Distributed Load

The distributed load can then be used to calculate the loading on the booms, moment created at the booms hub, and the stress in the sail membrane. For the stress in the sail membrane, a thin film approximation was used [58]. The sail thickness is 12.5µm while the width is .508 m and the length is greater than 1 meter. Figure 3.14 shows a cross sectional view of a sail strip. The length will be dependent on the strip number, but the width and thickness are known based on the manufacturer's specifications.

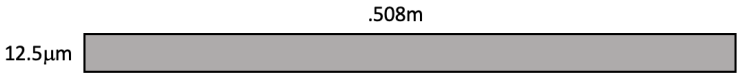

Figure 3.14: Sail Strip Cross Section

The thin film stress is then calculated for each strip.

$$\sigma_n = \frac{D_n}{.508 * 12.5e^{-6}} \tag{3.10}$$

Figures 3.15 and 3.16 show another benefit of the stripped sail design. Because two adjacent sails are under tension by the boom that separates them, the loading on the boom is reduced. Similar to the physics behind suspension bridges where the load is carried by the cables rather than the trusses, the sails are able to tension themselves using adjacent strips[59].

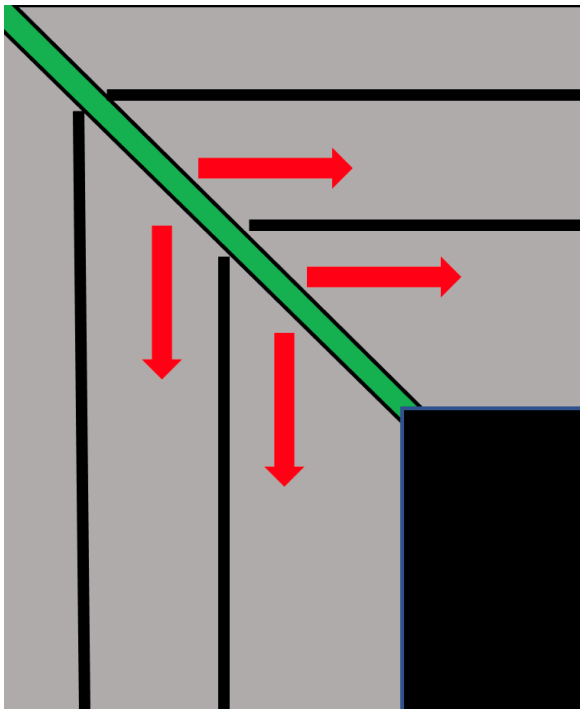

Figure 3.15: Sail Tensioning Visualized

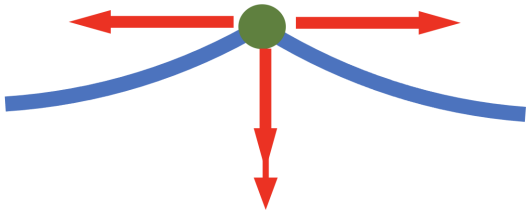

Figure 3.16: Boom Loading Visualized

It was important to pick a correct position for the loading to be concentrated when calculating the moment that would be generated at the boom's hub. Figure 3.17 shows the location of the loading for one of the booms for determining the mo-

ment created at the hub. The centroid of each strip trapezoid was used as the location of an equivalent point load. For each strip, there is a λ_n which correlates to the moment arm that it generates.

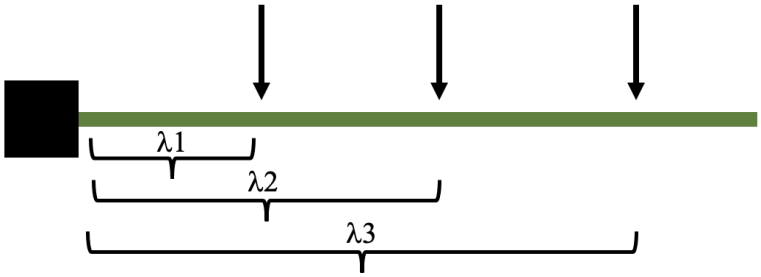

Figure 3.17: Boom Moment Generation

To calculate each lambda, the width(s) of the previous sails are added to the centroid (C_n) of the new trapezoid. For example, the third sail (λ_3), has a moment arm of 2 widths plus the centroid of trapezoid 3 [60].

$$C_3 = \frac{(B_3 + 2A_3) * w}{3(A_3 + B_3)} \tag{3.11}$$

$$\lambda_3 = 2 * (.508) + C_3 \tag{3.12}$$

Now that the formulation for calculating the strip loading, boom loading, and moment generated at the boom hub have been described, the simulation can be performed.

The calculations were carried out for drag sails ranging for areas ranging from 5 m^2 to 64 m^2, and for each launch vehicle the orbit was propagated from apogee through perigee. The maximum tension in one of the strips for each launch vehicle was calculated and is shown in Figure 3.18. The largest tension occurs in the Falcon and Vulcan rockets, which is due to their lower target perigees.

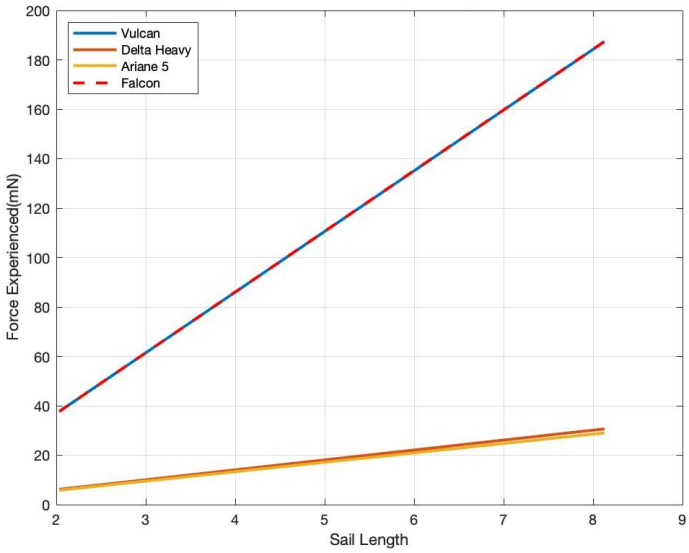

Figure 3.18: Tension in Sail Calculated

The Falcon's target GTO is 185 km x 35943 km, and the Vulcan's is 185 km x 35786 km[40, 43]. The Falcon 9 and Vulcan rockets experienced the highest loading, since they have a lower target perigee compared to the other vehicles. Now that the expected tensile load is calculated, it can be verified whether or not the stripped sail design will propagate tearing. Recall that for the 64 m^2 sail with a single attachment point, a 4.41 mm impact was estimated; Correlating to a tensile load of 850 mN for tear initiation.

For multiple grommets, the 4.1 mm impact required over 2.5 Newtons of tension in the sail for tearing to initiate. The orbital analysis showed that the sail would be expected to reach almost 200 mN, which is below the threshold for tear initiation; This shows that the sail membrane consisting of strips of 12.5µm Upilex film is expected to survive the loading it would experience in a GTO.

Radiation may weaken or degrade the sail material over time. By passing through the Van Allen Belts, the sail will experience high doses of radiation throughout its mission. During testing performed by NASA, the samples of Mylar that ranged 1.6 µm thick to 2.1 µm thick and were subject to Gigarads doses of radiation and 5000 psi (34 MPa) of initial stress [31]. Although the strips tested by NASA were significantly less thick than the selected Upilex material, comparisons can still be performed to see if the material would fail the test the same way that some of the materials that NASA tested did. Using the thin film approximation, the tension in the sail material can be calculated and displayed in Figure 3.19.

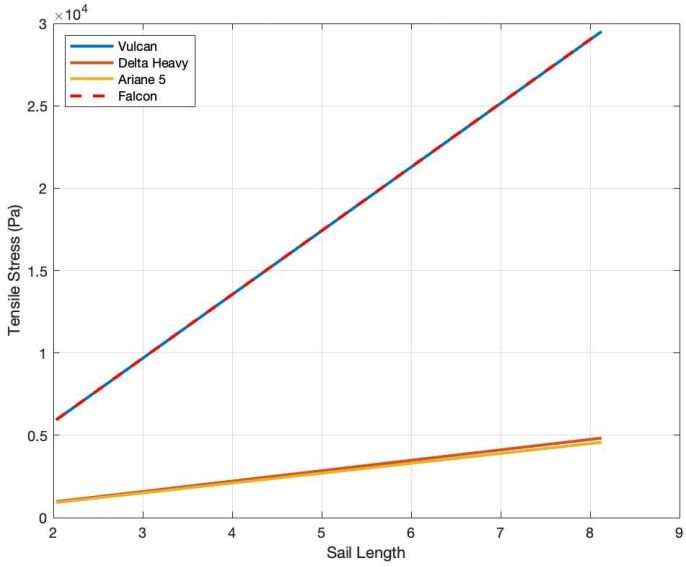

Figure 3.19: Estimated Stress in Strips

The max stress expected in the strips was 30 MPa. None of the aluminized strips that NASA tested failed while under similar loading conditions, while also being thinner materials[31]. Despite these conclusions, long duration environmental testing is the only way to verify whether or not the Upilex film will survive extended periods of high level radiation from the Van Allen Belts.

A concern that arrived from analyzing the loading was the moment created at the boom hub. Figure 3.20 shows the expected maximum moment at the boom hub based on the launch vehicles, orbits, and sail sizes. The moment arm grows exponentially as the sail size grows, which shows that there may be an upper bound for sail sizing when the structural mass required to withstand the moment at the boom hub may become too massive. For a 64 m^2 sail, which is comprised of 8 strips, the expected moment at the boom center for each boom approached 3.04 N-m. For the same analysis conducted on a quadrant sail, where the moment generated by drag acting on each strip is concentrated at the boom tips, the resultant moment was 4.31 N-m. The reduction in the moment generated at the boom hub is due to the distribution of the loading along the length of the boom by the stripped sail design, resulting in lower rigidity and structural strength requirements for the booms.

Boom design is not within the scope of this thesis, and a design would most likely need to be created for this specific application based on a finalized size. Several structural concepts for large scale deployable booms have been researched and designed over the last few decades [61]. One example boom designed for a stripped sail design used Finite Element Analysis (FEA) to observe its buckling behavior. Testing was then conducted on an optimized design, which experienced buckling at 45.4 N-m during testing of its weakest axis[61]. The mass breakdown of this sail will be scaled in order to calculate a mass estimate of the booms for this thesis.

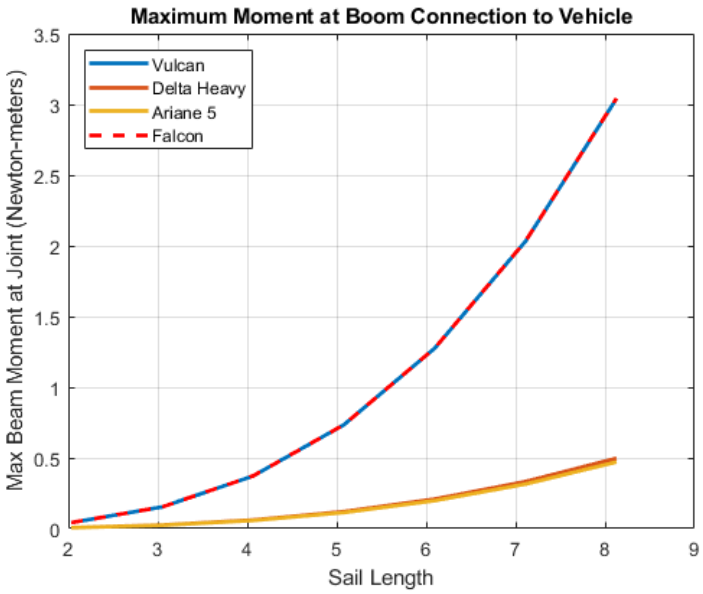

Figure 3.20: Estimated Moment at Boom Connections

Finally, it must be considered whether or not the drag sail system conforms to the mass and volume constraints of a CubeSat Dispenser with CubeSats inside. Boom mass is approximated as 100 grams/m based on experimental results and analyses, and Upilex 12.5 µm film as an area ratio of 54.4 m^2/kg[54, 63]. For the pure sail-boom system, a 64 m^2 sail would have a mass of 1.176 kg, and the booms would have a mass of 2.26 kg.

$$Mass_{sail} = \frac{1kg}{54.4m^2} * 64m^2 = 1.176kg \tag{3.13}$$

$$Mass_{booms} = 4 * \frac{100grams}{meter} * \frac{8 * \sqrt{2}}{2} meters * \frac{1kg}{1000grams} = 2.26kg \tag{3.14}$$

Resultant mass of the sail-boom system of 3.43 kg. To make a conservative estimate as well as account for additional hardware required for mounting and fastening the system, this is multiplied by 1.25 giving a mass of 4.28 kg. To account for structural mass, it is assumed that the structure of the sail system is equivalent to a standard mk.III PPOD dispenser mass of 3.01 kg [64]. The total estimated system mas for a 64 m^2 deployable drag sail system is 7.32 kg. The total mass for each sail size was found using the same analysis and summarized in Table 3.2. To estimate the preliminary volume that the stowed sails would require, the volume pre-deployment to post-deployment for LightSail-2 was calculated and used. LightSail-2 was stowed in a 2U volume, which is 20 cm x 10 cm x 10 cm or 2000 cm^3. The final volume is calculated from the area of the sail (32 m^2) times an assumed thickness of 2.50 cm taken from the boom thickness [10]. This results in a volumetric deployed to stowed ratio of 400:1. This ratio was applied to the sail areas used in this thesis to estimate their stowed volume, assuming the same deployed thickness of 2.50 cm that was used for the LightSail calculation. For reference, the total volume of a mk.III PPOD is approximately 8295 cm^3 [12]. The volumetric calculations are summarized in Table 3.2. The estimated volume of all the sails is less than the total volume of a mk.III PPOD, providing confidence that a potential drag sail design could be integrated to the same platform that a PPOD can. It must be noted that the large sails might run into issues with storage as the booms may not be able to be placed adjacent to each other due to volumetric constraints. Analysis would need to be conducted to determine how boom and sail quadrant placement affects performance, meaning if the sail quadrants are placed one on top of the other rather than co-planar.

Table 3.2: Estimated Sail System Mass Based On Sail Area

Sail Size (m^2)	$Mass_{Sail}$ (kg)	$Mass_{Booms}$ (kg)	Total System Mass (kg)	Est. Volume (cm^3)
25	0.46	1.414	5.34	1526.5
36	0.66	1.697	5.95	2250.0
49	0.91	1.979	6.62	3062.5
64	1.18	2.267	7.32	4000.0

Given that the pre-deployment mass of a mk.III PPOD is 7.010 kg, and that larger, more massive dispensers are being flown, it is feasible that even a 64 m^2 deployable drag sail device could utilize the same interface without greatly affecting the mass distribution. For example, although the dispenser mass was not available, the ISIS space ISIPOD 3U CubeSat dispenser can support payloads of up to 6 kg, which doesn't include the mass of the dispenser itself [65]. Using a smaller sail, the mass of the deployable drag sail system would be less than a fully integrated PPOD.

3.2 Efficiently Modeling Long Term Orbital Progression of Launch Vehicle Stages and Satellites

Since it is feasible that a large drag sail could be mounted onto a launch vehicle, the next step is to understand how the sail's size affects the amount of time that the rocket stage remains in orbit. A large sail may perform better, but performance must also be traded with mass and cost. A lower cost, less massive sail may have more opportunities to fly or be more inviting for launch vehicle. This section discusses the development of a model for determining orbital performance of drag sails in GTOs. First, the model design and formulation will be introduced, followed by any relevant assumptions and model validation, and then lastly the model will be applied to candidate launch vehicles to determine how the inclusion of a deployable drag sail device will impact the amount of time they are in orbit.

Drag on a spacecraft is calculated using the exposed cross-sectional area, or wet-

ted area. This excludes sections or areas that are not exposed to the flow field. This is important because the drag sail may not be fully exposed based on the current orientation of the launch vehicle. A drag sail integrated near the payload adapter has the potential to create a large moment arm about the center of mass, which may impact stability and cause the vehicle to rotate or spin in an undesirable fashion. One example of how the drag sail is integrated to the launch vehicle can be found in Figure 3.21. The Z-axis of the vehicle is directed towards the right side of the page, the Y-axis is directed out of the page, and the X-axis is directed towards the top of the page. Note the asymmetric placement of the drag sail represents the radius of an ESPA ring to simulate the sail itself being integrated to one of the ports on the adapter.

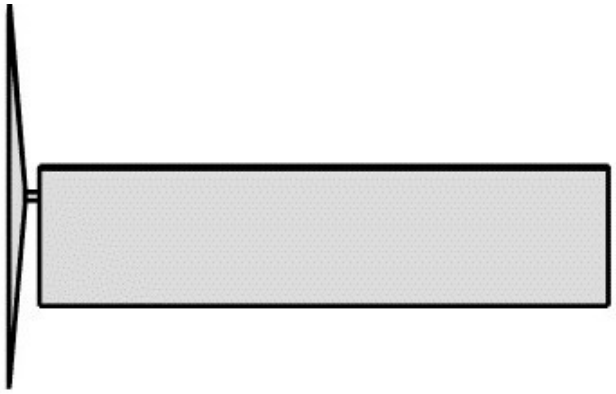

Figure 3.21: Example Stage with Drag Sail

The unique geometry of the system means that changes in attitude or orientation present large impacts on the wetted area. A unique approach is adapted for calculating the projected cross-sectional area (PCSA) that was originally used for a CubeSat application[66].

3.2.1 Assumptions

Constants are introduced and summarized in Table 3.3, and assumptions with rationale.

Table 3.3: List of Assumptions for Orbital Analysis

Assumption	Value
Starting True Anomaly	180^o
Initial Attitude wrt LVLH [roll, pitch, yaw]	[0,0,0] degrees
Initial Inertial Angle Rates [roll, pitch, yaw]	[0,0,0] degrees/second
Solar Irradiance	$1365 \frac{Watts}{meter^2}$
Angular Velocity of Earth	$72.9211 * 10^{-6} \frac{rad}{sec}$
Coefficient of Drag C_D	2.2
Coefficient of Reflectivity C_R	1.4

The initial attitude and attitude rates were chosen to be 0, despite noting earlier that launch vehicles have spin stabilization capabilities of up to 30 degrees/second in the roll axis. Not all spacecraft are spin stabilized before deployment, so it was decided to assume no angular velocity at deployment. Assuming spin stabilization for the analysis may impact the results of the simulation, as angular velocity about a single axis would result in the sail not contributing as much to the attitude of the spacecraft. Large spin rates result in the sail-vehicle system spinning about that axis only, adversely affecting the sails ability to modulate the drag on the vehicle. In its current state, Ariane Space spins their second stage to 45 degrees/second for stabilization after payload separation, although this is only a temporary measure as the rocket will naturally revert to spinning about its major axis after some time[44].

True anomaly, the angular position of the body, was chosen to be 180^o so that the body starts at apogee. This is the most realistic time which the sail will be deployed, with the launch vehicle's payload deployed.

The solar irradiance was assumed to be a constant 1365 $\frac{Watts}{meter^2}$ based on available online resources for mean solar activity, although it is known to fluctuate[58, 67]. The angular velocity of the Earth was chosen based on published values used by NASA and represents the angular velocity of the Earth at the equator[68].

The coefficient of drag is a dimensionless parameter that describes how the body reacts to the surrounding medium. It can be determined through experiments or FEA, but 2.2 was chosen as a conservative estimate for cylindrical shapes as it is dependent on geometric factors and orientation which may change throughout the orbit [69, 70]. It is important to note that the coefficient of drag changes based on altitude, as vehicle materials react differently with the different components of the atmosphere, which is also changing composition.

The coefficient of reflectivity of 1.4 is a common assumption for materials, although values typically range from 1.1 to 1.9 [70, 71, 72]. A C_R of 2 indicates that the body reflects all of the incident light, while a C_R of 1 indicates that the body absorbs all of the light and a value of 0 indicates that the light passes through the body. Choosing 1.4 represents a conservative estimate for the reflectivity of the rocket body, which are typically painted in a more reflective paint for thermal reasons. Materials are often subject to degradation after long duration space missions, which may result in changing C_R s. The value of C_R and C_d will impact the perturbations that are experienced during the mission. These assumptions do not have major impacts on results, which are shown in Figure 3.33.

There are numerous orbital perturbations that can be included in a simulation or model that impact a spacecraft's attitude and orbit. The decision must be made then on whether or not to include a certain perturbational effect. Only Solar Radiation Pressure(SRP), Drag, and Gravity Gradient(GG) torques were included in this analysis. Other perturbations such as the n-body perturbation, in which other celestial bodies such as the Sun and the Moon impart gravitational acceleration onto the body,

were not included. Other perturbations such as non-spherical Earth perturbations were also not included, as they may rotate the orbit but do not directly affect its altitude. SRP was included because as the satellite moves towards its apogee, the atmospheric density and thus the drag force are diminished. The large, reflective surface of a drag sail may act as a solar sail, either lowering or raising the orbit. The GG torque was included because it will affect the spacecraft's attitude throughout its orbit and can change its orientation with respect to drag and the relative velocity vector.

Other assumptions made about the vehicles themselves are resultant of information not being widely available online. The center of mass for each satellite was assumed to be at the geometric center, which seems reasonable as an empty rocket stage will most closely resemble a hollow cylinder. It was also assumed that the spacecraft are all homogeneous, meaning every face has the same C_D and C_R and that the craft has uniform density. Uniform density was an important assumption for calculating inertial properties, as only dry masses were available for the vehicles. These masses had to be forced in the models that were created, and then inertia tensors could be exported based on the geometry created.

Initially the location of the Sun with respect to the Earth was calculated using MATLAB's planetEphemeris() function[74]. The function was originally used to calculate the location of the Sun in the Earth Centered Inertial (ECI) frame but proved cumbersome and was making the model slow. Instead of removing the function completely, it was decided to update the Sun's position using the planetEphemeris() function once per year. For the duration of the year except for that day, a universal variable (UV) solver was used. The UV solver is a generalization of Kepler's equation, and solves for the position and velocity of an object given a starting orbit and velocity. The time step chosen for moving the Sun vector was chosen to be one day, or every 86,400 seconds, as the Sun is not expected to move very far in that amount of time

and it makes the simulation more efficient. The dominating perturbation that will affect the drag sail's performance is drag. Given the Sun's distance from the Earth is roughly $1.49*10^8$ km, a positional error is acceptable for the increased computational efficiency of the simulation and will not have a large impact on the results.

3.2.2 Polygonal Modeling Approach

The model adapted for this thesis was originally designed for control modes of small satellites such as CubeSats[66]. Different control modes may be desired for either minimizing drag or pointing to a specific orientation for tracking or Sun pointing. An analytic method for determining the exposed surface area of any satellite is developed based on the theory of convex polygons. The methodology accounts for overlapping polygon projections and offers an efficient manner to calculate the cross sectional area throughout an orbit. The model was created and then against the Space Autonomous Mission for Swarming and Geo-locating Nanosatellites mechanical model for validation[66].

There are two important reference frames for the formulation. First, $\boldsymbol{B}$, the body reference frame. The origin of the $\boldsymbol{B}$ frame is located at the center of mass of the vehicle, which is also the geometric center in this case.The axes [x, y, z] align with the principal axes of inertia. This is why the assumption of homogeneity for the models is important. The second frame is the $\boldsymbol{W}$, which is a coordinate system that is created at each iteration of the model. The $\boldsymbol{W}$ frame is created with respect to $\mathbf{k}$, which is a desired vector in the $\boldsymbol{B}$ frame. This vector $\mathbf{k}$ will represent the relative velocity to the atmosphere for calculation of drag, and the Sun-satellite vector for calculation of SRP. The origin of the $\boldsymbol{W}$ frame is located at the center of mass, and x_k and y_k make up a fundamental plane normal to the vector $\mathbf{k}$.

The z_k axis is directed along **k**. Figure 3.22 shows a representation of the ***W*** frame projection (blue) compared to the ***B*** frame (red).

The ***W*** frame allows the 3-dimensional representation of areas to be represented into a 2-dimensional space that is normal to the desired vector. Graphically, the ***W*** frame allows for the wetted area normal to any desired area to be calculated for each iteration of the model. Compared to Figure 3.22, Figure 3.23 shows the W frame representation of the same model with respect to the ***W*** frame.

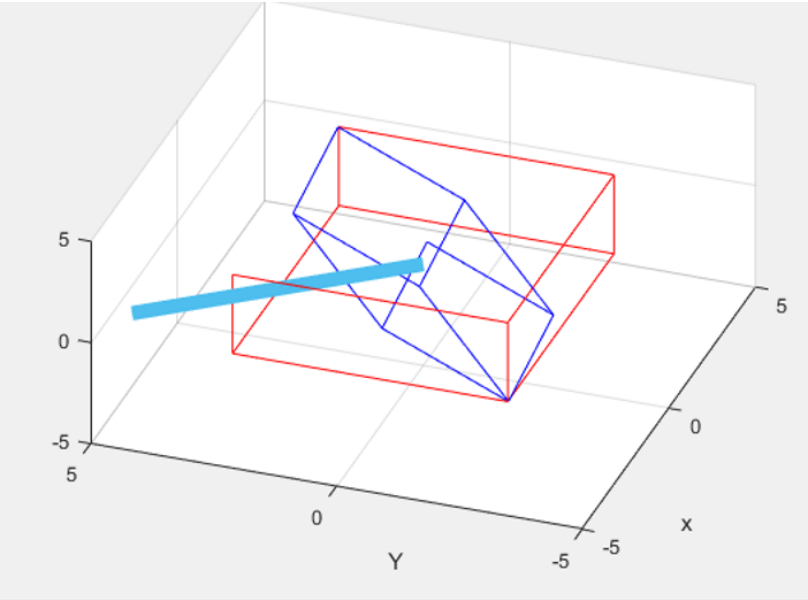

Figure 3.22: Example *B* Frame Representation

In Figure 3.22 the red outline shows a rectangular spacecraft shown in the body frame, the cyan vector represents the desired vector,chosen arbitrarily for this example, and the blue outline is the projected area of the red frame in the ***W*** frame. The same model and time step can also be shown explicitly in the ***W*** frame in Figure 3.23. The 2-dimensional representation of the 3-dimensional system can be clearly seen. The plane created by the **W** frame can be denoted as S for future discussion.

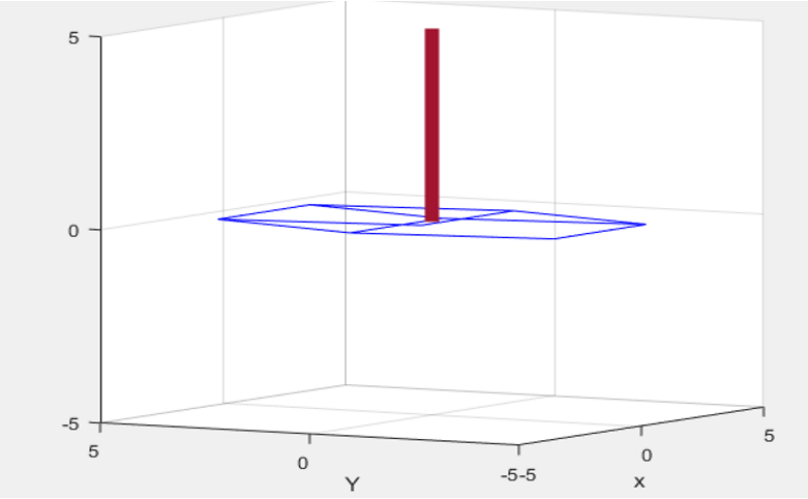

Figure 3.23: Example *W* Frame Representation

One of the difficulties of the polygonal modeling scheme is that cylindrical bodies must be converted into a series of polygons for the analysis. The size of the representative polygons must be calculated with respect to the reference cylinder's shape. As an assumption, polygonal approximation of cylindrical bodies is acceptable because the cross-sectional shape of the two is the same when looking broadside. The only area-based difference occurs when looking along the center line of the cylinder, in which case there will be some difference between the two shapes. Typically, the drag experienced by a vehicle is calculated by integrating the differential drag force d_F with respect to each surface element d_A. Eq. 3.15 shows how d_F is calculated, with $\hat{v}$ representing the unit vector of the velocity of the body relative to the medium and $\hat{n}$ representing the outward unit vector normal to surface element dA.

$$d_F = -\frac{1}{2}\rho v^2 C_D(\hat{n} \cdot \hat{v})\hat{v} * dA \tag{3.15}$$

By using a discrete number of polygons which are projected, the total drag force D_F can be instead calculated by:

$$D_F = -\frac{1}{2}\rho v^2 \hat{v} \sum_{i=1}^{N} C_D A_i' \tag{3.16}$$

Here A′ represents the projected area of polygon A_i onto the **W** frame. A similar approach is applied to calculation of the torque on the vehicle. Since D_F acts opposite to the direction of $\hat{v}$, the torque generated $\mathbf{N}_{drag}$ is normal to $\hat{v}$. Moreover, since the **W** frame is located at the center of mass and normal to the desired vector, drag in this case, so the torque **N** must lie in the plane S created by the **W** frame. The result of this conclusion is that the torque due to drag or another perturbing force can be calculated using the same methods as the force acting on the polygons.

$$N_{drag} = -\frac{1}{2}\rho v^2 \sum_{i=1}^{N} C_D A_i' (R_{ci} \text{ x } \hat{v}) \tag{3.17}$$

The notable change is that R′ is the distance from the center of mass to the center of mass of the projected element dA, which translates to the centroid of the projected polygon when calculating the total torque. Initially, simulation was conducting using MATLAB's ODE45() function[75]. The solver is designed to work well with non-stiff differential equations and using a variable time step for solving the equations. The issue arose when computation times were first assessed. Initially, the first 100 days of simulations would take more than 6 hours and began to slow down due to memory limitations. Efforts were made to optimize the solver taking advantage of MATLAB's ability to efficiently do matrix math, but ultimately another solution was desired.

The solution that was selected was to adopt an Encke's Method based numerical integration scheme for both the orbit and attitude, represented graphically in Figure 3.24 [76, 77, 78]. Encke's method begins with an osculating orbit as a reference, which contains no perturbing accelerations. For each discrete iteration, a perturbed orbit is

also calculated, and rectified with the osculating orbit at designated intervals. The benefit of using this method is that larger time steps can be taken with accuracy being maintained, with the caveat that rectification must occur periodically. It is common for rectification to occur once per orbit, but it is highly dependent on the perturbations as well as the orbit itself [77]. For this implementation, the rectification occurs at every iteration(δ_r), as the computational speed improvement was already much faster than the ODE simulations. A 100 day simulation using the ODE45 simulation took more than three hours to complete, while the same simulation using Encke's method took roughly 240 seconds.

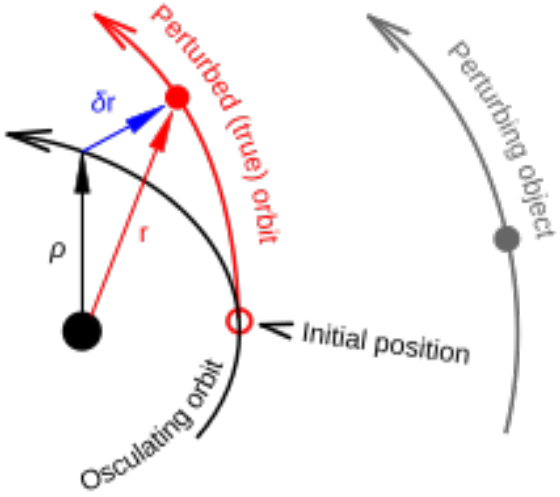

Figure 3.24: Encke's Method Visualized [78]

Encke's method allows the user to take larger time steps, but that can greatly impact the accuracy of highly dynamic systems. For example, on orbit a time step for a spacecraft with small angular rates may use a time step of 20 seconds, as the angular rates are not expected to vary largely in that amount of time. For highly dynamic systems, for example those with thrusters or attitude control systems which may create large instantaneous torques, Encke's method loses validity. This is because for the entire discrete time step, the torque that was calculated would be applied to the

spacecraft. Encke's method is useful for this application as the spacecraft is not being actively controlled and thus not expected to experience large, sudden torques. For a majority of the orbit when the spacecraft is away from perigee, the torques will be continuous and gradual, which leads to small differences between the osculating and perturbed orbits created in the method. Each discrete time step in the method, the $\mathbf{W}_{velocity}$ and $\mathbf{W}_{Sun}$ are created. The projected polygonal area of the target spacecraft is then calculated for both frames, followed by the torques for those perturbations. For each iteration, the first calculation is whether or not the vehicle is in eclipse, and the SRP calculations are skipped if the vehicle is eclipsed.

3.2.3 Model Validation

The methods used in the simulation have been described and now must be verified. Two options were initially considered for verification. The first option would be to compare the results of the model with another that is commonly used in industry, such as AGI's System Tool Kit (STK) or NASA's General Mission Analysis Tool (GMAT). The second option, which was ultimately selected, is to select real-world object of varying specifications that have deorbited and compare the model's results with what really happened.

The determination to conduct verification through the use of candidate missions was due to two factors. First, using real missions to verify the model would test assumptions that the model used, allowing for full front-to-back testing on the candidate missions. Use of another model for verification such as GMAT would mean that it would be potentially harder to assess what assumptions are responsible for any discrepancy.

Another benefit is that the method for creation of the models used by the model is tested. The information available online for most missions is rudimentary, often giving limited dimensional data and only a dry mass for the entire vehicle. This meant that interpolation of some dimensions was required. This also shows the important of the homogeneous assumption, where the dry mass can be applied to the entire vehicle.

Three candidate missions in LEO were selected to verify the accuracy of the model. The goals of the verification process is to apply the model to the selected candidate missions and determine how closely it matches their true decay orbits. The objects were selected to be in varying LEO orbits, as well as varied masses and shapes to best test the area calculation as well as the atmospheric model created. It is important to have verification of the model especially in LEO since the primary mechanism of the drag sail is its interaction with the atmosphere.

The data for the LEO candidate missions is tabulated to show the unique characteristics. The first mission is ROSAT, was an X-ray observatory launched in 1990(Figure 3.25) [79]. ROSAT deorbited on October 23, 2011, over 21 years (7800 days) in space. The model of ROSAT in Figure 3.2.3 that was used for the simulation relied on online information about both the satellite and its payload.

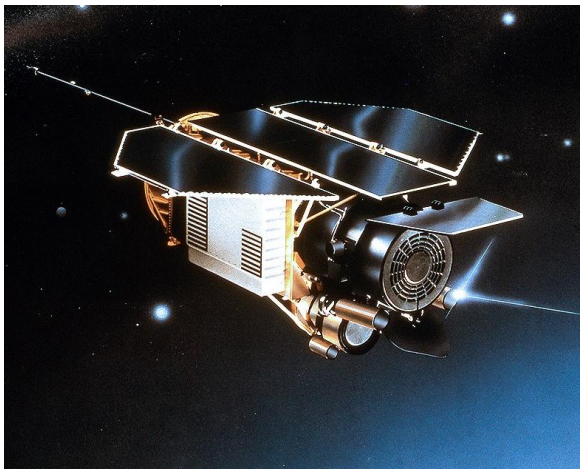

Figure 3.25: ROSAT Satellite[79]

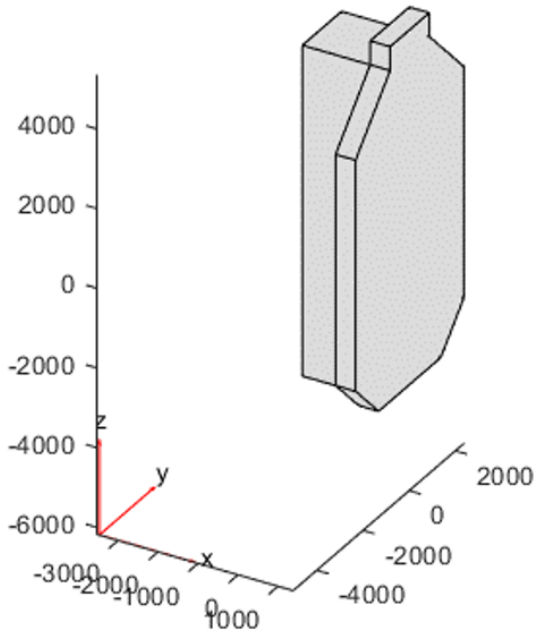

Figure 3.26: ROSAT Model (units in mm)

The next mission considered was the Tianggong-1 Chinese Space station, shown in Figure 3.27 [80]. At 8500 kg, the station was the largest candidate mission. It also is primarily cylindrical, similar to the rocket bodies that the model is trying to approximate. Since it is cylindrical, it will need to be modeled as a series of polygons

much like how rocket stages will be, which has been identified as one of the challenges with the polygon-based modeling scheme. The station lost control in 2016, with the China Manned Space Engineering Office announcing they had officially disabled service and ended the mission in March. The TLE used in the analysis is from May 2017 to ensure that it was during the regime of uncontrolled flight.

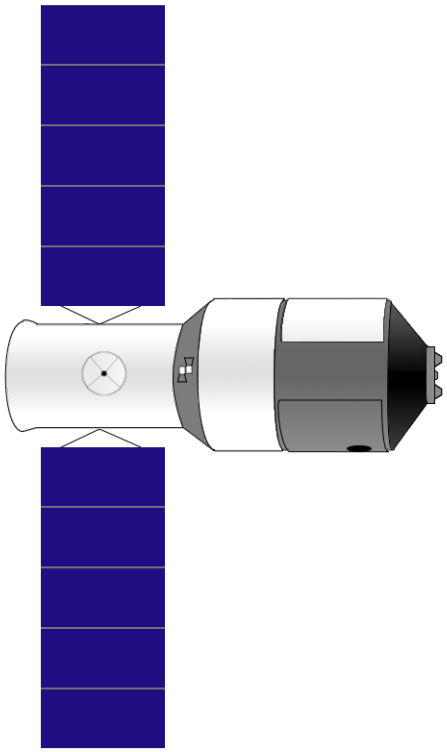

Figure 3.27: Tianggong-1 [80]

The final LEO candidate mission is the GeneSat CubeSat launched by NASA and several universities [81, 82]. The 3U CubeSat is the smallest candidate mission, both in terms of volume and mass. It also has a high ballistic coefficient, which is a function of area and mass.

The selected candidate missions comprised a wide range of orbits, shapes, and masses which will test the validity of the model created. The missions are summarized in Table 3.4, which includes their mass, launch date, and the initial orbit that they were propagated from.

Table 3.4: LEO Candidate Mission Parameters

Satellite Name	Mass (kg)	Launch Date	Orbit
ROSAT	2420	June 1990	580 km x 580 km
Tiangong-1	8500	May 2017*	327 km x 328 km
GeneSat	4	Dec 2016	413 km x 420 km

*Last controlled TLE data

For each mission, the satellite's orbit was input into the simulation and a model was created to represent the satellites' geometric features. Each mission was propagated from the starting date until it reached an altitude of 100 km. This height is sufficient for determining that the satellite will deorbit and is widely accepted for determining when to end simulations of orbital decay. Once a deorbit date was calculated, it was compared with when the candidate satellite naturally decayed. By looking at the difference between the model's estimate and what really happened, the accuracy of the model was checked. The results from the simulations are in Table 3.5. The model was able to predict the decay date of the missions whether the mission was in space for less than a year or more than 20 years. This level of accuracy is sufficient for determining how a drag sail will impact the longevity of a rocket stage since the rocket stage without the sail sometimes requires decades more than the 25-year guideline to deorbit.

Table 3.5: Candidate Missions Simulation Results

Satellite Name	Real Days in Space	Simulated Days in Space	% Error
ROSAT	7814	7873	0.75%
Tiangong-1	327	328	0.3%
GeneSat	1327	1230	7.2%

It is evident that the model is capable of efficiently propagating orbits over long time frames. Recall the function of the model is to effectively propagate orbits over long time frames so that it can be applied to GTO launch vehicle stages, which may take several decades to deorbit. Accuracy is important, but the determining factor is not that the model can accurately predict deorbit date to the day. The goal is to assess the model with a variety of candidate missions to see how certain inputs affect performance.

For the ROSAT mission, which was in space over 21 years, the model was able to predict the decay date of the satellite to within 2 months. For Tianggong-1 and GeneSat, the model was also able to predict their decay date within 10% of the true date. The GeneSat mission experienced more error with regards to the number of days in space, which could be attributed to the mass distribution in the satellite causing a more prevalent gravity gradient torque to be experienced. The satellite's internal volume was $\frac{2}{3}$ payload, meaning that the center of mass may have been offset significantly [81, 82]. Figure 3.28 shows an illustration of the CubeSat, which shows that the payload takes up a majority of the internal volume. The CubeSat standard allows for $\pm$ 7 cm, which means the assumption of a geometric center of mass may have led to the additional error of the simulation [12]. The accuracy of the model for these missions indicates that it is accurate for a large range of space vehicle masses and geometries, also showing that the atmospheric model being used can accurately represent the density through various changes such as solar cycling.

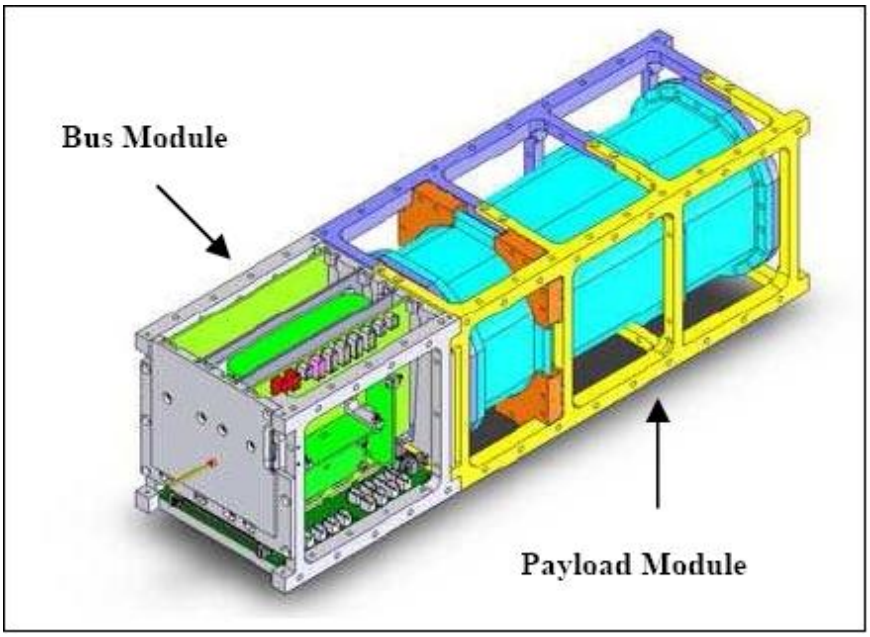

Figure 3.28: GEneSat Illustration of Payload [82]

In addition to the three LEO candidate missions, a GTO mission was also simulated. A GTO candidate mission was selected to check if there were any errors in the model for higher altitudes, as the LEO missions only tested the model under 1000 km. The GTO candidate mission would allow for testing of the model from altitudes of 1000 km to 35800 km. There are unique challenges with comparing the simulation to a GTO orbit, as many GTO objects are in orbit for decades or centuries. The simulation will instead use the initial Two Line Element (TLE) set and propagate it to the most recent TLE. An Ariane 5 rocket body was chosen, as a model for the Ariane 5 second stage was already in the process of being created for this thesis. Space-Track.org was used to determine the latest TLE for the object as well as the initial TLE, which are summarized in table 3.6 [83]. The initial TLE is from September 15, 2000, and the second is from May 8, 2021(NORAD number 26110). The propagation using the simulation will thus be used to propagate the first TLE for 7539 days and then be compared with how the stage's orbit has really evolved.

Table 3.6: Ariane 5 Candidate TLEs [83]

ARIANE 5 R/B (09-15-2000)
1 26110U 00016D 00258.11279397 .00000025 00000-0 83779-3 0 9995
2 26110 006.8906 282.9589 7083767 304.2391 007.5840 02.27135613 4002
ARIANE 5 R/B (05-7-2021)
1 26110U 00016D 21126.60491007 -.00000220 00000-0 16951-2 0 9995
2 26110 7.1447 14.1186 7098116 30.9350 356.1129 2.27182468175378

The orbit initially was 751 km x 35385 km with a semi-major axis of 24446 km. After 20 years and 7 months in orbit, or 7539 days in space, the new orbit that the satellite is in is 715 km x 35414 km with a semi-major axis of 35380 km. It is apparent that this stage will not meet the IADC's guidelines, as almost 21 years have passed since it launched its payload and it remains in such a high orbit. The initial orbit was input into the simulation and propagated for 7539 days using a time step of 20 seconds. At the conclusion of the simulation, the final perigee and apogee were calculated to be compared with the true orbit. It's important to note that since SRP, Drag, and GG torques are the only perturbing forces that means the orbital plane is not going to experience any rotation. Figure 3.29 shows how the final orbits in 2021 differ, with the blue orbit representing the propagated simulation starting from the year 2000 and the orange orbit representing the final orbit taken from the TLE. Note that the orbits are not aligned, which is due to the excluded perturbations which cause the orbit to rotate.

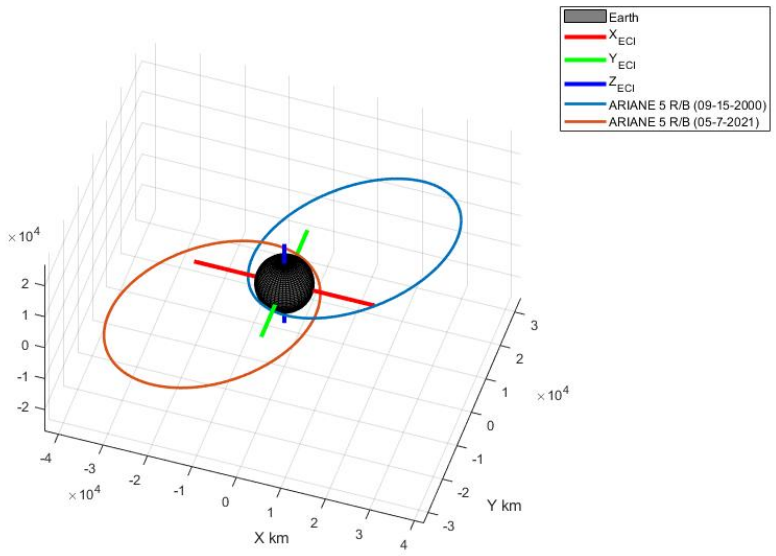

Figure 3.29: Simulated vs Real GTO Candidate Orbit

To check for validity, the perigee, apogee, and semi-major axis compared for the 20-year simulation and a percent difference is calculated.

$$\Delta apogee = \frac{|35414 - 35380|}{\frac{35414+35380}{2}} * 100 = 0.096\% \tag{3.18}$$

$$\Delta perigee = \frac{|715 - 751|}{\frac{715+751}{2}} * 100 = 4.91\% \tag{3.19}$$

$$\Delta SMA = \frac{|24442.5 - 24443.5|}{\frac{24442.5+24443.5}{2}} * 100 = 0.0041\% \tag{3.20}$$

The results of the calculation show that the model is able to propagate the GTO mission without divergence from what really happened. This verifies that the model represents an efficient way to model decade-long term orbital activity, and can be applied to the target launch vehicles in the next section.

3.2.4 Application of Model to Launch Vehicle Target Orbits

With the model validated, the next step was to apply it to target launch vehicles. Each launch vehicle has a user guide which describes its target transfer orbit for payloads to GEO [42, 43, 44, 45]. Summarizing the user guides in Table 3.7, these target orbits can be used with the model to determine whether or not that vehicle will deorbit by itself within the 25-year IADC guideline.

Table 3.7: Launch Vehicle Target GTOs

Launch Vehicle	Target Perigee (km)	Target Apogee(km)	Target Inclination(deg)
Ariane 5	250	35943	6.0
Delta IV Heavy	231	35902	27.0
Falcon 9	185	35800*	28.5
Vulcan Centaur	185	35786	27.0

* Target apogee unknown or not listed

For each launch vehicle, a model had to be created for the model to input and generate vertices from. Dimensions for each vehicle were found online, and summarized in Table 3.8 [42, 43, 44, 45]. The Ariane represents the smallest vehicle in volume but also the most massive, which is why it will be focused on for some of the later discussions.

Table 3.8: Launch Vehicle Properties

Launch Vehicle	Dry Mass (kg)	Length (m)	Diameter (m)
Ariane 5	4540	6.77*	5.40
Delta IV 5-meter Stage	3490	13.7	5
Falcon 9	3900	13.7	3.66
Vulcan Centaur	3490	11.7	5.4

* 4.71 meters + 2.06 m payload adapter

The challenge was to create a rectangular set of shapes that could be turned into polygons. To achieve this, the model was first created using the available dimensions for the stage. Next, a series of squares were created with side lengths equal to the diameter of the circle as in Figure 3.30. A rectangular representation of a cylinder with width and height equal to the diameter of the cylinder has a similar surface area, and cross-sectional views normal to the center line of the two shapes are identical.

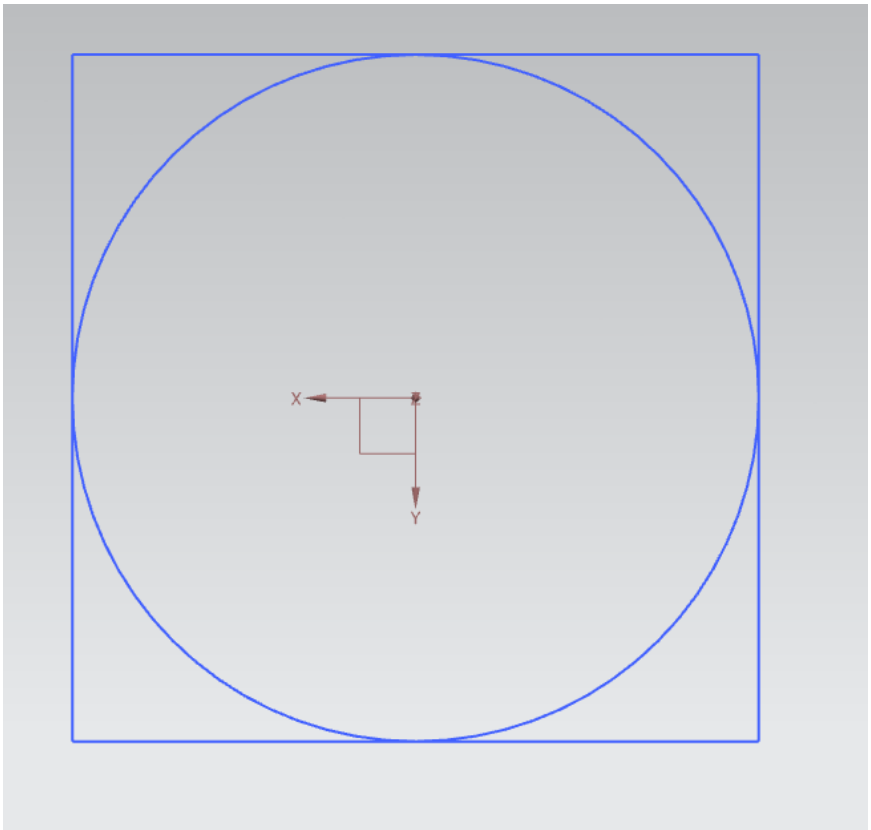

Figure 3.30: Creating Frame of Rocket Stages

The Ariane 5 has the highest perigee of the group, and is one of the worst violators of the 25-year guideline [85]. With a target perigee of 250 km, the likeliness that the stage will meet the 25-year guideline is almost zero [85]. Figure 3.31 shows the orbital lifetime evolution as a function of perigee altitude, which matches well with the model predication of 53 years for deorbiting the stage with no drag sail attached.

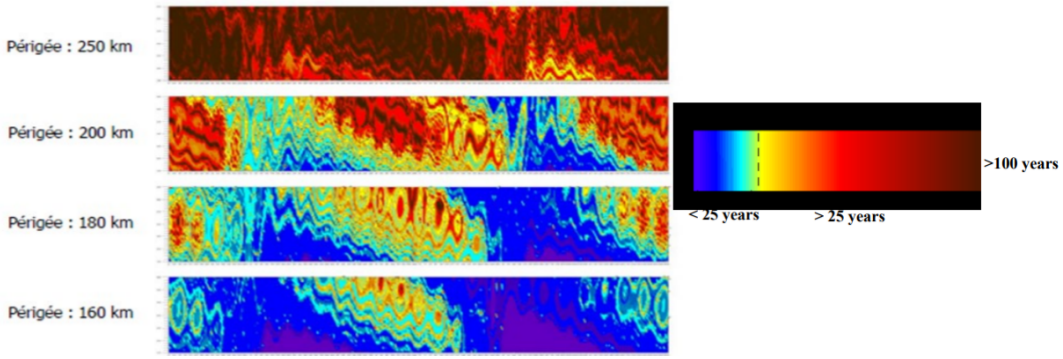

Figure 3.31: Orbital Lifetime vs Perigee Altitude

Each vehicle was then modeled for its target orbit without any drag modulation devices such as a drag sail. Its important to note that the target orbits used by the vehicles are ideal; it is much more common for the perigee to be higher as a higher perigee means that the payload requires less fuel to circularize its orbit. This means that the initial orbit that the drag sail is deployed into would be higher than the target orbits used in the analysis, leading to a longer mission duration for all of the sail sizes tested. The Delta IV launch records show some stages being left in 500+ km perigees while the target orbit is 235 km[85]. This means that the modeled deorbit time is very conservative and assumes the best case for stage decay.

The vehicles were also modeled with varying area drag sails attached. The areas selected range from 25 m^2 to 64 m^2. For the Ariane 5 target orbit, the results show that with no sail included the stage would take close to 54 years to deorbit.

Including a 25 m^2 sail, smaller than that used on the LightSail missions, reduces the orbital life to just over 40 years. Both the 64 m^2 and 49 m^2 sails provide the necessary performance for the decay rate to meet the IADC guideline, summarized in Table 3.9.

Another important consideration for drag sail performance is fault tolerance and how it impacts performance. The benefit of the stripped sail design is that if there is a puncture, only a small portion of the sail itself is affected. Even if a strip were to tear completely through, each strip is isolated from the others and therefore cannot propagate one tear to another strip. The weakest part of the sail in terms of mission failures are the booms. Since the drag sails are held in place, if one boom fails due to buckling or other method then the sail will effectively have half of its original area and the tension in the sail itself may be lost. Figure 3.32 shows one such failure. To analyze this failure mode, the 49 m^2 sail was modeled again but with a boom failure, causing half of the sail area to be lost. The simulation was then carried out again and compared with the initial results for deorbiting in Figure3.33.

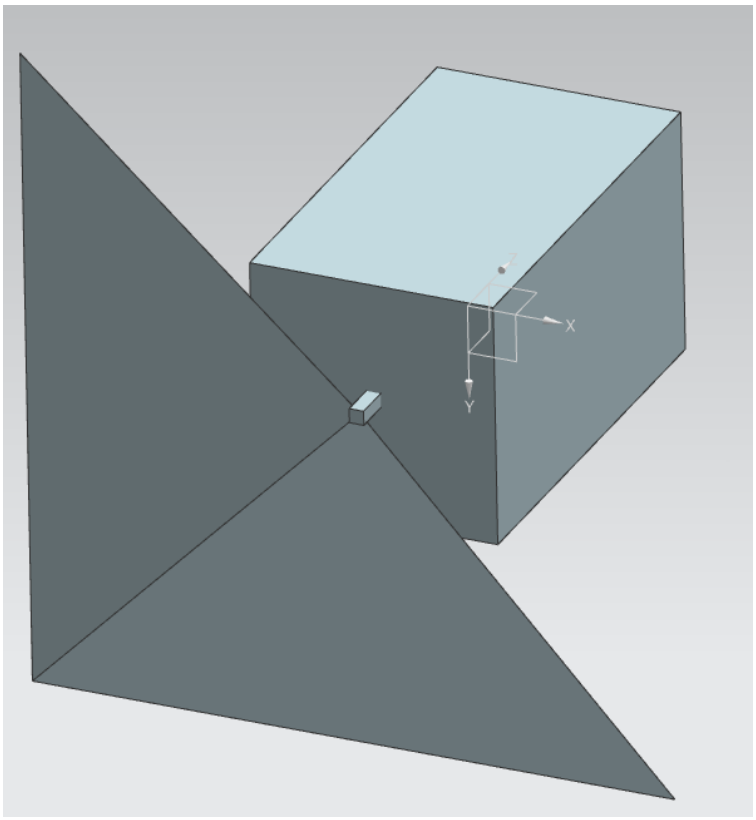

Figure 3.32: Damaged Sail Model

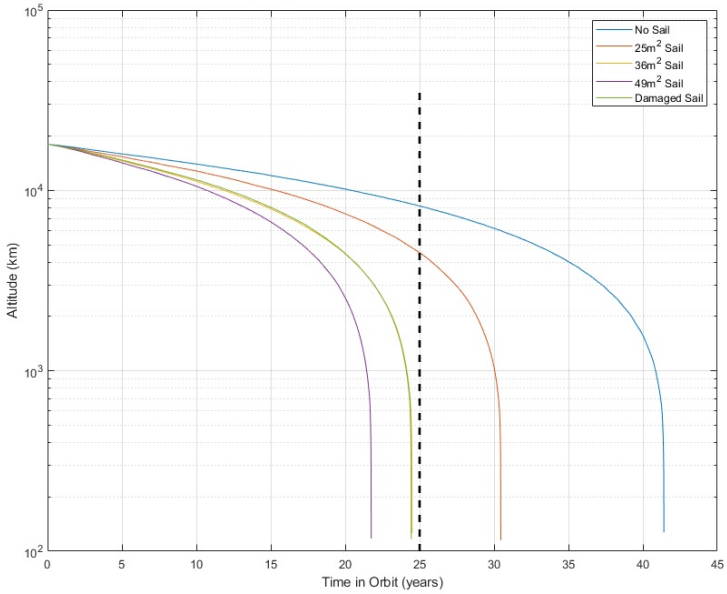

Figure 3.33: Example Sail Size Comparison

Results for the other launch vehicles were calculated and are summarized in Table 3.9. These values represent the most conservative estimate for decay for all of the missions, as stated earlier in this thesis. Even the 25 m^2 sail greatly reduces the amount of time that the objects are in orbit.

Table 3.9: Launch Vehicle Decays with Varying Drag Sail Sizes (Years)

Launch Vehicle	No Drag Sail	25 m^2	36 m^2	49 m^2	64 m^2
Ariane 5	53.86	40.25	36.29	18.28	18.13
Vulcan	26.48	12.63	11.02	9.64	8.59
Delta IV Heavy	63.02	41.25	36.17	31.51	27.55
Falcon 9	28.07	14.53	12.82	11.1	9.47
Est. Sail Mass(kg)	0.00	5.34	5.95	6.62	7.32

Notably the Delta IV Heavy remains in orbit the longest of any of the candidate launch vehicles. Even with the 49 m^2 sail, it takes approximately 31.5 years. Although this does not meet the IADC guideline, the sail the sail was able to reduce the amount of time on orbit by over 30 years. The Delta IV Heavy is also soon to be retired, in 2024, with only four more mission scheduled [86].

Another aspect of the simulation that was investigated was the impact of the solar cycle on the performance of the drag sails. Under increased solar activity, the atmosphere is expanded, which results in higher densities at the altitudes used in the simulation [55, 56]. Values for extremely high and extremely low solar activity were averaged from two atmospheric models and used in the simulation to understand how the solar cycle would impact the performance of a 49 m^2 drag sail. Figure 3.34 shows the expected decay of a rocket stage with extremely high, average, and extremely low solar activity. It is apparent that the solar activity levels have a large impact on the expected decay date. The change in solar activity is due to the solar cycle, which details the flipping of the Sun's magnetic poles approximately every 11 years [87].

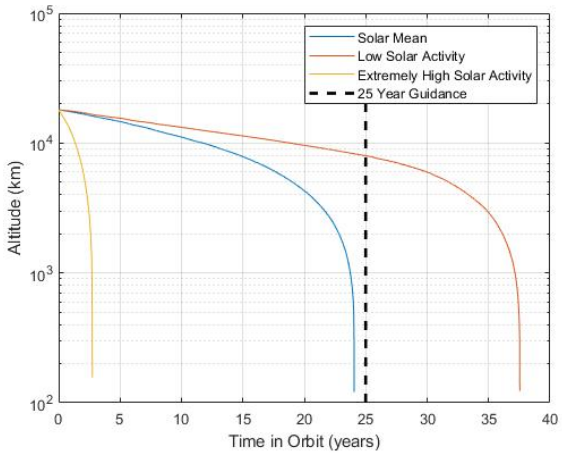

Figure 3.34: 49 m^2 Drag Sail Performance for Varying Solar Conditions

3.2.5 Attitude Analysis of Drag Sail Module Integration

The attitude of the sail-system is influenced by two determining factors. First is the placement of the drag sail, where asymmetry will result in differential torques throughout an orbit. The second is sail apex angle, which refers to the angle that the sail booms make with the center axis [24]. The two major design inputs for a drag sail are the sail boom length L and the apex half angle Φ, which are shown in Figure 3.35.

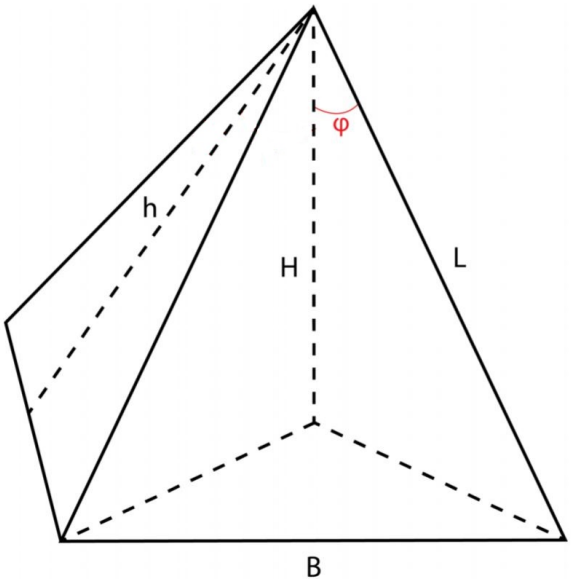

Figure 3.35: Drag Sail Geometry[24]

A smaller apex angle means that the sail is more swept, while a larger Φ angle results in a flatter sail. Students at the Georgia Institute of Technology researched the stability of deployable drag devices on small satellites, focusing on a 100 kg and 150 kg satellite that were each connected to a 95 m^2 drag sail and a 125 m^2 drag sail in an 87.9^o inclined orbit [24]. Apex angles were tested ranging from 65^o to 85^o, and the angle of attack of the sail was also varied. The right ascension of the ascending node was also varied to account for the different alignments with the sun vector, as the orientation influences the effect of SRP on the missions. The simulations were ran with both aluminized and non-aluminized sail materials. SRP was highly influenced by the orbit that the simulation was in, and only a few cases with aluminized sails were found to be stable, all of which were at or below 400 km [24]. With large highly reflective sail surfaces, the orientation of the Sun became an important input for determining stability. The students' simulation used an inclination of 87.9^o, which means that changes in the right ascension of the orbit in the simulation had a large impact on the sun-sail vector throughout the simulation. For an aluminized sail there were only a few cases that were found to be stable over the 5 orbit simulation, all of

which were below 400 km [24]. Instability was predicted by analyzing the derivatives of the rolling, pitching, and yawing moments with respect to the orientation of the spacecraft relative to the coordinate system defined in the paper [24]. The system described in the paper is largely influenced by SRP due to the large sail area to spacecraft ratio, consisting of a 95 m^2 and 125 m^2 highly reflective sail being integrated to a 150 kg spacecraft [24]. This was compounded by the fact that the simulation was conducted for 5 orbits, which is only about 530 minutes in duration. During this time the direction of the sun relative to the orbit is not going to change significantly as perturbations have not significantly affected it, which means that any resultant torques are highly dependent on the initial conditions. This thesis will be propagating the simulation for several decades, so the orientation of the sun with respect to the spacecraft is expected to change significantly. The sail area to spacecraft ratio is also much smaller, as the sails being considered range from 25 m^2 to 49 m^2 and the masses range from 3490 kg to 4540 kg. The research on Apex angle can however, was adopted and implemented directly into this thesis. The investigation of the sail apex angle and its impact on attitude and stability is important because aerostability was shown above to contribute to a shorter disposal period for the same sized drag sail when compared to a tumbling case in the Notable Demonstration Missions section.

Based on the recommendation from the student at Georgia Tech, and apex angle of 85^o was used for the models in this thesis [24]. This apex angle was the only angle used due to the large number of other inputs to the model which were considered, thus an investigation of how varying the apex angle affects the dynamics in a GTO was not carried out in this thesis. Analysis on the variation of the apex angle and its impact on sail performance can be implemented in this model simply by creating the initial CAD model with the desired sail angle. The model will interpret the sail angle when it creates the vertices it uses for the calculations. The attitude of the missions was propagated in order to determine the projected areas for the various

perturbational calculations for the simulation, but stability analysis was not conducted directly. It is difficult to analyze global stability of this nonlinear system with time-dependent forces which rely on all of the initial conditions. One method would be to linearize the system at various points of the orbit and determine whether or not the system is locally stable, but just because a *linearized* dynamical system is stable does not mean that the true nonlinear system is globally stable. This type of analysis was proven to be nontrivial, as at each instance for each candidate vehicle the time-dependent forces are also dependent aspects of the spacecraft itself such as the orbital position, attitude, and attitude rates. Another method for determining stability of the nonlinear system would be using Lyapunov's direct method, which uses a continuous unbounded positive definite function for assessing global stability of nonlinear systems. Stability was not assessed in this thesis, but the resulting attitude dynamics from the simulation can still be analyzed to see if they match the expected results.

For large drag sails using aluminized materials, the students at Georgia Tech concluded that only a few of the orbits they simulated would be stable [24]. This was due to the effects of solar radiation pressure on the large sail area causing the attitude to grow and become unstable in the selected orbits. The students also presented a baseline design of a sail with an apex angle of 85 ^{o} with 8 m booms that would be capable of deorbiting a 100 kg satellite from a 1200 km polar orbit within 25 years. The parameters of the orbits assessed by the students at Georgia Tech are different from those that would be experienced by a rocket stage in a typical GTO, mainly the physical parameters such as mass and sail area to spacecraft ratio as well as the orbital parameters such as the inclination and altitude. A typical GTO will only be within the regime described by the students for less than 25% of its orbit, which indicates that the conclusions about sail stability may not carry over. The simulations were also only carried out for 5 orbits, which is not indicative of long-term orbital

stability. The students concluded that non-aluminized sail materials performed better with regards to stable configurations, but did not mention the effects of long term environmental effects such as atomic oxygen, which leaves additional questions about the material selection and recommendation. It was determined from Table 2.2 that aluminized sail materials withstand the effects of atomic oxygen better than their non-coated counterparts [33].

When the sail-equipped rocket stage is within this region, is it expected that the spacecraft will experience a restoring torque due to the drag on the sail which will attempt to align the sail with the velocity vector. However, since the spacecraft is only within this region for a small portion of its overall orbit, this restoring torque cannot be relied on for aerostability. Due to the asymmetric placement of the sail itself on the rocket, it is also expected that the system will experience a screwing motion as the differential torques on the sail and the spacecraft itself cause it to rotate. If the angular velocities are low after the region of aerostability is passed, the spacecraft will return to rotating about its major axis. If the angular velocity about the sail-centered axis are high, though, it may continue to spin about that axis until its next perigee encounter. It is more desirable for the system to rotate about its major axis, as rotation about the sail axis would result in an undesirable entry attitude at its next perigee encounter. Figure 3.36 shows how the system would enter the aerostabilized region if spin stabilized about its sail axis from the previous pass. The system leaving perigee after being stabilized and aligning the sail with the velocity vector(left), and the system arriving to the aerostabilizing region with the same attitude it had after leaving on the previous orbit (right).

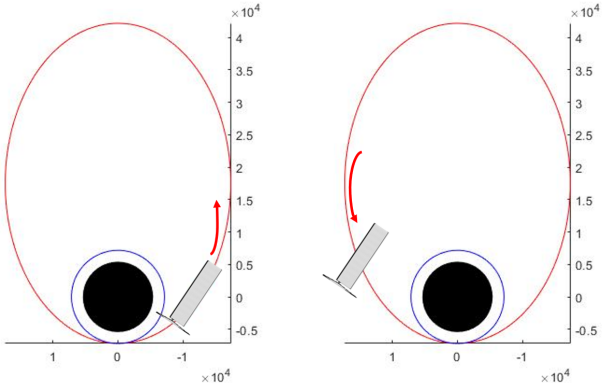

Figure 3.36: Sail Alignment if Center Line Rotation

Placement of the drag sail on the launch vehicle is also an important assumption which has large impacts on attitude evolution. The ESPA ring interface was chosen for the placement of the drag sail for the analysis. The ESPA ring was designed as a structural interface to the EELV bolt patterns, which allows it to interface with the ATLAS V, Falcon 9, Delta IV, Vulcan, and New Glenn launch vehicles [47, 88]. The ability to be integrated with active and future launch vehicles makes the ESPA ring an ideal candidate for the initial analysis for this thesis. Additionally, if directly integrating the module with the payload-to-rocket adapter if favored, the analysis conducted in this thesis will not require major changes. Figure 3.37 shows the alignment of the sail for a center line mounting configuration and an ESPA ring mounted configuration.

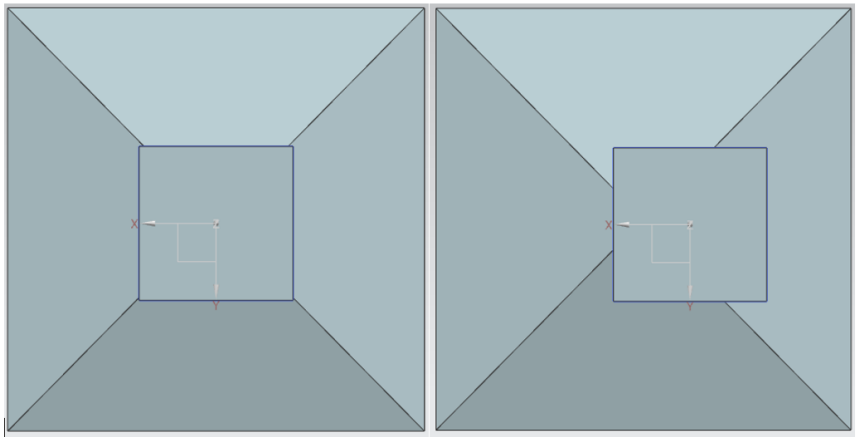

Figure 3.37: Drag Sail Location, Axial (left) vs ESPA (right)

With the asymmetric placement of the drag sail, it is expected that the spacecraft will experience a corkscrewing motion which will result in dominant angular velocities about two axes. With the center of mass being assumed at the geometric center, there is an asymmetric torque applied to the vehicle, which causes the pitch to increase. A breakdown of how this occurs is shown in Figures 3.38 and 3.39. In Figure 3.38 there is an asymmetric drag force due to the exposed area of the sail on the -Z face of the spacecraft. This causes the spacecraft to rotate such that the sail would rotate into the page and the +Z face would rotate out of the page.

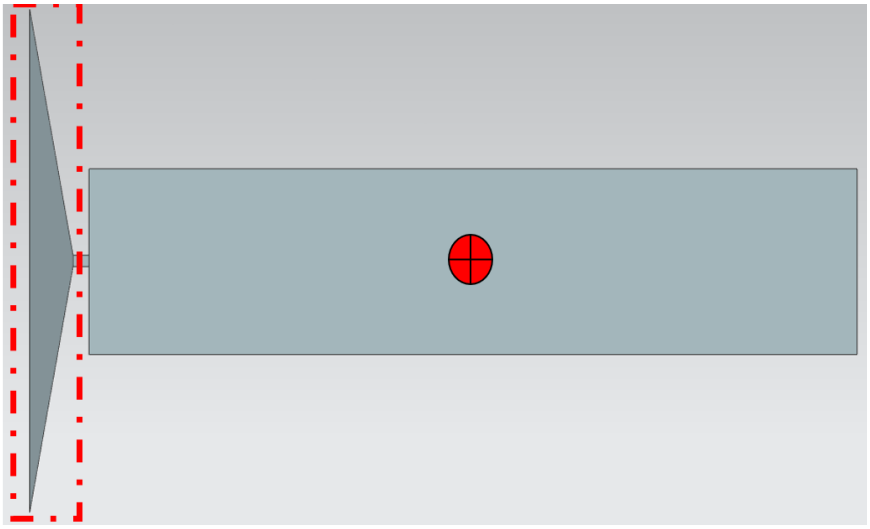

Figure 3.38: Center of Mass Asymmetry, $+X_{Body}$ View

Once rotation has begun, the asymmetry of the sail placement on the launch vehicle also creates a differential torque which is shown in Figure 3.39. As the spacecraft rotates, this asymmetry would cause rotation about the X axis. The combination of rotations occurring at the same time leads to the conclusion that the spacecraft is expected to have a rotation about multiple axes, most likely the Z-axis and X-axis.

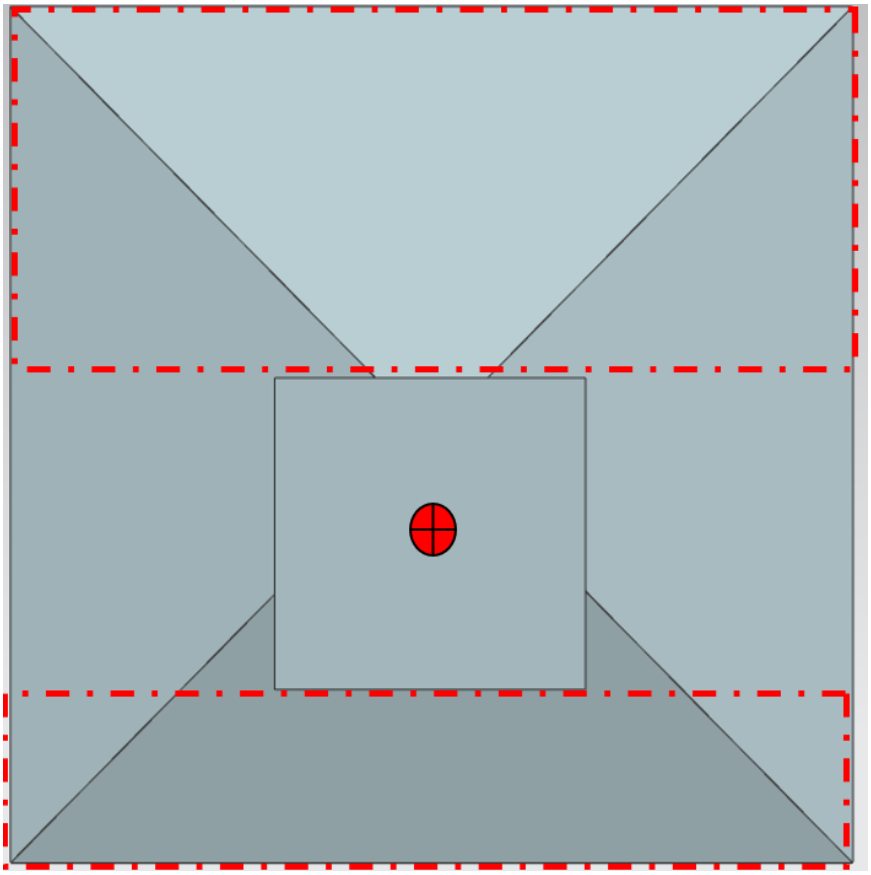

Figure 3.39: Center Of Mass Asymmetry, $+\mathbf{Z}_{Body}$ View

The spacecraft was given an initial displacement of 90^o with respect to the Y-axis so that the Z-axis of the rocket is aligned with the X-axis of the Local Vertical, Local Horizontal (LVLH) reference frame, shown in Figure 3.40. The LVLH frame in this regard is created such that the Z-axis points towards nadir, the Y-axis is negatively aligned with the angular momentum of the orbit, and the X-axis completes the right-hand rule.

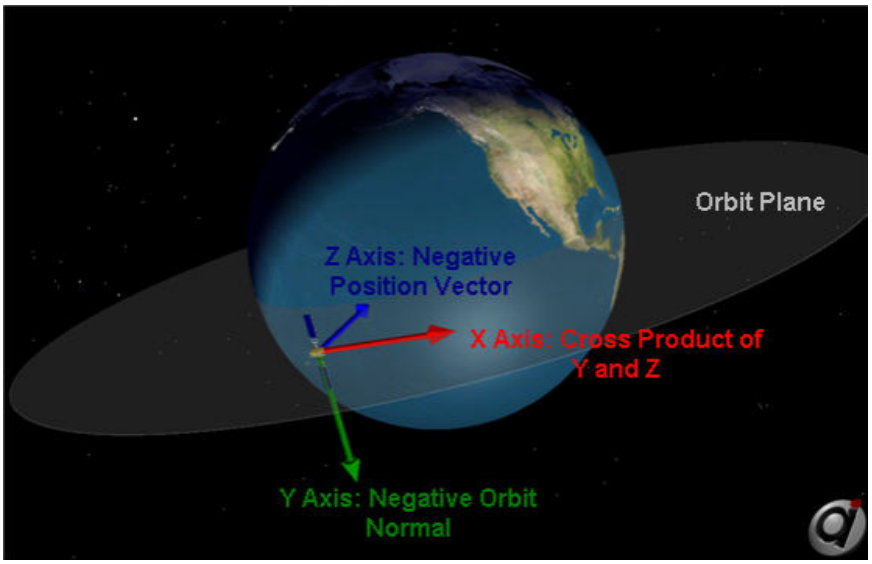

Figure 3.40: Local Vertical Local Horizontal Reference Frame [89]

The initial attitude of the sail-rocket system was chosen to simulate the sail being deployed once the payload has been deployed and the rocket body translated away from it. Figure 3.41 shows the initial orientation of the spacecraft with respect to the LVLH frame, which represents the Delta IV Centaur target orbit with an inclination of 27^o. The sail system mass was assumed to be 7.0 kg based on the mass estimate in Table 3.2, which was uniformly distributed to the sail module in the CAD model. The sail was then added to the launch vehicle model and the inertia was recalculated to be used in the analysis.

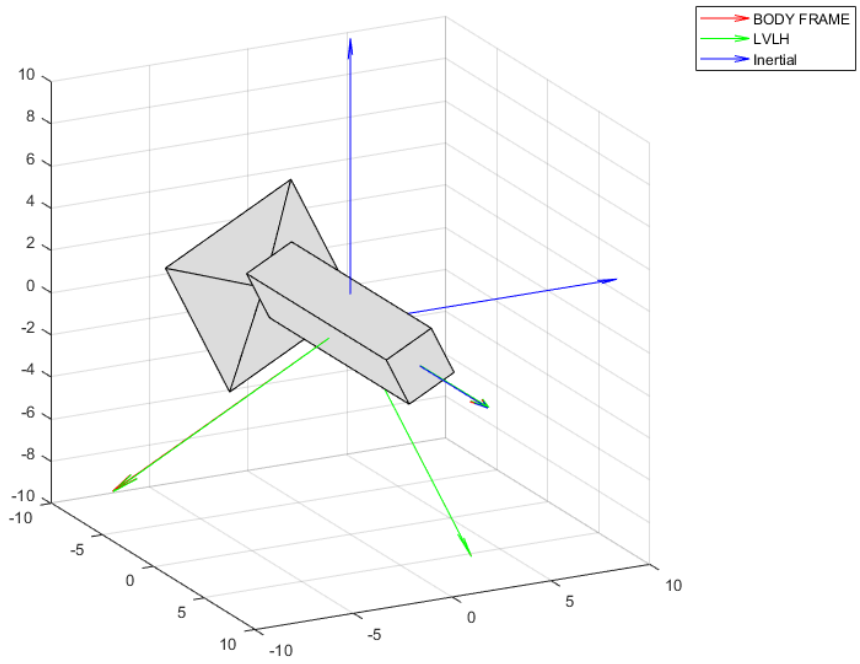

Figure 3.41: Initial Attitude of Delta IV Centaur

The attitude and attitude rates were investigated over several orbits with the drag module placed at the center line of the launch vehicle as well as at the radius of the ESPA ring. Figure 3.42 shows the first 5 orbits simulated. Starting at apogee, each perigee location and thus region of aerodynamic loading occurs at 0.5 orbits, 1.5 orbits, and so on. Although the angular velocities are low in magnitude, a spike can be seen at every perigee encounter, each followed by a new set of oscillations in the X and Y axes and a new angular velocity in the Z-axis.

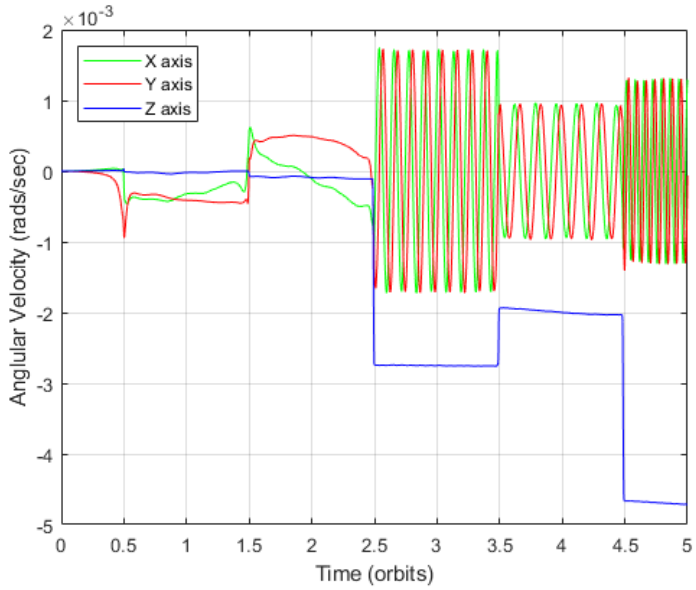

Figure 3.42: Ariane Center Line Sail Attitude Rates for 5 Orbits

At each perigee encounter, the attitude of the vehicle oscillates as expected. This is due to the aerodynamic torque of the sail acting as a restoring torque on the vehicle. The scale of the plots may make it appear the vehicle is sporadic, but X-axis of the figure is in orbits, greatly compressing the dynamics. The overall angular displacements were plotted as well and are shown in Figure 3.43, which shows that the Z-axis is indeed the primary axis of rotation as it has the largest angular displacement. Both the pitch and yaw axes oscillate, although dwarfed by the Z axis displacement, which matches the analysis found by the students at Georgia Tech [24].

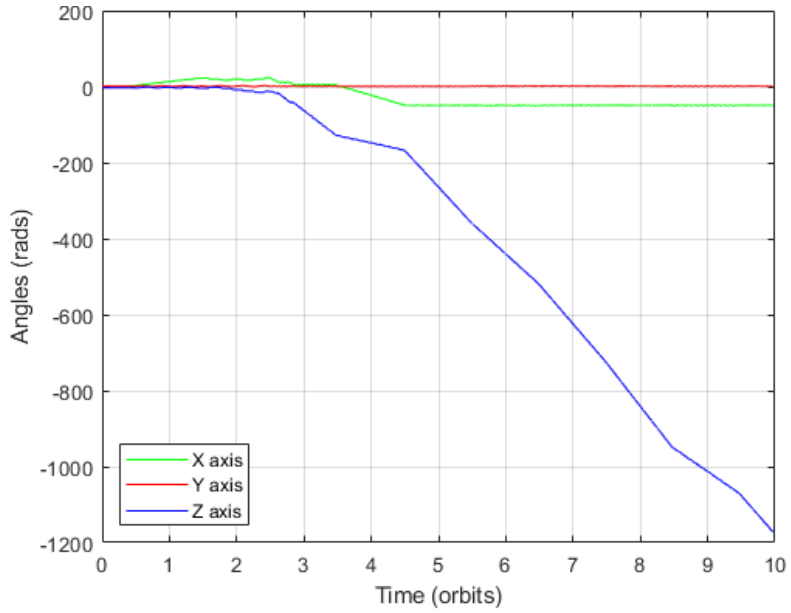

Figure 3.43: Ariane Center Line Sail Attitude for 10 Orbits, All Angles

The simulation was then run again with the ESPA ring configuration to see how the asymmetric alignment of the drag sail impacted the attitude over the orbit. Figure 3.44 shows that for 5 orbits there is a difference response in for the overall angular velocities. The Z-axis is no longer dominating in terms of magnitude, and more oscillations occur close to perigee as the drag torque is distributed. These oscillations represent the restoring torque of the drag sail causing the spacecraft to wobble, until around 0.65 orbits where the vehicle has left the aerostabilized region and the atmospheric density has dropped low enough to have a negligible effect on the spacecraft's dynamics.

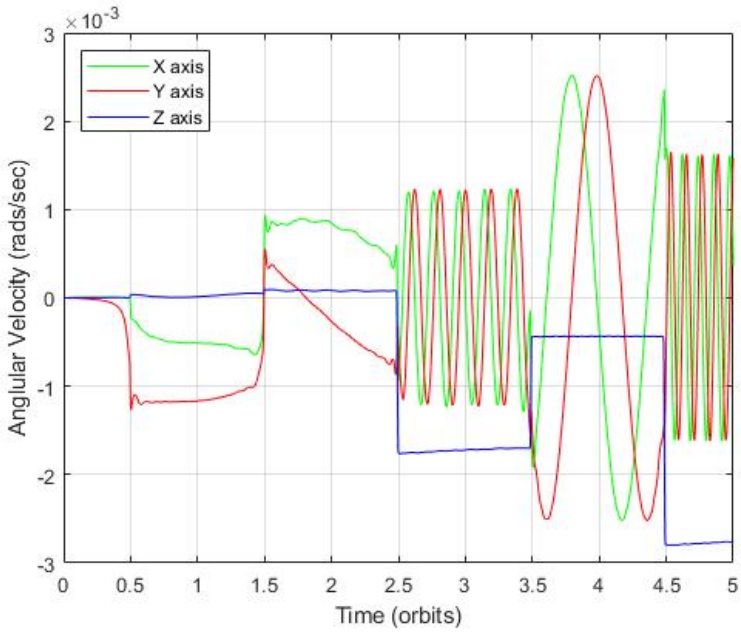

Figure 3.44: Ariane ESPA Mounted Sail Attitude Rates, 5 Orbits

By the time the satellite has reached 0.60 orbits and 1.60 orbits, or 36^o of true anomaly, the restoring torque has diminished. The diminished torque is due to the fact that the spacecraft has already passed 830 km in altitude at that time. Figure 3.45 shows a close up of the first perigee encounter, where the oscillations due to the restoring torque of the vehicle can be more clearly seen. These oscillations diminish around 0.65 orbits, which coincides with the spacecraft passing 850 km in altitude. This sort of restoring oscillation occurs near perigee for every orbit, and coincides with the conclusions of the Georgia Tech students discussed altitudes where areostability can be seen as a reliable method of attitude control [24].

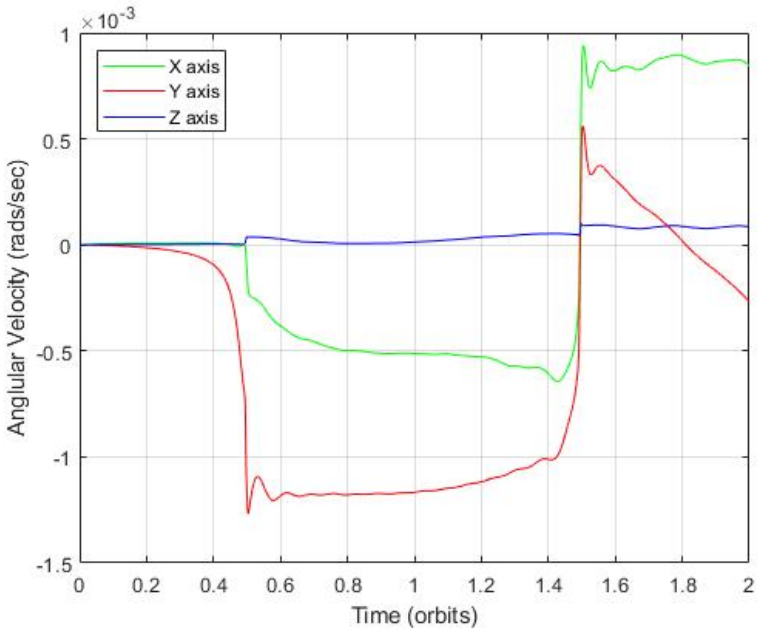

Figure 3.45: ESPA Mounted First Perigee Attitude Rates

The orbit was further propagated for a total of 50 orbits, with the angular rates shown in Figure 3.46 and the angular displacements shown in Figure 3.47. The angular rates appear to follow a cyclical pattern, not diverging as the spacecraft continues to gain and lose aerodynamics torques. Figure 3.47 shows that the spacecraft is spinning primarily around the X and Z axes, where X is the major axis and Z represents the minor axis where the sail is aligned. If there was no sail included, the vehicle would be expected to rotate about its major axis. Instead, the dynamics are as described above, where the apparent screwing motion results in spin about two axes. The Z-axis experiences the highest angular velocities, approximately $0.64 \frac{degrees}{sec}$.

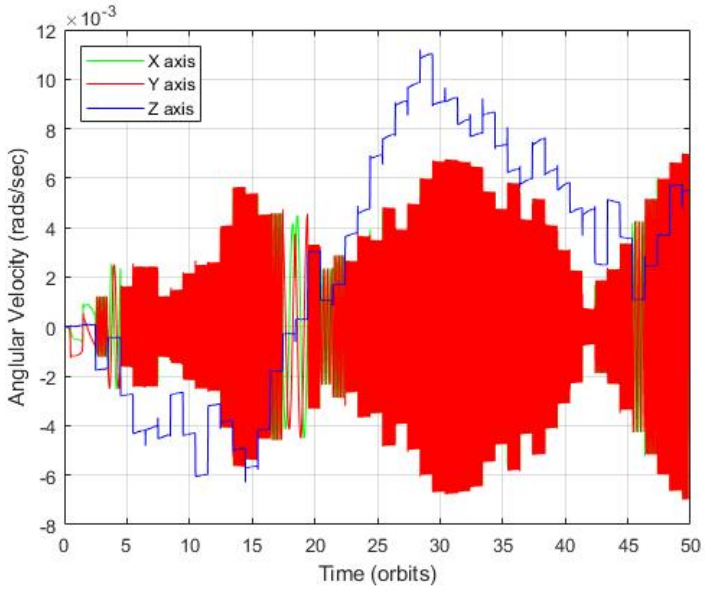

Figure 3.46: Ariane ESPA Mounted Sail Attitude Rates, 50 Orbits

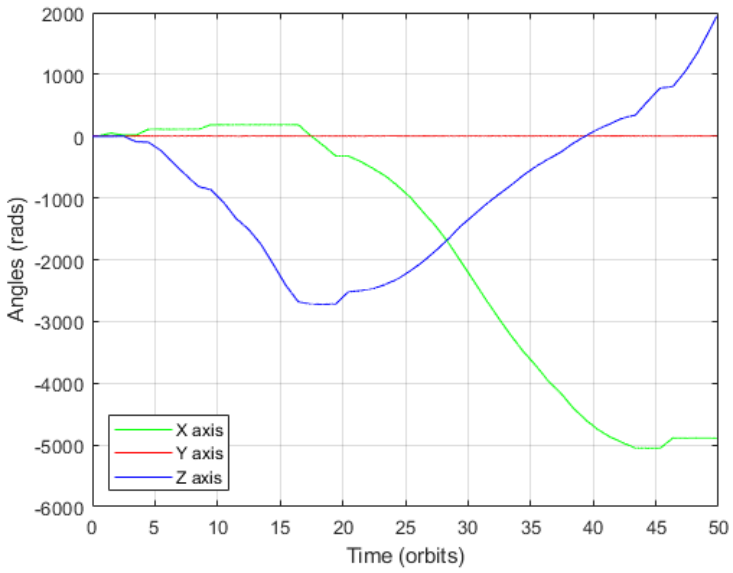

Figure 3.47: ESPA Mounted Sail Angular Displacement, 50 Orbits

Figures 3.47 and 3.43 show how the placement of the sail impact the dynamics of the system. As expected, the asymmetric placement of the sail on the ESPA ring radius resulting in rotation about two axes resulting in a screwing motion, while the center line case experienced rotation primarily about the Z-axis only.

The same analysis was carried out on the Delta IV's Centaur upper stage to compare results. The results are expected to be different as the dimensions and mass properties of the vehicles are different. The Delta IV Centaur represents the longest launch vehicle considered, while the Ariane is the shortest. The simulation results should lead to a better understanding of how the length of the vehicle impacts their dynamics.

The Delta IV's Z-axis experiences larger rotations in magnitude, which can be attributed to the increased inertia of the major axis as the stage is significantly longer. The magnitude of the X and Y axis of the body are approximately equivalent to the Arianes' angular velocity, with magnitudes around 0.006 $\frac{rad}{sec}$ or 0.34 $\frac{degrees}{sec}$. The Z-axis reached a maximum angular velocity of 3.6 $\frac{degrees}{sec}$ during the 50 orbit simulation shown in Figure 3.48. The apparent discontinuities in the figure are due to the scaling of the X-axis, which has units of orbits. The angular displacements shown in Figure 3.49 show that the rotation is primarily about the Z-axis alone, which was only the case for the Ariane when the sail was aligned axially.

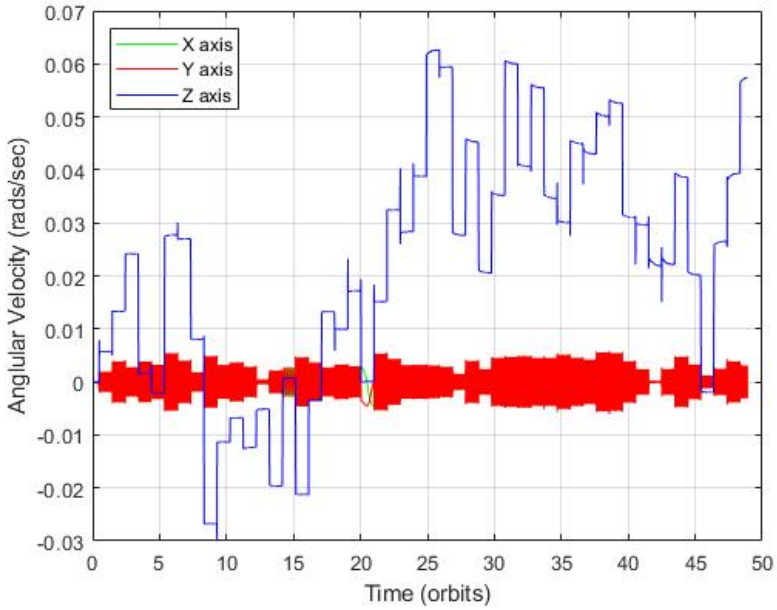

Figure 3.48: Delta IV ESPA Mounted Sail Attitude Rates, 50 Orbits

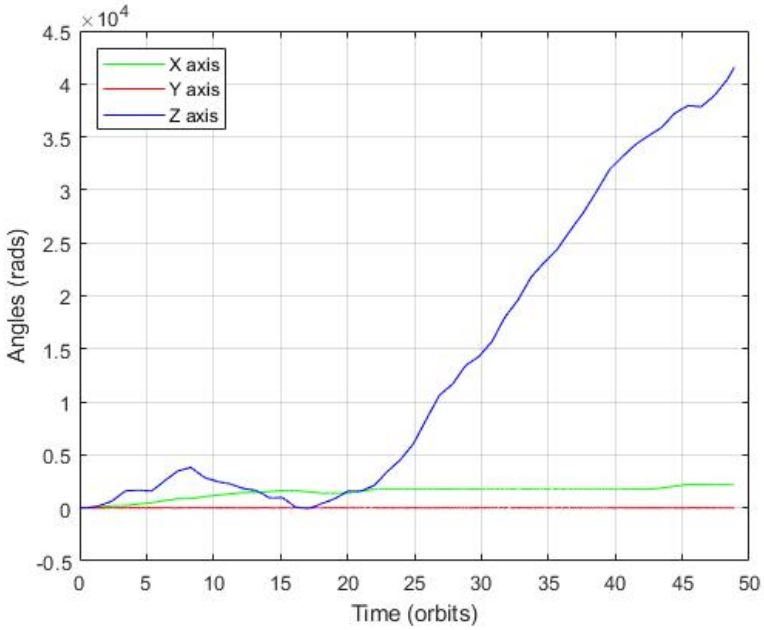

Figure 3.49: Delta IV ESPA Sail Angular Displacement, 50 Orbits

There are unique challenges when designing for passive stability in Geostationary Transfer Orbits. Varying the apex angle of drag sails in LEO applications has shown that passive global stability can be achieved for some configurations, but does not

transfer directly to GTO missions [24]. Due to the shape and varying altitude of GTOs, only a relatively small portion of the orbit is within the region where aerostability may occur. In this thesis, a 49 m^2 drag sail was positioned asymmetrically at the radius of an ESPA ring to determine how the placement of the sail would affect the dynamics of the system, and if the system would become aerostabilized at any point in its orbit. The resulting dynamics showed that the sail's placement did have an impact on the rotational dynamics of the system, causing rotation to occur around multiple axes. Below 800 km, there was evidence of a restoring torque being applied to the system, as the spacecraft experienced asymmetric torques which caused it to rotate. Once the spacecraft had passed 850 km, this torque became negligible, allowing the spacecraft's momentum to carry it as it headed towards apogee. The regime where the sail is capable of aerostabilizing was determined to be less than 20% of its entire orbit, leaving doubts about passive global stability.

The omission of perturbations which rotate the orbital plane were also called to question. The orbit will not rotate significantly after a few orbits, but over several years of propagation it is expected to have experienced several rotations. This is important to note with regards to the attitude dynamics because an inertially placed spacecraft will have a different orientation with respect to perigee as the ascending node of the orbit is moved and thus the perigee location, especially for inclined orbits. For this thesis, it is sufficient to include only SRP, drag, and GG as those torques affect the orbits apogee and perigee directly. Over several years, the rotation of the orbital plane is expected to make several full rotations, which was why the perturbations which would account for orbital rotation were not included at the cost of computational speed. Local and global stability throughout the simulation were not assessed in this thesis, but would require that these perturbations be included as they will affect the attitude dynamics over several years.

Once the drag sail has reduced the orbital altitude from a highly eccentric GTO to a LEO, the attitude can be studied to determine if the vehicle will become stabilized. For an orbit that is 250 km x 350 km, 10 orbits are again simulated with an angular offset of 90^o in the Y-axis. This means the sail center line is initially parallel to the atmospheric velocity vector. There is again an oscillatory motion which indicates that the vehicle is spinning about multiple axes, shown in Figure 3.50. For the LEO case, the spacecraft again rotates about two axes, similar to the ESPA mounted sail in Figure 3.47.

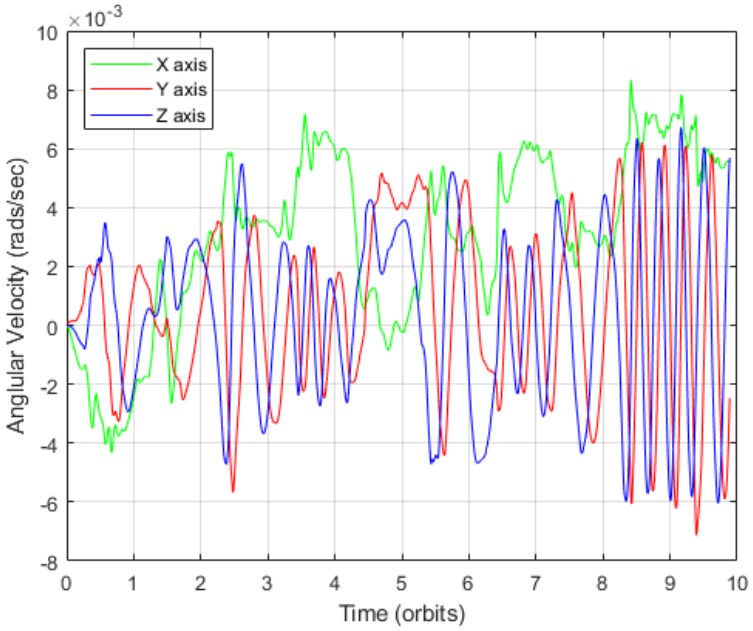

Figure 3.50: LEO Attitude Rates

For both the LEO and GTO simulations, the sail systems experiences rotation about multiple axes when the sail was integrated asymmetrically. The reason for the rotation was discussed and it was compared with a center line mounted sail. The results showed that the placement of the sail on the rocket stage did have and impact on the resulting dynamics, causing the rotation of the vehicle to be about two axes rather than being dominated by axis that the sail was mounted to. It was

also determined that the sail system does experience some level of aerostability near perigee, similar to the findings of the students at Georgia Tech that were looking at stability of large sail systems. However, the target GTOs that were looked at are only within this region for less than 25% of their orbits, raising doubts about the possibility of passive global stability. The dynamics of the sail system were modeled for several launch vehicles and initial conditions, but stability was not determined in this thesis. To assess stability, linearization of the system would need to be carried out at specific instances, and even then that would only show local stability. With time-dependent forces which also depend on all of the initial conditions, this task would not be trivial as each set of initial conditions would lead to different results. The target orbits that were chosen for this mission represent a general mission for assessing the performance of the drag sail on the targeted launch vehicles, but many missions have unique requirements and perigees that may differ from the selected orbits which will affect the forces that will influence and change the systems attitude.

Chapter 4

CONCLUSIONS AND FUTURE WORK

This thesis set out to assess the current progression of small satellite drag sail technologies and to determine if there were any limitations which would prohibit the integration of the drag sail onto a launch vehicle in a Geostationary Transfer Orbit. The analysis was broken into sections which would determine performance capabilities and limitations of current drag sail designs. The chosen design would then be integrated with several candidate launch vehicles in target GTOs in order to simulate how the inclusion of the sail would impact orbital longevity. A baseline 49 m^2 drag sail was capable of assisting a majority of the active launch vehicles considered to meet the 25-year guideline set by the IADC. A 64 m^2 drag sail was also determined to be feasible, but unnecessary for deorbiting the vehicles within the allotted time.

Sail material limitations were determined based on testing data as well as research. The space environment for a GTO is different than LEO, with unique considerations with regards to structural loading, radiation, atomic oxygen and stability. A model was created to assess the limitations on drag sail scalability for GTO applications, and analysis was conducted for each of the candidate launch vehicles. The selected material for the design was 12.5 µm Upilex-125S. The material was chosen over other materials such as Kapton, CP-1, and Mylar due to its high thermal performance as well as its ductility. The sail design chosen was a stripped sail with semi-rigid booms. This design was chosen over alternatives such as the heliogyro and 5-point quadrant sail with stitching because of the reduced requirements it imposes on the host vehicle, lower loading on the boooms, and increased resilience to the space environment. The stripped sail design in particular is important because stripping allows for traditional

stitching to be removed and reduces some structural mass requirements from the booms. It was determined through testing at Cal Poly SLO that the stitching used on LightSail-2 was susceptible to atomic oxygen, and could fail as early as 70 days into a mission in LEO. Stitching is typically included to reinforce the sail membrane to ensure the sail would not be completely lost if a tear were to initiate. The stripping of the sail replicates this effect... if one strip were to fail and a tear was initiated, the other strips would remain unaffected.

Loading on the drag sail was investigated to find whether or not critical loading would occur for a given sail area. NASA ORDEM software was used to estimate a maximum diameter impact for the drag sail over a 25-year mission, and that value was used to calculate what the maximum allowable tension in the sail could be before tearing would be a concern. For the 49 m^2 baseline, the maximum impact diameter was estimated to be 3.76 mm. For the single attachment point, the required tension for this impact to initiate a tear was approximately 1100 mN. For the dual attachment point setup, the loading required to initiate a tear is approximately 3 N. It was shown through analysis that the maximum tension expected in any sail strip would 190 mN, which is much less than the conservative single attachment design. Loading on the booms followed suite, and it was determined that the maximum expected moment at the boom hub would be 1.6 N-meters. Research showed a boom design that was optimized for a stripped sails that was baseline tested to withstand 45.4 N-meters in its weakest axis before failing.

The mass of a 49 m^2 sail was also baselined using information from online resources as well as the research on boom optimization for stripped sails. It was determined that a CubeSat dispenser-like system would have a mass budget of 6.62 kg, which is less than the mass of a full mk.III PPOD.

Once sail sizing had been analyzed, a model was created to understand how the system would perform in orbit. The model was based on a polygonal tool created

for analyzing CubeSat ADCS systems, and calculated the torques for the spacecraft using a series of projected polygons. The model was propagated using a developed implementation of Encke's Method. Concerns about stability were issued, as well as concerns about the inclusion of certain perturbations for long term orbital propagation and their effect on the spacecraft's attitude. It was determined that the ESPA mounting structure offered several opportunities for the sail to be interfaced, so it was selected to be used in the model. The model showed that for each of the launch vehicles chosen, they would fail to meet the IADC guideline if no changes were made. The model also showed that the inclusion of even a 25 m^2 drag sail greatly reduced the vehicle's orbital life. The 49 m^2 sail was capable of deorbiting the stages within the allotted 25-year guideline.

Kessler Syndrome can become a reality. If work is not done to reduce the amount of defunct artificial satellites being left in orbit than the opportunity to go to space may be taken away. This thesis presented one possible path forward for spacecraft to be passively deorbited once their operational phase has concluded, which would help with reducing the amount of space debris created.

4.0.1 Future Work

First, additional perturbational impacts on long term attitude stability should be investigated and compared with the results of this thesis. The model's orbital performance was specifically verified using selected candidate missions, but no direct verification was performed on the attitude dynamics of the system. Comparison with an industry standard program such as STK or GMAT should allow verification of the developed model. Investigation into the assumptions for spacecraft properties should also be investigated as model fidelity and the number of polygons that are used for the simulations may have a large impact on accuracy and reliability of results.

The model's use cases should also be expanded. This thesis aimed to understand the performance implications of the inclusion of a drag sail on spacecraft in transfer orbits. There is a lot of literature discussing the ideas of high LEO spacecraft using drag sails as a means of deorbiting, but a simulation of such an orbit was not carried out under this thesis. High LEO applications may prove another path forward for this concept, adding to the list of vehicles that can benefit from this design and aid with the reduction of orbital debris in the future.

Currently, high LEO objects make up a majority of the mass in orbit around Earth, shown in Figure 2.10 [90]. The 500 km to 1100 km range is an ideal candidate for analysis of drag sail performance, as the altitude is low enough that drag sails may prove useful in the disposal of space vehicles and rocket bodies. Without any means of deorbiting, these satellites are left to naturally decay in their orbit over decades or even centuries. With the help of a drag sail, perhaps these missions can have their decay rates increased and their orbital lives shortened.

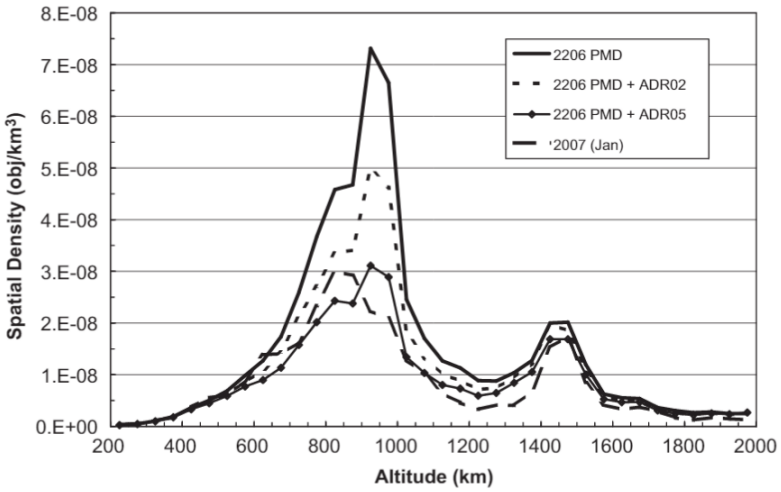

Figure 4.1: LEO Spatial Density [90]

Preliminary CAD and design work should also be started using the analysis performed in this thesis as a framework. Materials recommended in this thesis should be procured and subjected to long-term environmental testing if possible. With an

expected mission duration of 20+ years, the materials used will need to undergo significant long term testing. Long term testing may show whether or not the material is able to survive the cyclical fatigue associated with being placed in a GTO as well as show if any sort of flaking or material degredation may occur during the mission phase of the system.

Earlier it was assessed that a single boom failure on a 49 m^2 sail would still allow the system to meet the 25-year IADC guideline, but analysis was not conducted to understand how the loading in the other booms would be impacted by the failure. Since multiple strips are tensioned by each boom, the failure of a strip or boom could result in potential shear loads developing in the other booms. When assessing booms for future design cases, it should be considered how the boom would deal with additional shear load due to the loss of a strip or boom and how that would impact the tension on the adjacent strips.

Lastly, impact probability and risk assessment should be investigated. The rationale for ignoring this research was that the vehicles currently in orbit act as the drag sail system would. Risk assessment should be performed, as the inclusion of a drag sail may result in more uncertainty in the mission profile as well as increased risk of conjunctions occurring with other vehicles. Particularly MEO, where the GPS satellites are located, may include additional restrictions that would inhibit the use of a drag sail in a GTO. Risk of harm to humans should also be researched further. As a drag sail lowers the energy of an orbit, the angle at which it reenters the atmosphere becomes shallower. A shallower impact angle results in a larger lobe of uncertainty where debris may fall. This will need to be assessed to determine if passive orbit decay through the use of a drag sail would endanger people on the ground.

BIBLIOGRAPHY

[1] U.S. Department of State Archive, *The Launch of Sputnik, 1957*, Jan 2001. Available: https://2001-2009.state.gov/r/pa/ho/time/lw/103729.htm

[2] Orbital Debris Program Office, *Orbital Debris Program Office, LEGEND Evolutionary Model*, 2021. Available: https://orbitaldebris.jsc.nasa.gov/modeling/legend.html

[3] Brian Weeden, *2009 Iridium-cosmos Collision Factsheet*, 2010 Available: https://swfound.org/media/6575/ swf_iridium_cosmos_collision_fact_sheet_updated_2012.pdf

[4] Rafi Latzter, *Two satellites might collide at 32,000 mph over the Arctic today*, 2021 Available: https://www.livescience.com/satellite-collision-siberian-arctic.html

[5] Louis de Gouyon Matignon, *THE KESSLER SYNDROME*, 2019 Available: https://www.spacelegalissues.com/space-law-the-kessler-syndrome/

[6] IADC Steering Group and Working Group 4, *IADC Space Debris Mitigation Guidelines*, 2020 Available: https://orbitaldebris.jsc.nasa.gov/library/iadc-space-debris-guidelines-revision-2.pdf

[7] United Nations, *Space Debris Mitigation Guidelines of the Committee on the Peaceful Uses of Outer Space*, 2010 Available: https://www.unoosa.org/res/ oosadoc/data/documents/2010/stspace/stspace49_0_html/st_space_49E.pdf/

[8] NASA, *Where Do Old Satellites Go When They Die?*, 2019 Available: https://spaceplace.nasa.gov/spacecraft-graveyard/en/

[9] Westport, *What is Boil-off?*, 2011 Available: https://unece.org/DAM/trans/doc/2011/wp29grpe/LNG_TF-02-05e.pdf

[10] publisher, *LightSail-1 Solar Sail Design and Qualification*, 2012 Available: https://esmats.eu/amspapers/pastpapers/pdfs/2012/biddy.pdf

[11] J. Hiemstra, *Mechanical Design and Development of a Modular Drag Sail for the CanX-7 Nanosatellite Mission*, 2014 Available: https://www.semanticscholar.org/paper/Mechanical-Design-and-Development-of-a-Modular-Drag-Hiemstra/20a174472f38fc6012289149d26c814e0c40881c

[12] CubeSat.org, *CubeSat.org*, 1999 Available: cubesat.org

[13] nanosats.eu, *Total nonosatellites and CubeSats launced*, 2021 Available: https://en.wikipedia.org/wiki/CubeSat#/media/File:Total-CubeSats-Launched.png

[14] Cornell, *Chapter 4, Possible Operational Orbits* Available: http://hosting.astro.cornell.edu/~berthoud/alpsat/chapter4a.html

[15] NASA JPL, *NASA and Smallsat Cost Estimation Overview and Model Tools*, 2020 Available: https://www.nasa.gov/sites/default/files/atoms/files/saing_nasa_and_smallsat_cost_estimation_overview_and_model_tools_s3vi_webinar_series_10_jun_2020.pdf

[16] ScienceDirect, *CubeSat evolution: Analyzing CubeSat capabilities for conducting science missions*, 2017 Available: https://www-sciencedirect-com.ezproxy.lib.calpoly.edu/science/article/pii/S0376042116300951?via%3Dihub

[17] UTIAS Space Flight Laboratory, *On-Orbit Results from the CanX-7 Drag Sail Deorbit Mission*, 2017 Available: https://digitalcommons.usu.edu/cgi/viewcontent.cgi?article=3672&context=smallsat

[18] University of Toronto, *UTIAS Space Flight Laboratory*, 2014 Available: https://www.utias-sfl.net/

[19] Purdue University, *Upcoming space mission to test Purdue-developed drag sail pulling rocket back to Earth*, 2020 Available: https://www.purdue.edu/newsroom/releases/2020/Q3/upcoming-space-mission-to-test-purdue-developed-drag-sail-pulling-rocket-back-to-earth.html

[20] Keldysh Institute of Applied Mathematics, *Performance Scalability of Square Solar Sails*, 2017 Available: https://arc.aiaa.org/doi/abs/10.2514/1.A33894?journalCode=jsr&#:~:text=Square%2DSail%2DPerformance%20Scalability,-The%20most%20important&text=limits%20the%20admissible%20axial%20load%20applied%20to%20each%20boom.&text=Lateral%20boom%2Dtip%20deflection%20under,as%20the%20sail%20size%20increases.

[21] NASA MSFC, *Solar Sail Propulsion*, 2005 Available: https://www.nasa.gov/centers/marshall/pdf/134645main_solar_sail_fs.pdf

[22] NASA, *The Drag Equation*, 2015 Available: https://www.grc.nasa.gov/www/k-12/airplane/drageq.html

[23] University of Florida, *CubeSat Mission to Demonstrate Aerodynamically Controlled Re-Entry using the Drag De-Orbit Device (D3)*, 2018 Available: https://digitalcommons.usu.edu/cgi/viewcontent.cgi?article=4147&context=smallsat

[24] Georgia Institude of Technology, *Stability for a Deployable Drag Device for Small Satellite Deorbit*, 2016 Available: https://arc.aiaa.org/doi/10.2514/6.2016-5676

[25] The Space Foundation, *Space Briefing Book*, 2021 Available: https://www.spacefoundation.org/space_brief/types-of-orbits/

[26] Orbital Debris Program Office, *Frequently Asked Questions*, 2021 Available: https://www.orbitaldebris.jsc.nasa.gov/faq.html#12

[27] Florida International University, *The Vis Viva Equation*, Accessed 2021 Available: https://faculty.fiu.edu/~vanhamme/ast3213/orbits.pdf

[28] ULA, *Orbital Disposal of Launch Vehicle Upper Stages*, 2015 Available: http://fiso.spiritastro.net/telecon13-15/Reed_8-5-15/Reed_8-6-15.pdf

[29] NASA, *Earth's Magnetosphere*, 2013 Available: https://www.nasa.gov/mission_pages/sunearth/science/inner-mag-mos.html

[30] Wikipedia, *Van Allen Belts Image*, 2006 Available: https://en.wikipedia.org/wiki/File:Van_Allen_radiation_belt.svg

[31] David L. Edwards et al, *Electron Radiation Effects on Candidate Solar Sail Material*, 2004 Available: https://journals.sagepub.com/doi/abs/10.1177/0954008304044106

[32] Fugett, Daniel, *ATOMIC OXYGEN CONSIDERATIONS FOR LEO DE-ORBIT TRAJECTORIES USING SOLAR SAILS*, 2017 Available: https://digitalcommons.calpoly.edu/cgi/viewcontent.cgi?article=2973&context=theses

[33] University of Toronto Institute for Aerospace Studies, *Sail Material, Inspection Imager, and Deployment Analysis for an End-Of-Life Disposal Drag Sail*, 2018 Available: https://digitalcommons.usu.edu/cgi/viewcontent.cgi?article=3098&context=smallsat

[34] Antonenko, J., *Thermal control materials in Mercury environment, page 170-171*, 2003 Available: http://articles.adsabs.harvard.edu//full/2003ESASP.540..169A/0000171.000.html

[35] Joyce A Dever, Russell Messer, Charles Powers, Jacqueline Townsend and Eve Wooldridge, *Effects of vacuum ultraviolet radiation on thin polyimide films*, June 2001 Available: https://citeseerx.ist.psu.edu/viewdoc/download?doi=10.1.1.968.8002&rep=rep1&type=pdf

[36] Johnson, Nicholas, *Origin of the Inter-Agency Space Debris Coordination Committee* Available: https://ntrs.nasa.gov/api/citations/20150003818/downloads/20150003818.pdf

[37] Kelso, Dr. T.S., *Celestrak*, 2021 Available: http://celestrak.com/satcat/search.php

[38] J.-C. Liou, Nicholas L. Johnson, N. M. Hill, *Controlling the growth of future LEO debris populations with active debris removal*, 04/2010 Available: https://www.sciencedirect.com/science/article/abs/pii/S0094576509003981?casa_token=_My5etl-eikAAAAA:sCv0WwnCdluibMB9vpmHIYQVO2vuZzvhUdEYfuFQc0f-ofvH_NRQwbgN1NBEGXfozw1isRTyBg

[39] J.-C. Liou, Nicholas L. Johnson, *A sensitivity study of the effectiveness of active debris removal in LEO*, 02/2009 Available: https://www.sciencedirect.com/science/article/abs/pii/S0094576508002634?casa_token=Z9FQku6UfoMAAAAA:0YEaFwUOnaLGTsWiH5QAxP8RykiVJIv9eAMBx_H2d9X7hXz8foLOimeH6c4YT-C3G7POhboipg

[40] CubeSat.org, *The CubeSat Program* Available: https://www.cubesat.org/about

[41] Kulu, Erik, *Nanosats Database*, 2014 Available: https://www.nanosats.eu/

[42] SpaceX, *Falcon's User Guide*, 2020 Available: https://www.spacex.com/media/falcon_users_guide_042020.pdf

[43] ULA, *Delta IV Launch Services User's Guide*, 2013 Available: https://www.ulalaunch.com/docs/default-source/rockets/delta-iv-user's-guide.pdf

[44] Ariane Space, *ARIANE 5 USER'S MANUAL*, 2016 Available: https://www.arianespace.com/wp-content/uploads/2011/07/Ariane5_Users-Manual_October2016.pdf

[45] United Launch Alliance, *Vulcan Centaur Datasheet* , 2021 Available: https://www.ulalaunch.com/rockets/vulcan-centaur

[46] ULA, *CubeSat Express The Future of Rideshare Launch*, 2017 Available: https://www.ulalaunch.com/docs/default-source/rideshare/cubesat-express-the-future-of-rideshare-launch-(cubesat-developer's-workshop-may-2017).pdf

[47] US Air Force Space Test Program, *Evolved Expendable Launch Vehicle Secondary Payload Adapter*, 2001 Available: https://digitalcommons.usu.edu/cgi/viewcontent.cgi?article=2028&context=smallsat

[48] Juan Fernandez,Vaios Lappas, Andrew Daton-Lovett *Completely stripped solar sail concept using bi-stable reeled composite booms*, 2011 Available: https://www.sciencedirect.com/science/article/abs/pii/S0094576511000543

[49] The Planetary Society, *LightSail 2*, Accessed 4/2021 Available: https://www.planetary.org/sci-tech/lightsail

[50] NASA NTRS, *Development and Ground Testing of a Compactly Stowed Scalable Inflatably Deployed Solar Sail*, 2004 Available: https:

//www.researchgate.net/publication/23592289_Development_and_Ground_Testing_of_a_Compactly_Stowed_Scalable_Inflatably_Deployed_Solar_Sail

[51] NASA Astromaterials Research and Exploration Sciences, *NASA ORDEM 3.1 Model*, 03/2021 Available: https://orbitaldebris.jsc.nasa.gov/modeling/ordem-3.1.html

[52] Alan Zehnder, *Fracture Mechanics, p.55-84*, 2021 Available: https://link-springer-com.ezproxy.lib.calpoly.edu/content/pdf/10.1007%2F978-94-007-2595-9.pdf

[53] MIT, *Material Property Database*, Accessed 04/2021 Available: https://www.mit.edu/~6.777/matprops/polyimide.htm

[54] UBE Industries, *Upilex Polymide Film*, Accessed 5/2021 Available: https://www.ube.com/upilex/en/upilex_grade.html

[55] Piyush Mehta, Andrew Walker, Earl Lawrence, Richard Linares, David Higdon, Josef Koller, *Modeling satellite drag coefficients with response surfaces*, 10/2014 Available: https://www.sciencedirect.com/science/article/abs/pii/S027311771400413X#:~:text=A%20drag%20coefficient%20value%20of,commonly%20used%20in%20the%20past.&text=In%20addition%2C%20fitted%20drag%20coefficients,used%20in%20the%20drag%20model.

[56] Rocket & Space Technology, *ATMOSPHERE PROPERTIES*, Accessed 05/2021 Available: http://www.braeunig.us/space/atmos.htm

[57] Space Environment Technologies, *COSPAR International Reference Atmosphere, 2012*, 07/2012 Available: https://spacewx.com/wp-content/uploads/2021/03/chapters_1_3.pdf

[58] NASA Goddard Earth Sciences, *Solar Radiation*, Accessed 05/2021 Available: https://earth.gsfc.nasa.gov/climate/research/solar-radiation

[59] Google.com, *Area of Trapezoid Forumla*, Accessed 05/2021 Available: https://www.google.com/search?q=are+of+trapezoid&rlz=1C5CHFA_enUS926US926&oq=are+of+trapezoid&aqs=chrome..69i57j0i10i131i433j0j0i10l2j0j0i10l4.2431j0j7&sourceid=chrome&ie=UTF-8

[60] Stanford University Department of Materials Science and Engineering, *Mechanical Properties of Thin Films*, 01/2005 Available: https://imechanica.org/files/353%20Class%20Notes%202005.pdf

[61] ScienceDirect, *Innovative Bridge Design handbook*, 2016 Available: https://www.sciencedirect.com/topics/engineering/suspension-bridges

[62] Vedantu.com, *Centroid of a Trapezoid Formulation*, Accessed 05/2021 Available: https://www.vedantu.com/formula/centroid-of-a-trapezoid-formula

[63] Christoph Sickinger, Lars Herbeck, *DEPLOYMENT STRATEGIES, ANALYSES AND TESTS FOR THE CFRP BOOMS OF A SOLAR SAIL*, 03/2003 Available: https://www.dlr.de/fa/en/Portaldata/17/Resources/dokumente/institut/2002/2002_03.pdf

[64] The CubeSat Program, Cal Poly, *Poly Picosatellite Orbital Deployer Mk. III Rev. E User Guide*, 03/2014 Available: https://static1.squarespace.com/static/5418c831e4b0fa4ecac1bacd/t/5806854d6b8f5b8eb57b83bd/1476822350599/P-POD_MkIIIRevE_UserGuide_CP-PPODUG-1.0-1_Rev1.pdf

[65] ISISpace, *ISIPOD CubeSat Deployer*, Accessed 05/2021 Available: https://www.isispace.nl/product/isipod-cubesat-deployer/

[66] Ohad Ben-Yaacov, Eviatar Edlerman, Pini Gurfil, *Analytical technique for satellite projected cross-sectional area calculation*, 07/2015 Available: https://www.sciencedirect.com/science/article/abs/pii/S027311771500263X

[67] Michigan Tech University, *The Solar Constant*, Accessed 05/2021 Available: http://www.geo.mtu.edu/KeweenawGeoheritage/MiTEP_ESI-2/Solar_Constant.html

[68] NASA, *Launching From Florida: Life in the Fast Lane!*, Accessed 05/2021 Available: https://www.nasa.gov/pdf/142825main_Bobsled_Launch.pdf

[69] Markley, F. Landis, Crassidis, John L., *Fundamentals of Spacecraft Attitude Determination and Control, p. 389*, 2014

[70] M. Moe, S. Wallace, K. Moe, *Recommended Drag Coefficients for Aeronomic Satellites*, 2013 Available: https://www.semanticscholar.org/paper/Recommended-Drag-Coefficients-for-Aeronomic-Moe-Wallace/c4e4e6b250b6a733a717e157897fbb23e84bd1f3

[71] David Gondelach, Roberto Armellin, Aleksander Lidtke, *Ballistic Coefficient Estimation for Reentry Prediction of Rocket Bodies in Eccentric Orbits Based on TLE Data*, 07/2017 Available: https://www.hindawi.com/journals/mpe/2017/7309637/

[72] Robert A. Hawkins, Joseph A. Palomares, *De-Orbiting Upper Stage Rocket Bodies Using a Deployable High Altitude Drag Sail*, 06/2012 Available: https://digitalcommons.calpoly.edu/cgi/viewcontent.cgi?article=1103&context=aerosp

[73] NASA, *Orbital Debris Quarterly News, Volume 23, Issue 1 & 2*, Accessed 05/2021 Available: https://orbitaldebris.jsc.nasa.gov/quarterly-news/pdfs/odqnv23i1.pdf

[74] MathWorks, *PlanetEphemeris Function*, Accessed 05/2021 Available: https://www.mathworks.com/help/aerotbx/ug/planetephemeris.html

[75] MathWorks, *ode45() Function*, Accessed 05/2021 Available: https://www.mathworks.com/help/matlab/ref/ode45.html

[76] James Woodburn, Sergei Tanygin, *EFFICIENT NUMERICAL INTEGRATION OF COUPLED ORBIT AND ATTITUDE TRAJECTORIES USING AN ENCKE TYPE CORRECTION ALGORITHM*, 01/2002 Available: https://www.researchgate.net/publication/265230374_AAS_01-428_EFFICIENT_NUMERICAL_INTEGRATION_OF_COUPLED_ORBIT_AND_ATTITUDE_TRAJECTORIES_USING_AN_ENCKE_TYPE_CORRECTION_ALGORITHM

[77] University of Virginia, *Perturbation Formulations for Satellite Attitude Dynamics*, 11/1974 Available: http://articles.adsabs.harvard.edu/cgi-bin/nph-iarticle_query?1976CeMec..13...39K&defaultprint=YES&filetype=.pdf

[78] GregorDS, *Encke's Method Visualized*, Accessed 05/2021 Available: https://upload.wikimedia.org/wikipedia/commons/thumb/d/dc/Enckes_method-vector.svg/220px-Enckes_method-vector.svg.png

[79] Deutsches Zentrum für Luftund Raumfahrt German Aerospace Center, *The ROSAT Mission*, Accessed 05/2021 Available: https://www.dlr.de/content/en/articles/missions-projects/past-missions/rosat/rosat-mission.html

[80] Wikipedia, *Tianggong Image*, Accessed 05/2021 Available: https://en.wikipedia.org/wiki/Tiangong-1

[81] NASA Ames, *GeneSat-1*, Accessed 05/2021 Available: https://www.nasa.gov/centers/ames/missions/2007/genesat1.html

[82] eoPortal, *GeneSat-1 Mission Database*, Accessed 05/2021 Available: https://directory.eoportal.org/web/eoportal/satellite-missions/g/genesat

[83] Space-track.org, *Archived TLE Data*, Accessed 05/2021 Available: https://www.space-track.org/#/gp

[84] CNES, ARIANEGROUP,ARIANESPACE,ESA , *Maneuvers to Reduce Ariane 5 Upper Stage Lifetime Duration in Orbit*, 2019 Available: https://www.hou.usra.edu/meetings/orbitaldebris2019/orbital2019paper/pdf/6090.pdf

[85] Spacelaunchreport.com, *Space Launch report: Delta IV Data Sheet*, Accessed 05/2021 Available: https://www.spacelaunchreport.com/delta4.html

[86] SpaceNews.com, *ULA to launch Delta 4 Heavy for its 12th mission, four more to go before rocket is retired*, Accessed 05/2021 Available: https://spacenews.com/ula-to-launch-delta-4-heavy-for-its-12th-mission-four-more-to-go-before-rocket-is-retired/

[87] NASA Goddarn SFC, *World of Change: Solar Activity*, Accessed 06/2021 Available: https://earthobservatory.nasa.gov/world-of-change/Solar

[88] MOOG, *ESPA User Guide*, 11/2018 Available: https://elibrary.gsfc.nasa.gov/_assets/doclibBidder/tech_docs/Moog_ESPA_UsersGuide%20-%20Copy.pdf

[89] ai-solutions, *LVLH - Earth Pointing*, Accessed 06/2021 Available: https://ai-solutions.com/_freeflyeruniversityguide/attitude_reference_frames.htm

[90] J.-C. Liou, *An active debris removal parametric study for LEO environment remediation*, 06/2011 Available: https://www.sciencedirect.com/science/article/abs/pii/S0273117711000974?

casa_token=F8XF17utNH4AAAAA:C2kmdWZ_W-dxL_ZfJA8_

jVqkbuYi5SPlmm0r4yDZ8oD71wK17acamHN7muD7XQLC_IrDLPe1GQ